Manufacture and Testing of an Active Compressor Blade for Aeroelastic Studies

by

Debashis Sahoo

B.Tech.(Hons.) in Aerospace Engineering, Indian Institute of Technology, Kharagpur, India (1998)

Submitted to the Department of Aeronautics and Astronautics
in partial fulfillment of the requirements for the degree of

MASTER OF SCIENCE

at the

MASSACHUSETTS INSTITUTE OF TECHNOLOGY

June 2000

Author_____
Department of Aeronautics and Astronautics
May 26, 2000

Certified by_____
Professor Carlos E. S. Cesnik
Assistant Professor of Aeronautics and Astronautics
Thesis Supervisor

Accepted by_____
Professor Nesbitt W. Hagood, IV
Chairman, Department Graduate Committee

Manufacture and Testing of an Active Compressor Blade for Aeroelastic Studies

by

Debashis Sahoo

Submitted to the Department of Aeronautics and Astronautics
on May 26, 2000, in partial fulfillment of the
requirements for the degree of
Master of Science

Abstract

This thesis deals with the manufacture of a 26-bladed 'active' rotor that will be used for developing an experimental database on turbomachinery aeroservoelastic phenomena, such as flutter and its control. The active rotor has blades made of two stress-bearing composite spars, aerodynamically shaped foam, piezoelectric actuators attached to the spar base and a root which allows the blade to be inserted into the rotor.

The thesis analyzed the models developed for the active rotor blade design from previous studies and made suitable refinements in them. The following parameters were obtained – spar dimensions, their location and material, piezoelectric dimensions and material, foam material, and root structure and material.

Next, technologies were developed for manufacturing the root and the twisted spar, packaging the piezoelectric actuators using copper-Kapton and bonding them to the spars, and wiring the spars and actuators. However, further investigation is necessary with regards to the issues of foam shaping, spar-foam attachment, and development of accurate leading and trailing edges of the blade.

The final step involved testing the blade before and after spar-foam bonding. This required testing on the benchtop to obtain the blade performance limitations, and then testing it in vacuum while spinning inside a spin pit, which was constructed for this purpose. The latter gives the blade performance under rotation. The scope of the thesis is limited to the benchtop tests conducted on the active wired spars. Some of the blade and spin pit wiring issues need to be resolved before conducting the spin tests in vacuum. Also a rotor frame incorporating 26 active blades needs to developed to test under vacuum and in a wind tunnel.

The results of the preliminary benchtop tests as well as the blade finite element model predict that the blade performance would be lower than the initial target. Several ways of improving its actuation capability considered were: (a) applying higher voltage with DC offset to the actuators, (b) using multi-wafer actuators, and (c) using active fiber composites. However, these issues need further work. The active rotor, when completed, will serve as a robust tool for aeroservoelastic testing over a significantly larger operating range than is currently possible.

Thesis Supervisor: Professor Carlos E. S. Cesnik
Title: Assistant Professor of Aeronautics and Astronautics

Acknowledgments

I would like to express my gratitude to my advisor, Professor Carlos Cesnik, for introducing the problem to me and for giving me unstinting guidance, advice and support throughout the execution of the project and especially during the difficult times. Many thanks to Professors Paul Lagace, Mark Spearing and John Dugundji of TELAC, and Jim Paduano of GTL whose inputs during the critical stages of the project were invaluable.

A special mention must be made of the undergraduate research assistants who worked with me on this project. Scott Liebermann, who was responsible for the manufacture of the root of the blade. Garrett Barter, who has helped me in almost all aspects of the blade manufacture. Special thanks to Yassir Azziz and Garrett for figuring out the complicated task of manufacturing the twisted composite blade. And finally, Jadon Smith who is helping us in the difficult task of machining of the blade.

I would also like to thank the lab technicians – John Kane of TELAC, Dave Robertson and Paul Bauer of AMSL/SSL, and James Letendre and Viktor Dubrowski of GTL who provided us with timely help and allowed us to use the lab facilities.

I am grateful to the following graduate students who provided valuable inputs during various stages of the project - Michael Fripp, Chris Dunn and SangJoon Shin of AMSL, Seth Kessler and Torry Radcliffe of TELAC, and Dean Head and Waleed Farahat of GTL. A special mention must be made of Dr. Zhongwei Li and Dr. Gerald Guenette of GTL who guided us through some of the difficult phases of the project.

I must thank all the members of GTL, TELAC, and AMSL who eased my transition from Indian to American way of life.

The unflinching support and encouragement of my family also helped me a great deal in this transition and for making a productive use of my stay at MIT.

The funding for this research was provided under the Air Force Office of Scientific Research (AFOSR) Grant Number F49620-95-1-0280, and Grant Number F49620-95-1-0409: their support is gratefully acknowledged.

Contents

List of Figures

List of Tables

Nomenclature

Roman

B_{ij}	Strain-displacement transformation matrix components
d_i	Nodal displacement vector components
d_{ij}	Piezoelectric strain constant
D_{ij}	Elastic matrix components
E, E_{ij}	Tensile modulus
G, G_{ij}	Shear modulus
K_{ij}	Stiffness matrix components
M_{ij}	Mass matrix components
N_{ij}	Shape function
p_i	External force at any point on blade
P_i	Nodal force matrix components
S	Shear strength
t	Time
T	Kinetic energy
u_i	Blade displacement vector components
U	Potential energy
v	Volume
V	Electrical voltage across piezoelectric actuator in the 1-3 direction
X_t	Longitudinal tensile strength
Y_t	Transverse tensile strength

Greek

ϵ_i	Strain tensor components
ν_{ij}	Poisson's ratio
ρ	Density
σ_i	Stress tensor components
Λ	'Equivalent' thermal strain due to piezoelectric effect

Subscripts

a	Actuation effect
c	Centrifugal effect
e	Elemental
piezo	Piezoelectric material
1, 2, 3	Material direction

Superscripts

$\bullet$	Differentiation with respect to time
^{T}	Transverse matrix operator

Chapter 1

Introduction

1.1 Motivation

Man's desire to fly like birds led to the invention of the aeroplane. Since the Wright brothers' first powered flight in the early part of the 20th century, the aeronautics industry has come a long way. Great strides have been made in propulsion system development, particularly the gas turbine engine. However, the quest for improved efficiency, higher thrust-to-weight ratio, higher stage loading and higher pressure has pushed the engine performance and integrity to the limits [1]. One of the most challenging problems being faced is the vibration of engine parts, which includes (a) resonant vibration occurring at an integral order, i.e., multiple of rotation speed, and (b) flutter, an aeroelastic instability occurring generally as a non-integral order vibration, having the potential to escalate into larger and larger stresses resulting in serious damage to the engine. The associated failures of engine blades are referred to as high cycle fatigue (HCF) failure.

HCF has been explicitly identified as the dominant engine failure mode from 1989 to 1994 in both civilian and military aircraft engines ([2] and [3]). HCF failure has been identified to have occurred during final engine test phase, after an engine has successfully passed qualification tests and production has begun, and even worse during flight! Moreover, HCF problems are usually identified only after failure has occurred even though the root causes of failure may have been present for a considerable time. Recent meetings of industry, government and academic experts in turbomachinery have found out that "high cycle fatigue failure prevention will not be accomplished through improving the material resistance to vibratory stresses ... or through further improvements in nondestructive evaluations. Rather

it must be accomplished through better management of the applied vibratory stresses, either by reducing the forcing excitation or structural response or both ... This implies obtaining a much improved ability to predict the conditions under high vibratory stresses will occur as well as their locations, amplitudes, frequencies and directions." [2]

The ability to accurately and reliably predict HCF failure is a challenging task. Although finite element structural analysis and testing techniques have matured over the years, the story is different in the unsteady aerodynamic case. Aerodynamic forcing functions are not well predicted or known for complex cases of interest, such as wake behavior at off-designed conditions, effects of adjacent blade rows or adjacent stages, transonic flows over the rotor blades, large amplitude dynamic separation and so on. As pointed out in [4], wind tunnel unsteady aerodynamic tests on full scaled or aeroelastically scaled 'rigid' models have been used till date to improve the accuracy of analytical predictions, based on either empirical methods or computational fluid dynamics (CFD) or a combination of two. However, these models cannot be used for testing over the whole flight envelope and over all interesting frequencies because of structural limitations. This lack of a complete experimental database has limited flutter investigation even in the 90s [1]. A major hurdle in the attempt to get such a database "can be removed if testing methods are developed to measure all participating generalized aerodynamic loads on configurations which will be made to oscillate at the frequencies, flight conditions and deformation (motion) shape of the aeroelastic ... configurations investigated." [4]

1.2 Active Rotor Concept

In 1996, the gas turbine community of Massachusetts Institute of Technology (MIT) proposed to address the problem of lack of experimental data through development of an 'active rotor'. Such a rotor has individual blades with embedded piezoelectric actuators which can operate at bandwidths up to several times blade resonant mechanical frequencies of interest. Because every blade is actively controlled, the unsteady blade environment is unambiguously defined. The actuators can be used to excite several modes at any desired interblade phase angle to simulate a variety of flow conditions. Once these features are realized, the active rotor can serve the following purposes:

(a) It can provide a method to measure aerodynamic damping coefficients across the

entire operating range of the rotor. This can be done by driving the rotor at appropriate interblade phase angle at an operating point and measuring the resulting blade motion. Knowledge of damping can then be used to locate the turbomachinery flutter boundary.

(b) Blade tuning (the coincidence of modal frequencies of the individual blades in the rotor) is an important parameter for aeroelastic instability. This can be simulated by actively controlling the stiffness and damping of individual blades of the active rotor.

(c) Data on aerodynamic loads and the interactions between the loads and the blades have been difficult to separate, but the active rotor can add new and different information. It can be used as a three-dimensional system identification tool that allows interrogation of the flow structure at a greatly increased signal-to-noise ratio, and thus with more resolution than is now possible.

(d) Finally the active rotor concept can be used for building low order system models, which coupled with advanced system identification techniques, can then be used for developing effective technology for detecting HCF phenomena *in situ* in an operating engine prior to failure.

Active Blade Components and Actuation Modes

In order to achieve the above objectives, the active rotor blade was subdivided into the following components:

- Two fiber composite beams, known as spars, covered with high bandwidth piezoelectric actuators near the root on both sides,
- A relatively low stiffness aerodynamic shell made of foam, and
- A root structure to allow the blade to fit into the rotor hub.

The spars support the blade under the large centrifugal stresses and the foam gives an aerodynamic shape to the blade. The actuators are attached at the root to maximize their effectiveness in deforming the blade. This active blade structure conveniently enables useful modes of actuation. The spars can be deformed by bending through out-of-phase actuation of the piezoelectric wafers on both sides of the spar. The blade shape and movement can be controlled by actuating the spars in bending in the same direction or in opposite directions. The blade will bend in the former case and twist in the latter. By using a combination of

bending and twisting modes of actuation, the desired deformation mode can be imparted to the blade during aeroelastic experimentation. More about this is illustrated in [7].

The active rotor needs to meet the following requirements, in order to be useful as an experimental aeroelastic tool:

- The available controlled twist at the tip of the blade must be at least 0.25° (1° is the ideal twist authority desired).
- The available bending at the tip should be near 0.3° (or 1 mm tip bending for the 177 mm long blade).

These requirements have been obtained from aerodynamic considerations and are discussed in more detail in [7].

Active Rotor Configuration

The configuration chosen for the active rotor design is a 31.3% geometric scale model of the Quiet Engine Program (QEP) Fan C Build 3 design [5]. It is a 26 titanium bladed rotor and since the blades are scaled, the maximum design speed is increased from 5200 rpm to 16000 rpm. Due to this speed, the tip of the blade will go over transonic flow regime. The other noteworthy features of the blade are its vibratory modes, particularly the first bending mode at 330 Hz and first torsion mode at 900 Hz. These figures are useful in designing the active blade. Figure 1-1 shows a representation of the scaled Fan C blade. The reason for choosing this rotor configuration is that it has interesting flutter problems and has undergone extensive mechanical and aerodynamic testing. Additional information about the rotor and its tests can be found in [6].

1.3 Previous work done on active rotor concept

The preliminary design and development of the active rotor is outlined in [7]. The identification of the spar material, its thickness and thickness distribution, and orientation of the composite fibers were found by focusing on straight untwisted untapered spars. Construction and experiments such as tensile pull tests on the simplified spar specimens gave an initial idea of the limiting parameters of the spar.

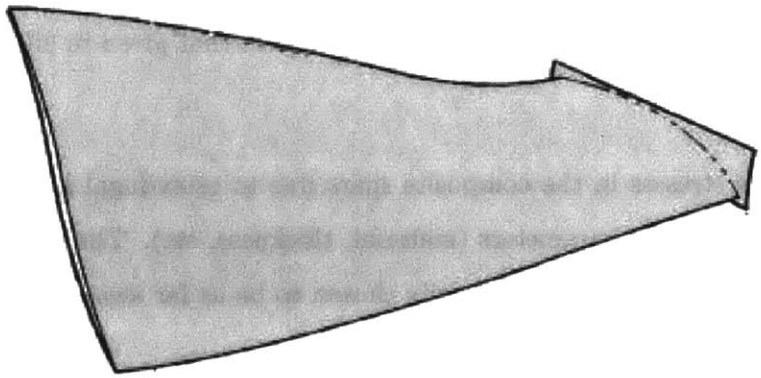

Figure 1-1: GE scale Fan C Titanium blade.

The material and thickness properties of the piezoelectric actuators, and their location within the blade were also addressed. Significant work was done on packing of the piezoelectrics with copper-Kapton to maintain electrical connection as well as to improve the failure strain of the package. Two options were investigated to protect the actuators from high strains due to the centrifugal loads, as predicted by a finite element model (FEM) of the blade. The first option of embedding the piezoelectric within the composite plies was discarded because it was predicted by Classical Laminated Plate Theory (CLPT) to be not strong enough. The second method of protection considered was surface bonding of the piezoelectric wafer to the composite spar while under compression. A shear lag analysis was done to predict the failure strain of the bond layer under centrifugal loads and thus to identify the bonding agent between the spar and the piezoelectric actuator.

Experiments were done on piezoelectric actuators attached to the simplified spars mentioned above. These include actuation under loading tests, in which the spar was extended by different load levels while the piezoelectric material was actuated; this gave an indication of the piezoelectric actuation level under centrifugal stresses. Creep tests were also performed on the precompressed piezoelectric actuator to find the effectiveness of the precompression over time.

Preliminary investigations were made to identify the foam material as well as the methods to give the desired aerodynamic shape to the foam. However, those issues were not fully addressed in [7].

As mentioned before, a detailed finite element model was constructed from the coordinates of the GE scaled Fan C blade. Validation was done by changing the blade material to titanium and comparing the natural frequencies with that given in [6]. The goals of the model was threefold:

- Predict the stresses in the composite spars due to centrifugal loads and thus aid in identifying the spar parameters (material, thickness, etc). The distance between the spars inside the blade was arbitrarily chosen to be as far away as possible from each other;

- Predict the strain levels on the piezoelectric actuators: this was used in identifying the amount of precompression of the actuator; and

- Predict the blade tip deflection (both bending and twist) available from piezoelectric actuation over a broad range of frequencies of applied signal; this served to characterize the performance and usefulness of the actuator.

Benchtop actuation tests were performed with the simplified spars attached with piezoelectric wafers near the cantilevered end. Also finite element analysis was done on the specimen and the spar tip deflection results were compared with the benchtop experiment for a wide range of frequencies. This gave useful information for better modeling of the piezoelectric effect in the FEM using experimental hysteresis curves of the piezoelectric material. It also gave useful information for modeling the composite fiber properties so as to accurately capture the dynamics of the specimen.

In all the above analyses, it was assumed that aerodynamic loads were not significant compared to centrifugal ones and hence not considered.

1.4 Scope of Thesis

This thesis continues the development of the active rotor blade, focusing on refinements in the design process, manufacturing issues related to the spars, connection of the piezoelectric actuators to the spar, aerodynamic foam shaping, assembling of the various blade components, and testing of the twisted tapered spar in vacuum under centrifugal loads before attaching it to the foam. The testing of the final blade is left for future work.

Chapter 2 details the models used in the design and development of the active rotor blade. A short description of the models used in [7] along with the useful parameters obtained from them are enlisted. The limitations of the models and refinements made in them are also discussed in detail. Also the topics not dealt with in the previous models, such as root design, spar location and aerodynamic load effect, are analyzed.

Chapter 3 describes the manufacturing procedure of the spar and root. It includes details of the construction method of root-filler and graphite-epoxy plate, cutting of spars from the plate, and also a tensile pull test done to verify the integrity of the manufacturing process as well as the root-blade system under rotation.

Chapter 4 describes the issues related to the actuator and sensor preparation, and the blade wiring characteristics. The problems associated with them, the characteristic tests of the actuator and the bonding of spar and actuator are dealt with. Finally, recommendations are made for improvement in the active wired spar construction method.

Chapter 5 details the methods of shaping the foam to get the desired twisted aerodynamic shape. The pros and cons of various methods of foam shaping are outlined too.

Chapter 6 deals with the process of assembling the blade from its parts. Detailed analysis is done on the method of blade construction through the example of the first twisted blade that was made, including the spin test done on the blade. The effect of subjecting the blade to several thermocycles is also found and based on these observations, suggestions are made for improvement in the assembly process.

Chapter 7 discusses the test plan undertaken to characterize the active wired spar behavior before attaching the spar and foam using the new recommendations. The instrumentation used for the various tests, procedure of the tests, and results are discussed.

Chapter 8 summarizes the work done, conclusions made therein and gives an outline for the future work to be done on building the 26-bladed active rotor system and testing it for aeroelastic studies.

Chapter 2

Design and Modeling Issues

The active rotor blade has four principal components – spars, piezoelectric actuators, foam and root. There is also a transition region between the root and the blade, known henceforth as transition element. [7] describes the design and modeling issues related to the spar, foam and actuator. This chapter outlines the main features of the models and describes the subsequent refinements made in them. It also deals with the design of the root and transition element.

2.1 Simplified Blade Model

2.1.1 Model Description

For preliminary analysis purpose, [7] simplified the blade to a straight untwisted untapered shape with a skew angle to the rotational axis. The skew angle was specifically chosen to increase the stress level to approximately that of the actual blade. The spacing between the spars and their width was kept uniform and the width was chosen to eliminate the need for cambered spars. The piezoelectric length was taken as approximately 50% of the length of the spar. The complex foam shape was replaced by a volumetric equivalent rectangle. The foam and the actuators were modeled as isotropic materials and the composite properties of the spar were smeared and taken to be isotropic. The blade root was not considered.

The blade was given a rotation of 16000 rpm (obtained from [6]) and the stresses on the blade were calculated. Failure of the blade was determined by the Maximum-Distortion-Energy Criterion, which combines the multi-dimensional loads (axial and shear) to give the

von Misses stress, that can be directly compared to the failure stress of the material. More information on material failure models can be obtained from [11].

2.1.2 Useful Blade Parameters Derived from the Model

Several variables were varied in the model and their effects studied in [7]. These include material of the spar, its thickness taper, root thickness and skew angles in the width and thickness directions. The useful active rotor blade parameters obtained from this process have been enumerated below.

Spar material: Graphite-epoxy AS4/3501-6 from Hercules Composite Products Group was chosen for the manufacture of the spar.

Spar dimension: The spar thickness at the root was designed to be as thick as possible while accommodating the actuators and foam. A linear taper was adopted. From the blade dimensions obtained from [6], the root cross section has dimensions of 9 mm x 3 mm, the tip is of 9 mm x 0.5 mm dimensions, and the length of the spar is 177 mm.

Spar orientation: The spars were designed to emerge radially out of the rotor hub.

Other blade parameters were qualitatively chosen and are outlined below.

Spar location: The distance between the spars was arbitrarily chosen to be 30 mm.

Actuator material: PZT-5A from Morgan Matroc was chosen as the actuator because of its high actuation energy density.

Actuator dimension: The piezoelectric actuator dimensions were chosen to be 9 mm x 0.254 mm and a length of 36.3 mm (about 20% of the length of the spar). This is the most appropriate commercially available size of a single piezoelectric wafer. A single wafer actuator was chosen instead a series of wafers to simplify the manufacturing procedure.

Actuator location: The actuator location was chosen to be at the base of the spars to achieve maximum tip actuation.

Foam material: Rohacell WF 200 from Richmond Aircraft Products was chosen as the foam because of its low density and stiffness, high strength, and its potential ability to be thermoformed into complex shapes.

Foam dimension: The foam has a chord length of 65mm at root and 89mm at tip, and thickness of 7.4 mm at root and 2.4 mm at tip. The stagger angle is 6.5° at root and 71° at tip. The camber is 71° at root and $-1.7°$ at tip. These figures were obtained from [6].

2.2 Blade Finite Element Model

Using the above information, a finite element model of the blade was constructed in [7] in the commercial FEM package PATRAN/NASTRAN. More information on the package can be found in [16] and a brief theoretical background of the model is given in Appendix A.

The purpose of the model was to find out whether the blade in this configuration can survive the rotating environment of 16000 rpm and whether the desired level of actuation can be achieved. No aerodynamics was considered and an arbitrary root shape was assigned at this stage.

The following characteristics of the concept were determined:

- The operating load on the spar at 16000 rpm was found to be 570 MPa.
- The strain on a piezoelectric actuator was found to exceed the failure level by 1000 $\mu\epsilon$.
- The actuation level satisfied the 0.25° tip twist requirement over 1KHz frequency band.

Two issues were still not resolved from that model – fiber orientation in the spar and protection of piezoelectric actuators. The latter was solved in [7] by precompressing the actuator while bonding it to the spar. Precompression can be achieved in two ways. The first option is that of embedding the actuator within the composite plies. This results in residual thermal strains after completion of curing because of the mismatch between the coefficient of thermal expansion (CTE) between the spar and actuator. The amount of prestrain was predicted in [7] by a classical laminated plate theory (CLPT) based analysis for various fiber orientations of the spar. The minimum fiber orientation which gives $1000\mu\epsilon$ prestrain was found to be 56°.

The next step was to vary the fiber orientation and evaluate the spar laminate strength using Tsai-Hill failure criterion, which compares multiaxial stresses to the appropriate failure strengths and combines the result into a single number. This was used to determine failure by comparing with the operating load of 570 MPa. The maximum fiber angle which survives at 16000 rpm was found to be 31°, lower than the prestrain requirement.

Since the embedding option did not satisfy both strength and prestrain requirements, the actuator was surface-bonded to the spar and precompression done electrically while the

cure took place. Using shear lag analysis in [7], it was found that Epotec 301 (from Epoxy Technologies) would be able to keep the two together at 16000 rpm. Epotec is available in two parts A and B, which are mixed 4 parts by 1 before applying to the bonding surfaces and which become thermoset after the cure. Epotec 301 was found to hold the prestrain by experiments given in the reference.

The final issue resolved in the reference was the fiber angle which was required to be less than than 31°, as discussed above. Since the blade actuation due to piezoelectric action involves spar bending, it was desired to keep spar stiffness minimum in the direction of bending. However, the fiber angle was chosen to be 20° to maintain a factor of safety for strength reasons.

Having resolved these problems, the next step is to look at the aforementioned design method with a critical eye and make refinements if necessary.

2.3 Limitations of the Design Method

Three parameters of the blade were not analyzed while carrying out the design using the models developed in [7]. First was the design of the root and the transition element; second was the location of the spars within the blade and the last one was the bonding between the spars and foam. These issues are discussed in detail below.

2.3.1 Root Design

Designing of the root and the transition element require finding the appropriate material and basic structure, and predicting whether the root will survive at 16000 rpm centrifugal loads.

Material Choice and Basic Structure of Root

As illustrated by Figure 2-1, the blade is inserted into the hub of the rotor and held in place by clips. Therefore, two forces act on the root: (a) centrifugal loads at 16000 rpm, and (b) reaction force of the clips. The root needs to be strong enough to resist the two forces, and a wedge shape is optimum for resisting this type of load. As shown in the figure, the basic structure of the root consists of graphite-epoxy fibers coming out of the spars and a filler to create the correct shape of the root. The initial choice of filler material was steel

and the straight spars were made using steel filler. But considerations of weight reduction of blade and consequent hub stress reduction caused the change of filler material choice to graphite-epoxy. The filler layup was made quasi-isotropic to eliminate any undesirable directional property and is discussed in detail in Section 3.2.

Material Choice and Basic Structure of Transition Element

The transition element consists of graphite-epoxy fibers coming out of the spars and entering the root structure. The main function of the transition element is to provide a smooth transition region from the twisted shape of the spars to the relatively straight root. Hence the element was designed to come out straight from the root and merge with the spars smoothly. This design keeps the stress in the root to a minimum. It may be noted that the design was obtained purely by qualitative analysis rather than quantitative optimization analysis.

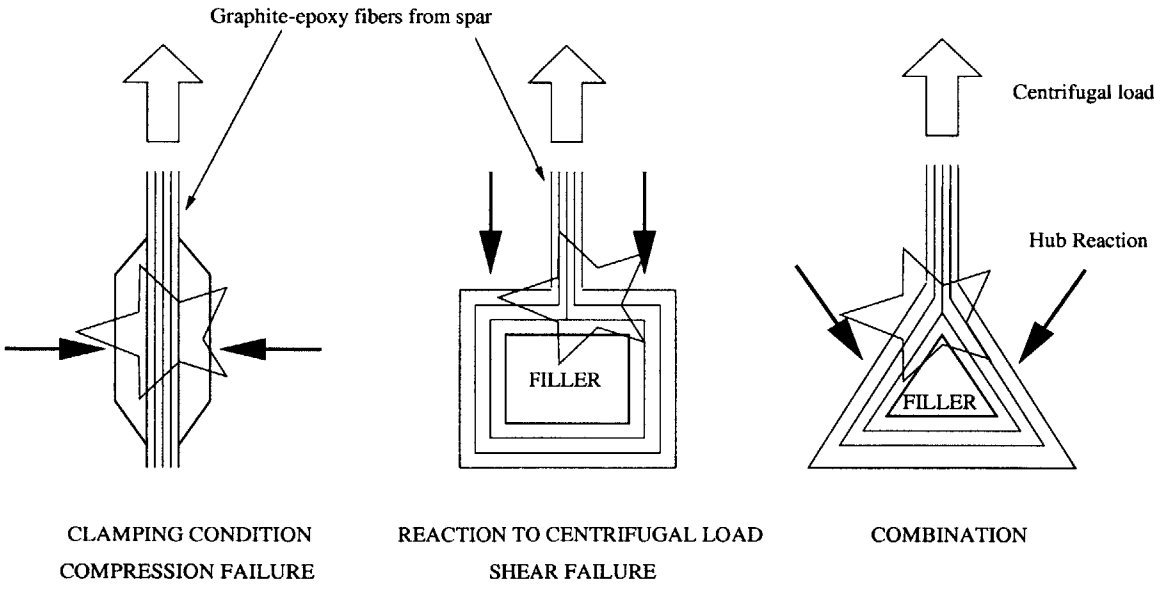

Figure 2-1: Illustration of different root structure concepts.

Finite Element Model of Root

(1) Geometry and Finite Elements:

A finite element model of the root was constructed in PATRAN/NASTRAN to determine its integrity in the presence of centrifugal load. The results were verified by a tensile

pull test (described in Section 3.4). The dimensions of the root were taken from the titanium Fan C blade and are shown in Figure C-1. Since failure of the root fibers and filler were being investigated, the modeling of the root was made more detailed than that done in the complete blade model. The plies coming out of the spars were modeled as solid brick-shaped elements, while the filler was modeled as solid wedge-shaped elements.

(2) Material:

The ply material values were transformed from the fiber direction to the appropriate angle of orientation ($\pm 20°$, in this case), were then converted into 3-D anisotropic properties, and finally applied to the solid ply elements. The reason is that PATRAN does not accept composite properties for solid elements. The filler was assigned the properties of steel. Codes were written for conveniently constructing the model in PATRAN and are given in Appendix C. Also the material values are given in Appendix B.

(3) Loading and Boundary Condition:

Centrifugal load at 16000 rpm was calculated near the root interface with the blade by assuming the blade to be an untwisted flat equivalent rectangular block. A code was written to find the force at the root by the procedure explained in [7]. The code and the symbols used in the code are explained in Appendix C. The force obtained was distributed over the front flat surface of the root so that the tensile force applied at each node of the front face in the FEM is 25 N.

The boundary condition was kept the same as that faced in the pull-up test, as illustrated in Figure 3-8. So half the inclined surface on each side of the root was fixed (clamped). Although this boundary condition is not exactly the one which the active blade faces in the rotor, the difference is assumed acceptable for this study. Secondly, it will help in comparing the FEM results with that of the pull tests.

(4) Analysis and Results:

Static linear analysis (SOL 101) was used to find the element stresses on the filler and ply stresses on the fibers due to the centrifugal load. Since the root has composite plies, Tsai Hill failure criterion was used to find whether the root can survive the centrifugal loads. The stress results for the root plies are shown in Figures 2-2(a) and (b).

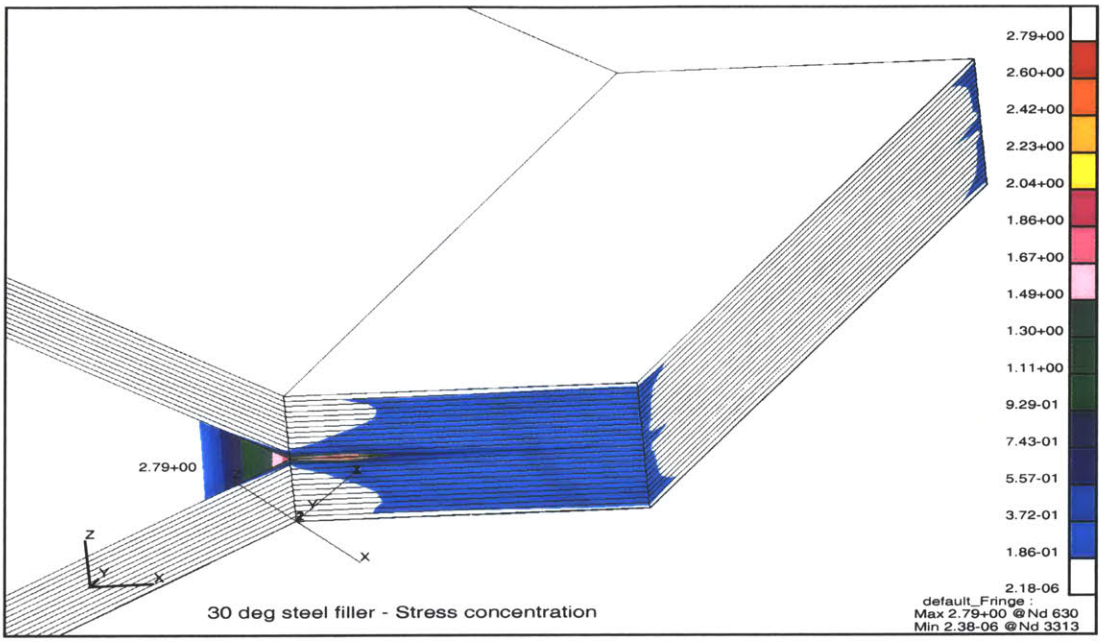

(a) Tsai-Hill stress concentration factor in plies for 30° half-angle

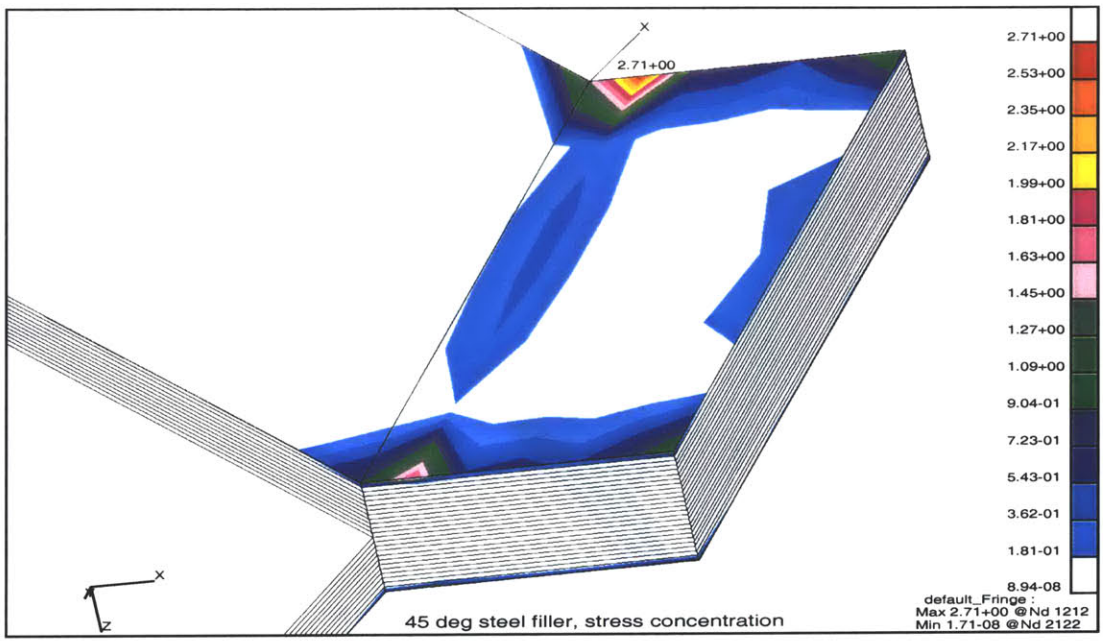

(b) Tsai-Hill stress concentration in plies for 45° half-angle

Figure 2-2: Stress analysis results of root at 16000 rpm centrifugal load – I. Numbers on the root show the maximum stress location.

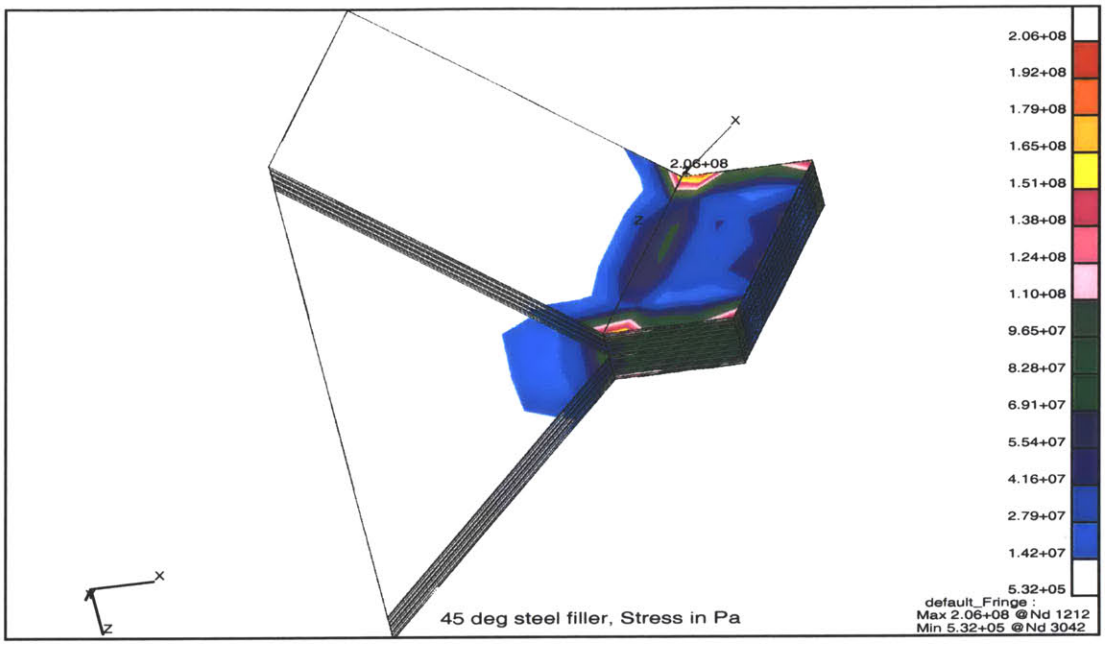

(a) von Mises stress (Pa) in blade plies for steel filler

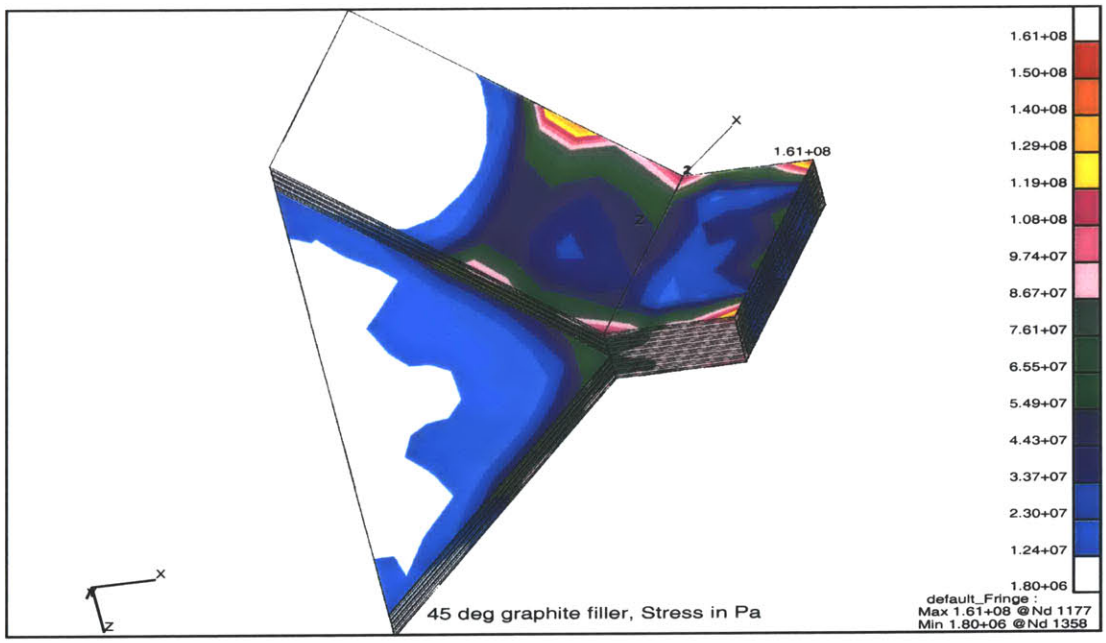

(b) von Mises stress (Pa) in blade plies for graphite filler

Figure 2-3: Stress analysis results of root at 16000 rpm centrifugal load – II. Numbers on the root show the maximum stress location.

The results are shown for various fiber angles and expressed in terms of multiples of failure stress of the material. The regions above unity indicate failure. These regions are localized in the pictures and hence ignored. In principle, these may be the regions of crack initiation and more work needs to be done in that respect. Also when the half angle of the root is changed from 45° to 30°, the stress in the root increases and the high stress region spreads to a greater region.

Figures 2-3(a) and (b) show the case of the 45° steel filler, and its replacement, the graphite filler, respectively. Although the figures show von Mises stress, the individual components of the stress tensor showed similar decreasing trend of the order of 20%, which indicates that the chosen root structure is expected to survive the 16000 rpm rotation requirement.

It may be noted that stress in the filler is not plotted here because the filler is in compression and the resulting stress on it is far below the failure level.

2.3.2 Location of Spars within Blade

The next problem was to determine the best location of the spars within the blade dimensions. This problem was complicated by the large number of parameters involved in the optimization problem. To simplify the problem, the deciding factor was limited to the tip (un)twist achieved by the blade actuation at rest condition (zero rpm). To find the actuation level at different spar locations, a finite element model of the active blade was built in PATRAN/NASTRAN in lines similar to that given in [7], with some refinements, as described below.

File Preparation for Blade Finite Element Model Construction

The plan followed for building the finite element model of the blade was as follows:

- Obtain the blade shape in electronic form that can be fed to PATRAN, thus producing the foam upper and lower surfaces.
- Decrease the thickness of the blade to get the upper and lower surfaces corresponding to the spar, known henceforth as the 'thin' blade shape.
- Cut the spars from the 'thin' blade shape, and

- Attach the root shape obtained from Section 2.3.1.

The most convenient format of producing the blade is the CAD form and the corresponding one for feeding to PATRAN is the IGES form. The reason why the blade model was not built in PATRAN directly was because this feature in PATRAN is not convenient.

A combination of MATLAB and PRO-ENGINEER was used to convert the coordinates of the Fan C blade given in [6], thus producing the foam upper and lower surfaces. It may be noted that PRO-ENGINEER is a commercially available CAD and FEM package with convenient model building capabilities. Its implementation and usage details are given in [17]. MATLAB ([15]) was used to input the blade coordinates in the syntax accepted by PRO-ENGINEER.

To get the spars, the thickness of the blade was decreased to be equal to the spar thickness. The blade and spar files were then loaded into the finite element package PATRAN/NASTRAN after being converted into the IGES format. Since the blade is twisted, the requirement of radially oriented spars needs extremely large and time consuming computation to determine the exact spar paths, especially when the distance between the spars is varied and tip (un)twist calculated for each instance. To simplify matters, the spars were cut parallel to each other, keeping the necessary distance between them. To do this, a surface was created at the level corresponding to a quarter of the thickness of the 'thin' blade from the pressure side and this surface was cut at the proper location to form spar elements. This simulates the condition that the foam is attached to the spar from the pressure side only. The reason for doing so is given in Section 6.2. Also, a wedge-shaped base of the dimensions found in Section 2.3.1 was attached to the spars through a transitional element.

Finite Element Discretization

The discretized model and its details are shown in Figure 2-4. Standard elements available in PATRAN/NASTRAN library were used to discretize the different parts of the blade. Solid elements (CHEXA) with eight nodes and six degrees-of-freedom (dof) per node were used for the foam, root and the transition element. Plate elements (CQUAD4) with four nodes and six dof per node were used for the spar plies and piezoelectric actuators. The spar elements were surrounded on all sides by foam elements, except for the suction side where there was no foam. The foam solid elements were arranged to have sharp leading

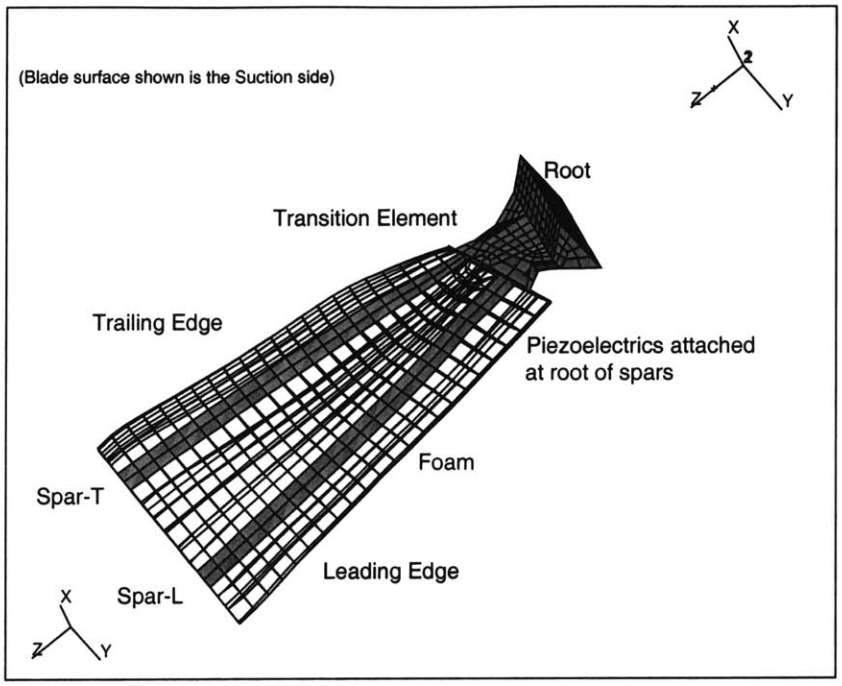

(a) Blade FEM

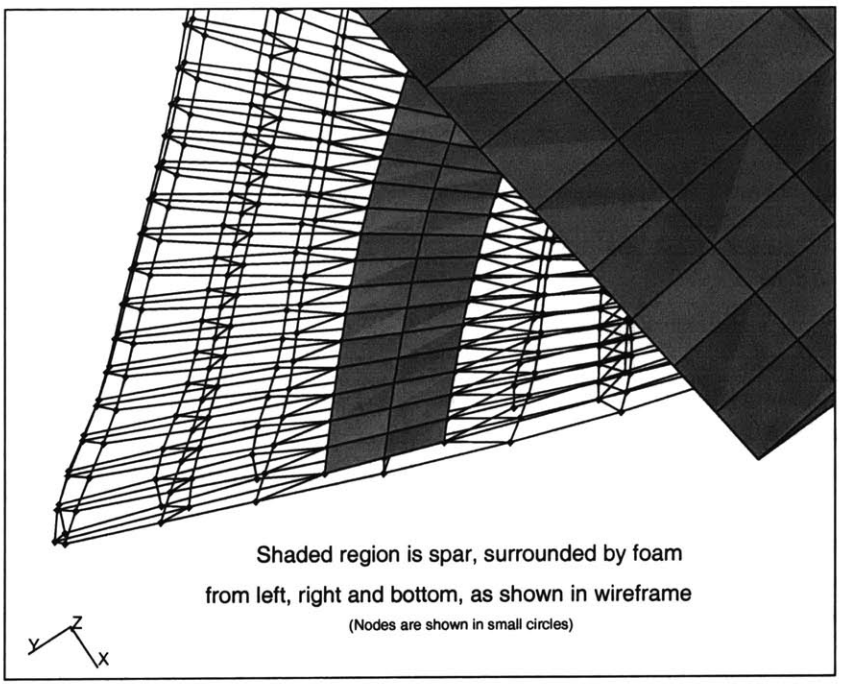

(b) Spar-Foam connection

Figure 2-4: Finite Element Model of the Active Rotor Blade (adapted from PATRAN).

and trailing edges. Although the edge shape affects the aerodynamics, it does not influence the structural analysis of the blade.

In the old model given in [7], the spar and actuator elements used coincident nodes with an offset defined for the actuators whereas in the new model, the piezoelectric wafer was considered a part of a composite spar-piezoelectric layup, as explained in the next section. Also in the old model, the spar and foam elements were joined at the nodes by rigid bars (RBE2) whereas the spar and foam nodes were coincident in the new model. Both these changes were done for convenience and also to eliminate the error due to rigid body associated singularities in the finite element matrices.

Material

The actuator and foam elements used isotropic materials (MAT1) . The root and transition element used equivalent three-dimensional anisotropic properties, derived from the composite layers, they were constructed from. This is because PATRAN does not allow composite material properties to be associated with solid elements (CHEXA), as mentioned before. However, PATRAN allows composite materials (PCOMP) to be built from any material with any ply thickness and ply orientation. So, a composite material system was created for the spar and piezoelectric systems (shown in Table 2.1).

Table 2.1: Assembly of spar layers to simulate twisting of blade by actuation through equivalent thermal effects. Here CTE refers to coefficient of thermal expansion and was also kept zero for foam and root.

Leading edge spar			Trailing edge spar		
Entity	Ply angle	CTE	Entity	Ply angle	CTE
Piezoelectric	–	$-\alpha$	Piezoelectric	–	$+\alpha$
Graphite/Epoxy	$+20°$	0	Graphite/Epoxy	$+20°$	0
Graphite/Epoxy	$-20°$	0	Graphite/Epoxy	$-20°$	0
...	...	...	...	...	...
Graphite/Epoxy	$-20°$	0	Graphite/Epoxy	$-20°$	0
Graphite/Epoxy	$+20°$	0	Graphite/Epoxy	$+20°$	0
Piezoelectric	–	$+\alpha$	Piezoelectric	–	$-\alpha$

As explained in Appendix A, the piezoelectric effect has been modeled as a thermal expansion/contraction effect. By using positive and negative CTEs for piezoelectric actuators attached to the suction and pressure side of the spars, respectively, bending of the spars can

be achieved. Twisting of the blade results when the two spars bend in opposite directions while blade bending occurs when they bend in the same direction, as shown in Table 2.1. The spars taper from $[\pm 20°]_{6s}$ at the root to $[\pm 20°]_s$ at the tip, in steps of 2 plies. The actuators cover the 24 ply, 22-ply and 20-ply portions of the spars.

Appendix B gives all the material properties used in this finite element blade model.

Loading

The source of loading in the FEM was the 'equivalent' temperature of the piezoelectric actuators, due to an input sinusoidal signal of 220 V amplitude and frequencies of 0 to 1250 Hz applied out-of-phase to the two active spars. The method of applying this loading is explained in detail in [7] and Section 4.3.2, and the reason for applying 220 V signal is explained in Section 4.3.1. The bandwidth of 1250 Hz covers the first three modes of the blade. It may be noted that centrifugal loads were ignored in this study.

Boundary Conditions

The active blade is fixed to the rotor at the root through clips. Between the root and the clips are aluminum shims, which are glued to the root inclined surfaces to provide a gap for the blade wiring to pass through the inclined surfaces to the rotor without getting smashed. The blade wiring serve to power the actuators and transfer the sensor readings to the outside environment. So the shim regions of the root were clamped in the finite element model (Figure 2-5).

Analysis and Results

Frequency Response (SOL 108) was used to find the tip (un)twist characteristics of the blade with respect to the actuating signal frequencies for various interspar distances. It may be noted that because of the way the model was set up, a new PATRAN/NASTRAN model was created each time the interspar distance was changed.

Figure 2-6 shows the tip (un)twist angle for different frequencies of applied signal, for three interspar distances. Note that the interspar distances given are that between the midline of the spars.

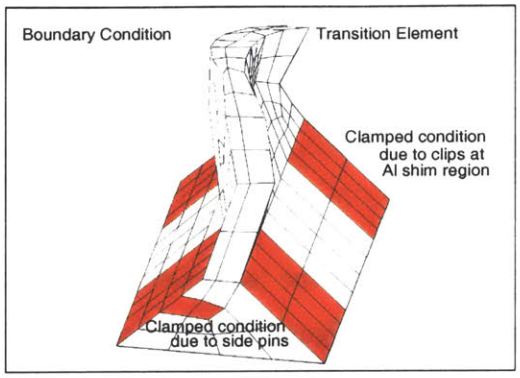

Figure 2-5: Boundary condition used in the PATRAN/NASTRAN model. Shaded region shows the fixed nodes. The root is fixed by the clips on the inclined surfaces and pins on the sides.

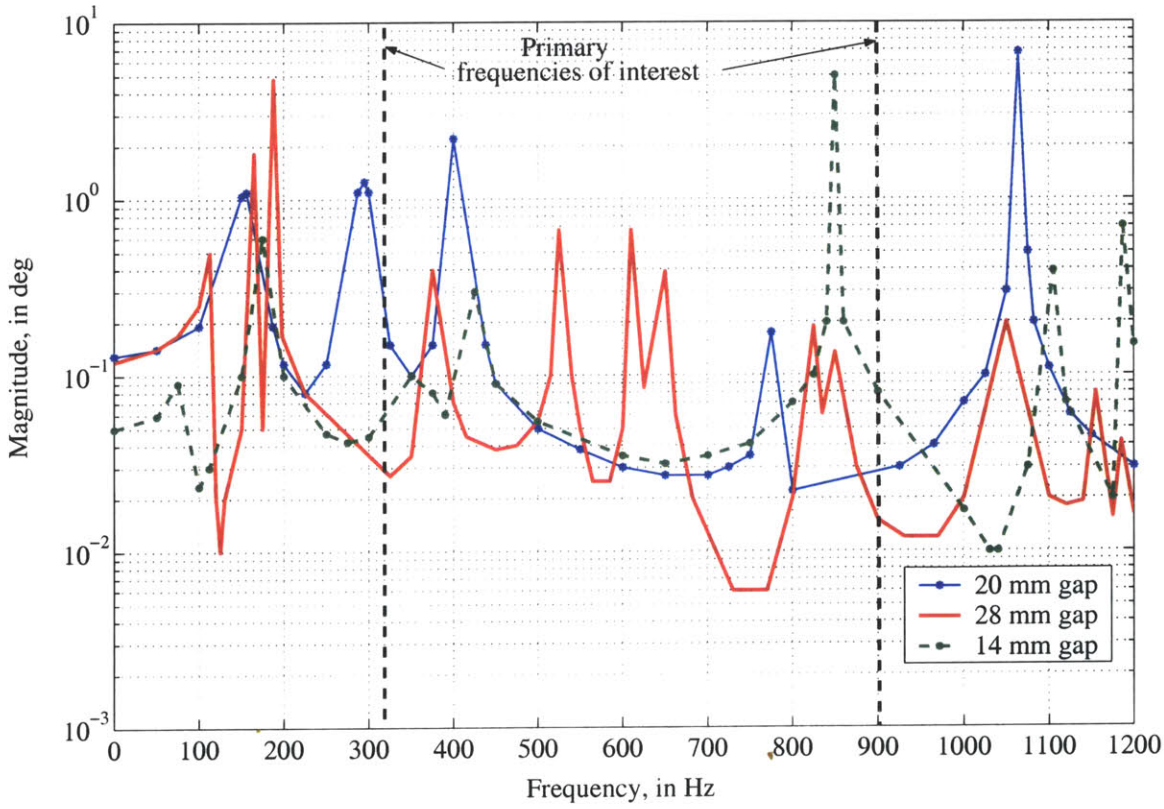

Figure 2-6: Tip twist of blade for various spar gaps as predicted by PATRAN/NASTRAN for input signal of 220 V. The blade was at rest condition (zero rpm).

It is clear from Figure 2-6 that the case of 20 mm interspar distance has maximum response at 330 Hz (the first bending mode of GE scaled Fan C blade) and good response at 900 Hz (the first torsion mode). This value of spar gap was chosen for manufacturing the active rotor blade.

2.3.3 Spar-Foam Bonding

The final unresolved issue was the investigation of the strength of the bond between the spars and foam. This was too complicated to be handled computationally because of the complex shape of the interface. That is why the bond between the foam and spars was assumed to be perfect in the finite element model. The other option of investigating the bond strength is experimental and is discussed in detail in Section 6.2. It may be noted, however, that one way of strengthening the bond is to increase the area of contact between the spars and foam, which can be done by including a small tab between the spars at the junction of the spars and the transition element. This is discussed further in Section 2.4.3 and illustrated in the FEM result shown in Figure 2-12.

2.4 Refined Finite Element Model of the Active Blade

The stage was then set for building the refined finite element model using the above information. The purpose of the model was to verify the integrity of the blade design under 16000 rpm and to find its bending and twisting characteristics due to actuation. The effect of introducing the tab was also analyzed. Finally, the effect of aerodynamic loads on the blade was studied.

2.4.1 Model Description

The model was built along the lines described above, except for two differences. One was the way the spars were cut from the 'thin' blade. It has been mentioned before that the spars should emerge radially from the rotor hub. Since the blade is twisted and bent in shape, it is difficult to satisfy this objective throughout the spar length while maintaining the desired distance between spars within the blade. Hence the radial direction was maintained for as long as possible from the tip while the spars were cut from the 'thin' blade surface and the required interspar distance was maintained only near the base.

The other difference was the loading condition. In this case, centrifugal load corresponding to 16000 rpm (267 rev per sec, in PATRAN) was applied at each node of the blade to find the stress and strain levels in the blade. The 'equivalent' temperature load was applied in the case where frequency response was desired. However, both loads were not applied simultaneously in the model (see discussion in Section 2.4.6).

2.4.2 Analyses

The following analyses were conducted:

- Static linear analysis (SOL 101) was used for obtaining the static stresses and strains on different parts of the blade. However, it was found that the tip twist of the blade was large and beyond the geometric linear assumption. Hence the next solution technique was followed.

- Static nonlinear analysis (SOL 106) was then used for finding stresses/strains, with the option of increasing loads in steps following the blade deflection.

- Frequency Response (SOL 108) was used for finding the bending/twisting capabilities of the blade at rest condition in the presence of a sinusoidal signal of constant amplitude 220 V and frequencies of 0 to 1250 Hz applied to the actuators.

2.4.3 Results

The results for the different studies are outlined below and summarized in figures at the end of the chapter. von Mises tensor quantities were used in the results to facilitate comparison between various models and failure strengths. Although it may not be suitable for composite material failure analysis, it is considered representative for the present analysis.

Stress in Spar

The maximum operating stress faced by the spar during rotation at 16000 rpm was found to be 219 MPa (Figure 2-8). Figure 2-7 shows the failure stress in the spanwise direction of the $[Piezo/(\pm\theta)_6]_s$ layup (which corresponds to the spar root cross section) for various fiber angles as well as the maximum operating stress. The failure stress for various fiber angles has been obtained from [7]. Clearly, the earlier choice of $\pm 20^\circ$ is safe from the point

of view of structural integrity and hence was maintained throughout the project. It may be noted that the operating stress of 219 MPa is much lower than that predicted by the older model because the distance of the origin of rotation axis from the blade base was updated from 96 mm to 89 mm in the new model. This updating was necessary in light of the new hub and clips design of the blade.

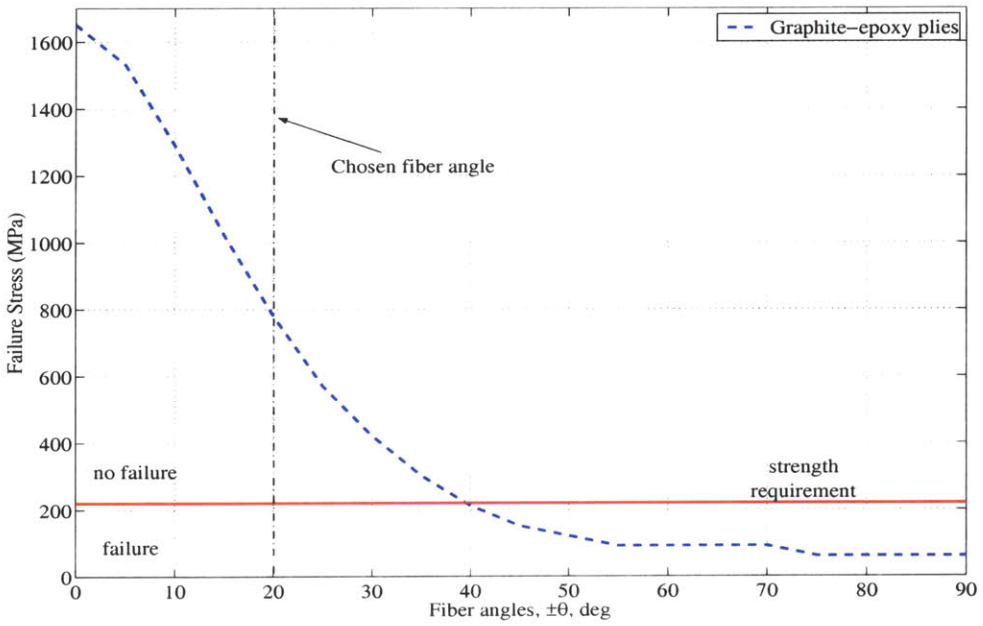

Figure 2-7: Effect of layup orientation on the strength of the blade spar.

Untwist due to Rotation

As the blade rotates, it tries to untwist and straighten out from its original shape. The amount of untwist at 16000 rpm can be estimated from the FEM deflection result shown in Figure 2-9. Those displacements translate to an untwist angle of 17.9° (obtained by dividing the sum of deformations of the extreme points of the blade tip by the length of the tip). The expected untwist should be introduced in the jig shape used for preparation of the active rotor blade so that the blade attains the shape of GE Fan C blade at the required speed. However, the specimen that is referred to in this thesis does not have the extra pretwist built into it.

Strain in Actuators

The new finite element model predicted that the strains experienced by the piezoelectric actuators under 16000 rpm centrifugal load exceed the failure limit of 2000 $\mu\epsilon$ by about 2000 $\mu\epsilon$. Figures 2-10(a) and (b) show that the higher strains are localized at specific spots. The high strain regions have been ignored in the present analysis but should be addressed in a future 'production' blade.

The actuators are expected to survive these loads after being packaged in copper-Kapton, as indicated by the actuation-under-tensile-loading tests presented in [7]. The reference explains that this piezoelectric strength extension may be due to the coating of the piezoelectric wafer surfaces with the flexible adhesive and polymide (Kapton) cover. This possibly allows microcracks to be formed and joined back, relieving some of the excess strains and maintaining the actuation characteristics of the wafer.

Stress in Foam

Figure 2-11 shows that the von Mises stress in the foam is below the Rohacell WF200 tensile strength of 12 MPa (986 psi). The higher stress level shown near the base of the foam and along the spar region is actually the element stress of the spar. This was plotted in the figure because the spar element shares its four nodes with the foam ones and so it was not possible to separate the spar element results from the foam in that figure. It is also noted that the stress at the spar plate element is lower than that in the plies because the former was calculated in the mean plane of the spar cross-section.

Structural Effects of Tab

The presence of the tab does not cause significant change in the stress/strain in the blade, as shown in the FEM results of Figures 2-12 to 2-15. The maximum increase in the spar stress is about 13% while that in foam is about 1%. The results for the strain decrease in the actuator is 2% and the untwist due to rotation is 0.1% with the presence of the tab.

2.4.4 Structural Effects of Aerodynamic Loads

A reduced order aerodynamic model from [20] was used to estimate the aerodynamic pressure at 70% span (measured from base of foam) on both the suction and pressure sides. The

flow was assumed to be at Mach number 0.70 with the flow angle being 61°. This pressure was transferred to the nodes of the foam by assuming a quadratic trend from the base of the foam to the tip. The reason for the quadratic trend is that the air speed increases as square of distance from the base of the foam.

The aerodynamic pressure distribution at 70% span is shown in Figure 2-20 and the FEM results at 16000 rpm are given in Figures 2-16 to 2-19. Although centrifugal loads dominate the stresses, there are some significant differences when aerodynamic loads are introduced. For example, even though there is a 15% increase in the stress level in the spars and 2% increase in case of foam, the high stress fringes cover more areas when the aerodynamic loads are introduced than in the purely rotational case. This is expected because the aerodynamic loads induce bending in the blade. In case of the actuators, the pressure side actuators have more strain than the suction side, which is opposite of what happens in the purely rotational case, although the strain levels reached are similar. The deformation plot shows clear bending of the blade by about 15.5° (obtained by dividing the average tip deflection by the blade length from the base of the spars). Overall, the blade is expected to survive the rotation environment in the presence of airflow.

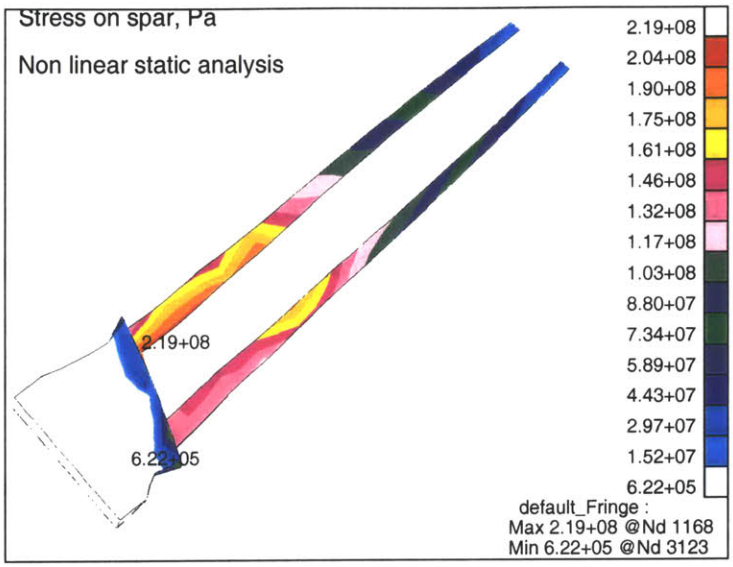

Figure 2-8: von Mises stress in spars at 16000 rpm, as predicted by the refined FEM. No tab is present and the numbers on the spar show the extreme stress regions.

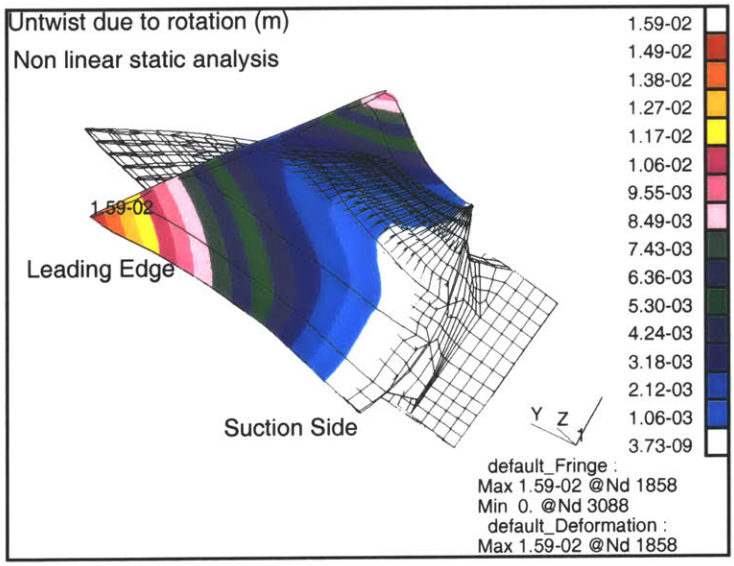

Figure 2-9: Untwist of the blade at 16000 rpm, as predicted by the refined FEM. No tab is present and the number on the blade indicates the maximum untwist region.

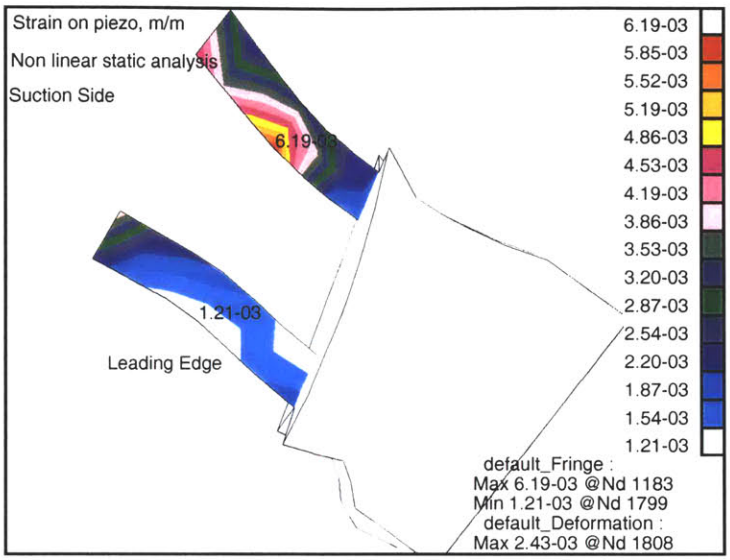

(a) von Mises strain in piezoelectric actuator – suction side

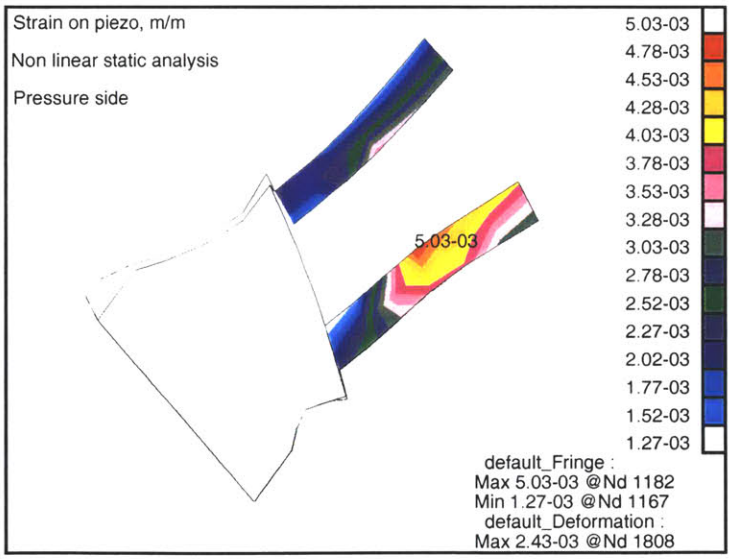

(b) von Mises strain in piezoelectric actuator – pressure side

Figure 2-10: Effect of 16000 rpm on the actuators, as predicted by the refined FEM. No tab is present and the numbers on the actuators show the extreme strain region.

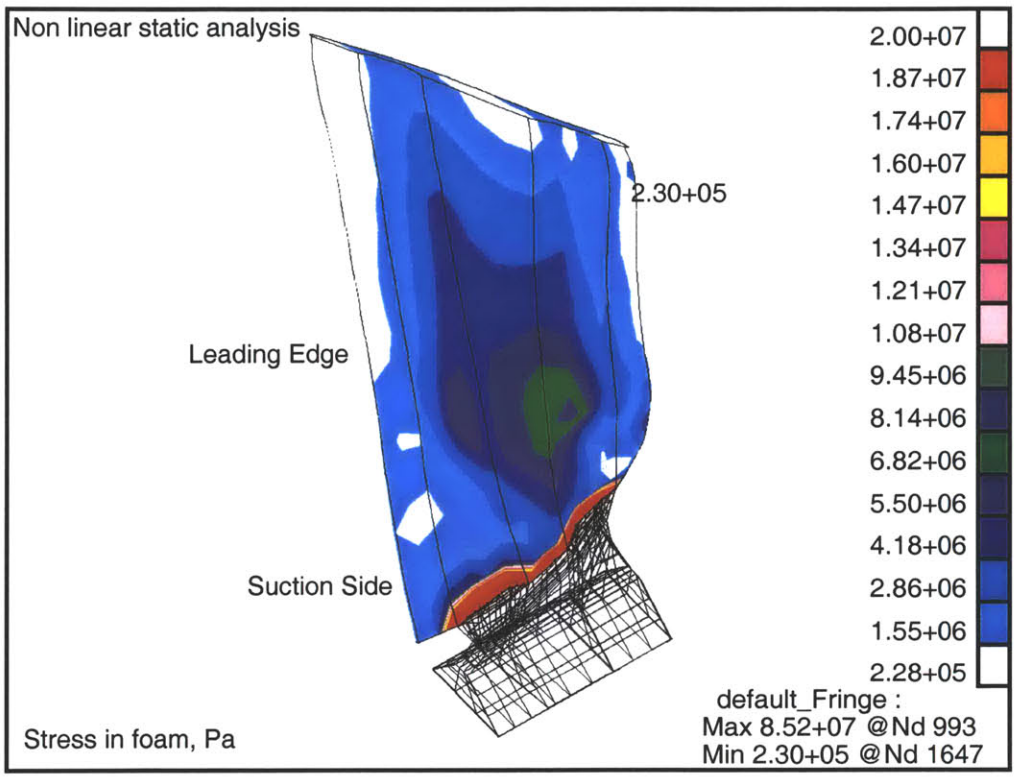

Figure 2-11: von Mises stress in foam at 16000 rpm, as predicted by the refined FEM. No tab is present and the number on the foam shows the maximum stress regions.

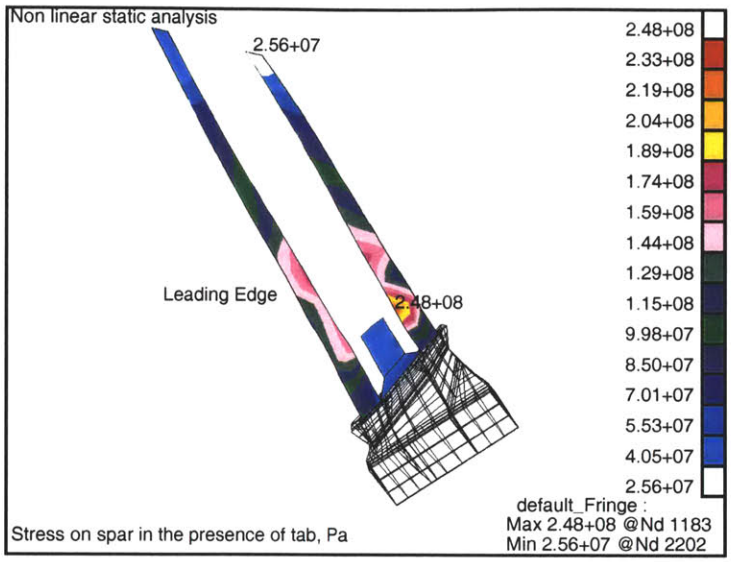

Figure 2-12: von Mises stress in spars with tab at 16000 rpm, as predicted by the refined FEM. The numbers on the spar show the extreme stress regions.

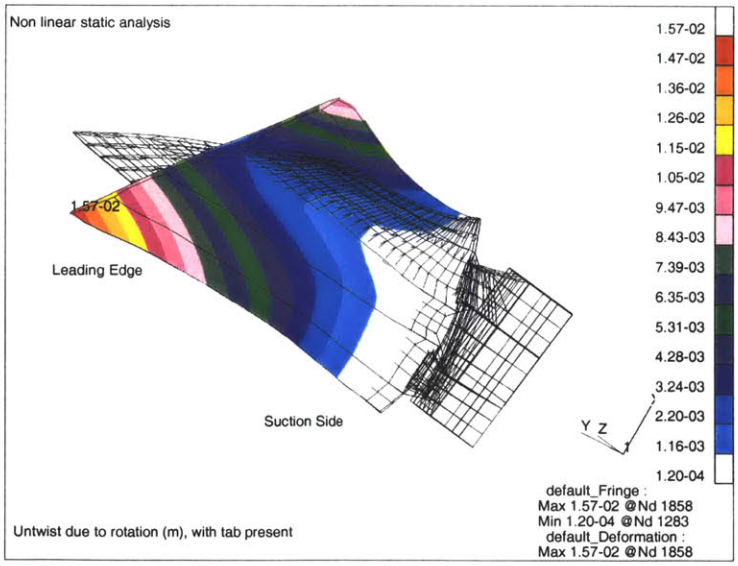

Figure 2-13: Untwist of the blade with tab at 16000 rpm, as predicted by the refined FEM. The number on the blade indicates the maximum untwist region.

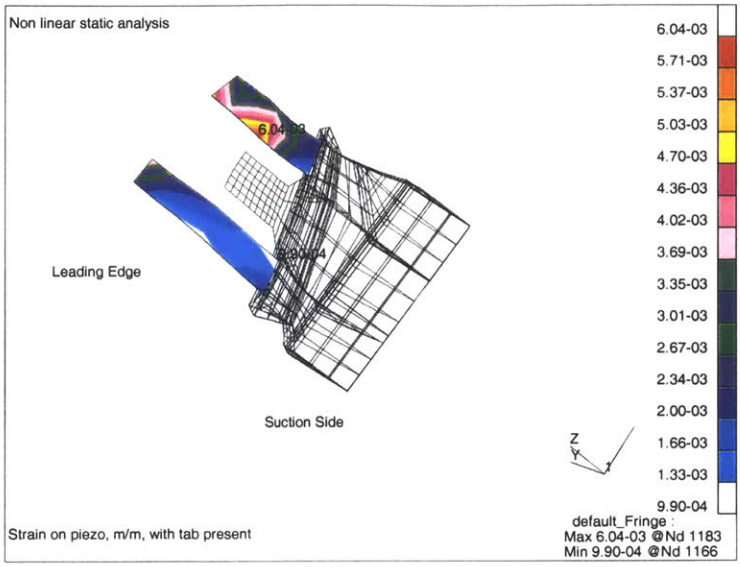

(a) von Mises strain in piezoelectric actuator – suction side

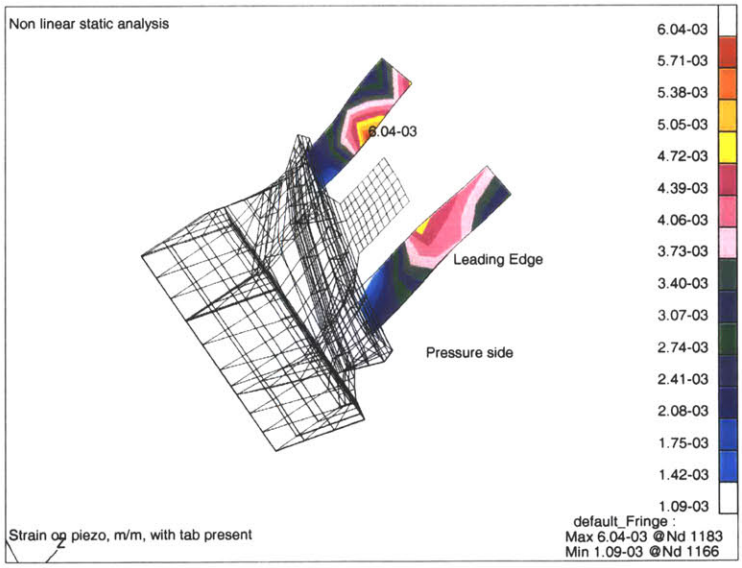

(b) von Mises strain in piezoelectric actuator – pressure side

Figure 2-14: Effect of 16000 rpm on the actuators with tab, as predicted by the refined FEM. The numbers on the actuators show the extreme strain region.

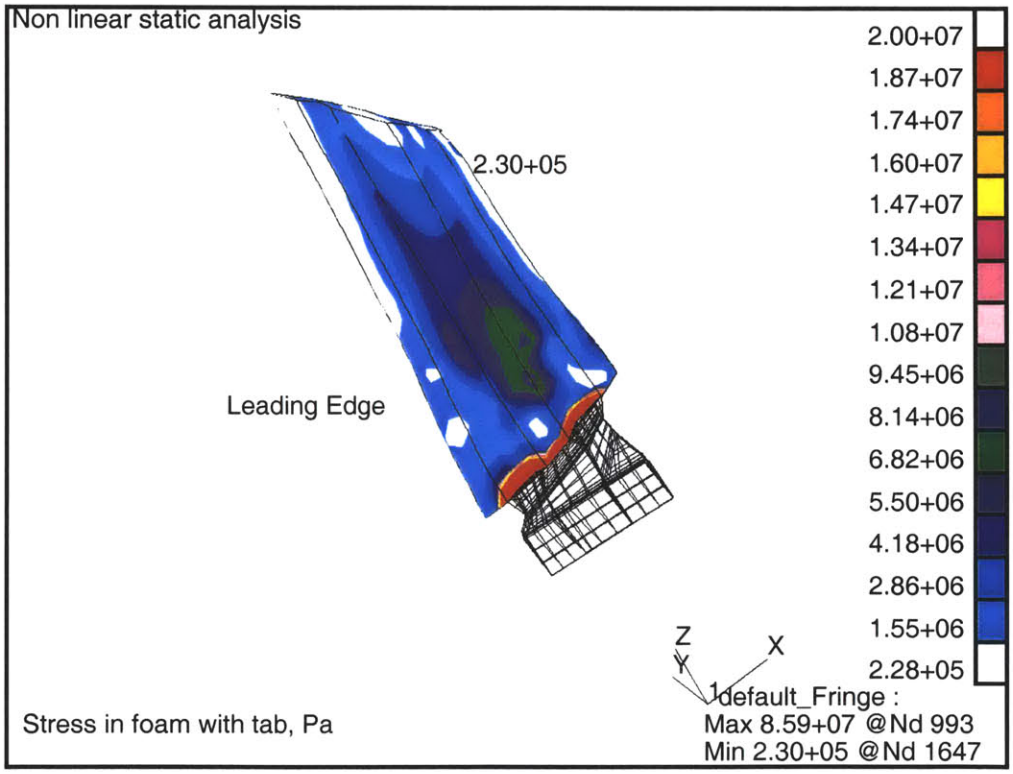

Figure 2-15: von Mises stress in foam with tab at 16000 rpm, as predicted by the refined FEM. The number on the foam shows the maximum stress regions.

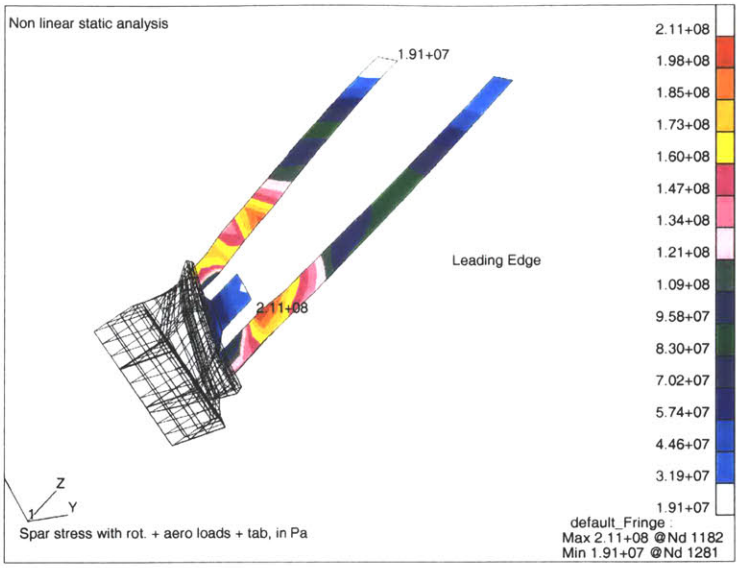

Figure 2-16: von Mises stress in spars with tab and aerodynamic loads at 16000 rpm, as predicted by the refined FEM. The numbers on the spar show the extreme stress regions.

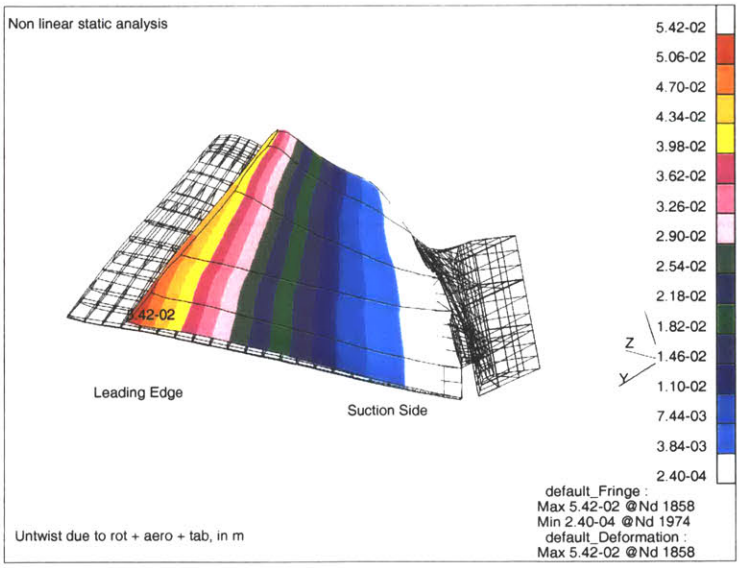

Figure 2-17: Untwist of the blade with tab and aerodynamic loads at 16000 rpm, as predicted by the refined FEM. The number on the blade indicates the maximum untwist region.

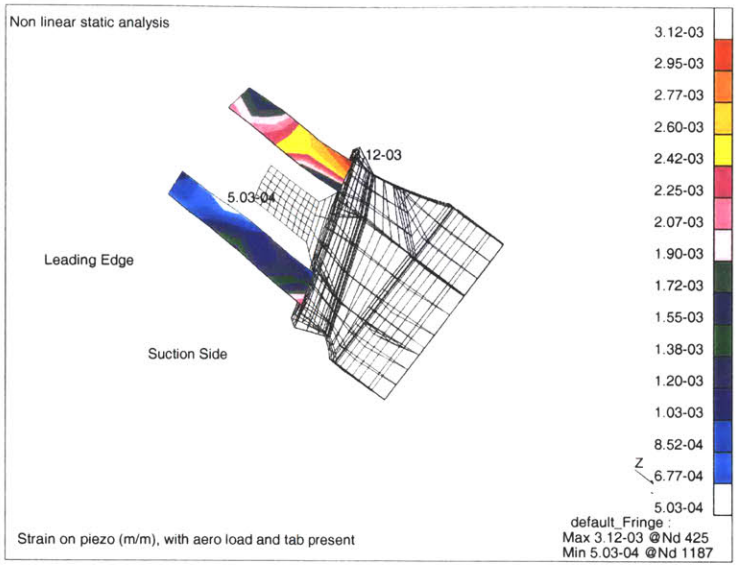

(a) von Mises strain in piezoelectric actuator – suction side

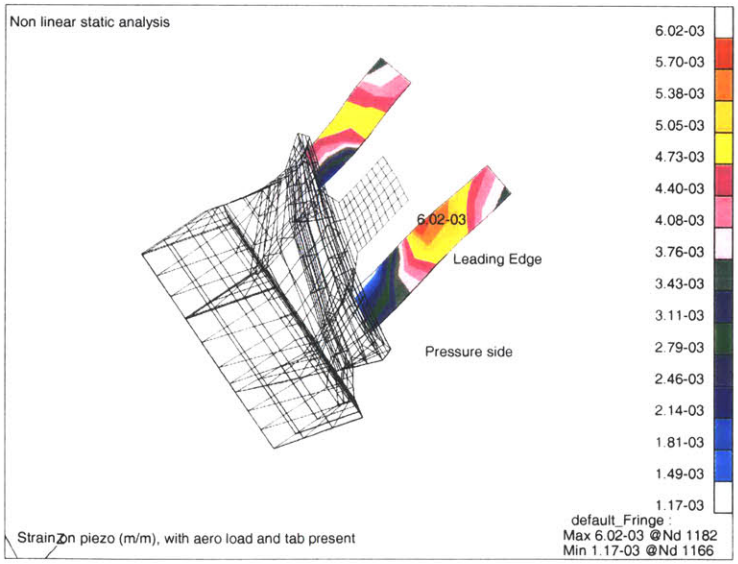

(b) von Mises strain in piezoelectric actuator – pressure side

Figure 2-18: Effect of 16000 rpm on the actuators with tab and aerodynamic loads, as predicted by the refined FEM. The numbers on the actuators show the extreme strain region.

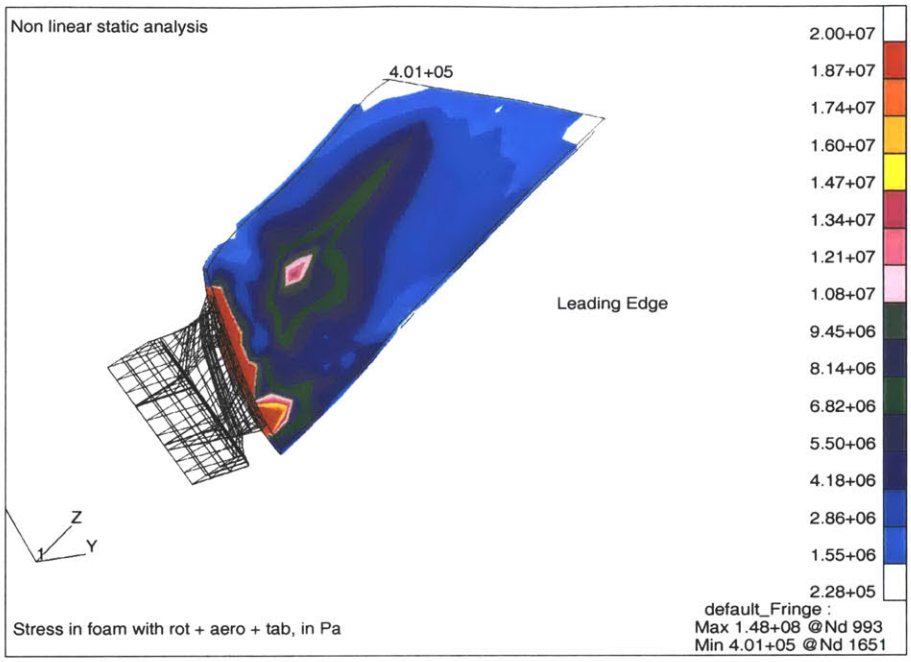

Figure 2-19: von Mises stress in foam with tab and aerodynamic loads at 16000 rpm, as predicted by the refined FEM. The number on the foam shows the maximum stress regions.

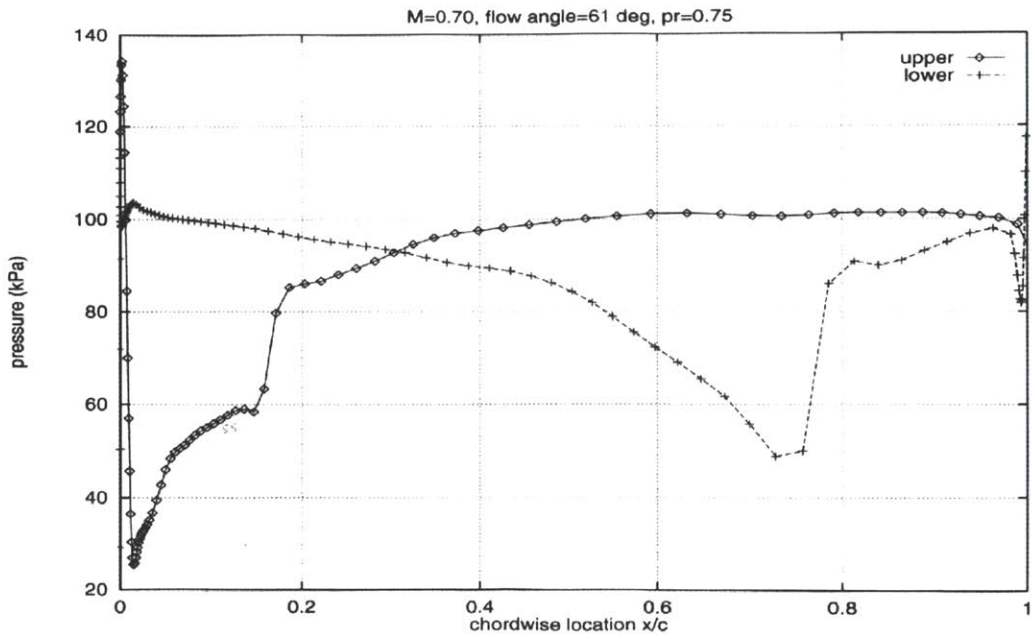

Figure 2-20: Aerodynamic load at 70% span.

2.4.5 Blade Performance

Frequency response analysis was done using the PATRAN model for estimating the blade tip twist and bending level. This was conducted by actuating the piezoelectrics at 220 V at frequencies between 0 and 1250 Hz. The plots are shown in Figure 2-21. The requirement for each case is also shown in the figures. It may be noted that the tip twist and bending plotted in the figures are averaged over the entire tip chord.

Clearly, the blade performance does not match with the requirement at all frequencies, except at some of the poles. In spite of this fact, manufacturing and testing of this blade configuration was commenced. The reason is as follows. The actuation-under-tensile-loading tests of [7] indicate that the actuation level is increased up to 1.5 times due to tensile loads once under rotation. In addition, the 220 V signal on the actuators can be extended to about 1.5 times by a method shown in Section 4.3.1. Although these actuation increases would not be enough to meet the requirements, it would provide an invaluable and robust experimental tool to perform control studies on flutter and estimate aerodynamic loads on a scale much larger than presently achievable, although lower than the initial target. Moreover, with further development of piezoelectric material systems, higher authority actuators can replace the current ones in use.

2.4.6 Limitations of the FEM

Lastly, it would be instructive to keep the following limitations of the blade FEM in mind while using its results.

Geometry Mismatch: There is about 10% mismatch in shape between the spars in the model and the one tested because of manufacturing errors. Secondly, there is again a 10% difference in the positions of the actuators in the model and the experimental specimen because of slippage of the actuators while being bonded to the spars. Lastly, the demarcation of the 24-ply region, 22-ply region, etc. in the spars is difficult to verify in the experimental specimen because they are not visible from the outside.

Rotation Effect on Frequency Response: It is extremely difficult to run Frequency Response analysis with the centrifugal loads present, primarily because PATRAN considers centrifugal loads as external loads and does not convert them into added mass terms of the form $M\omega^2 r$ in the left side of the governing differential equation

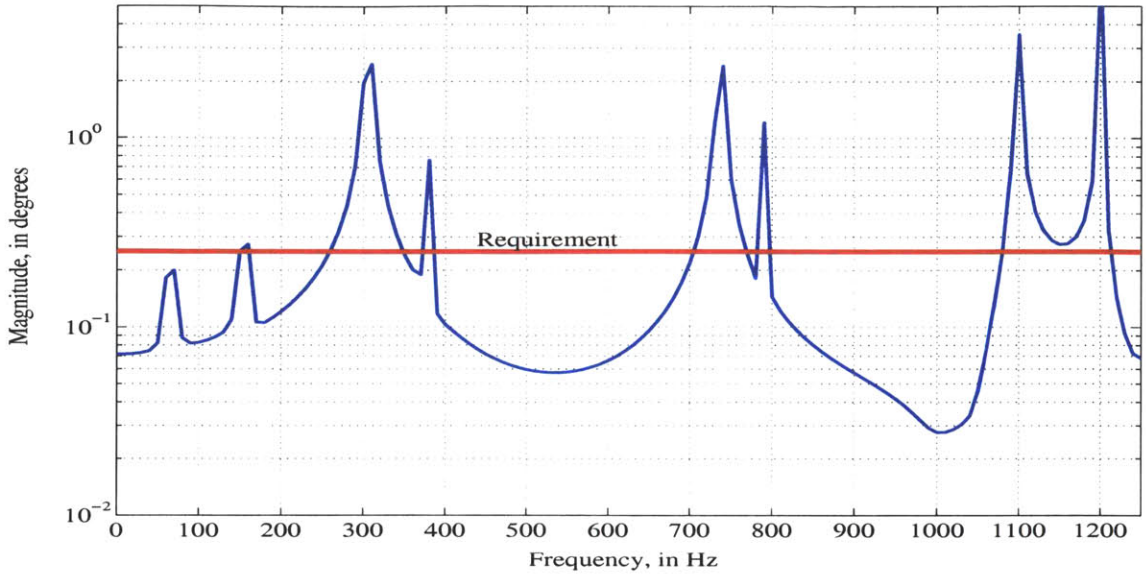

(a) Tip Twist Frequency Response

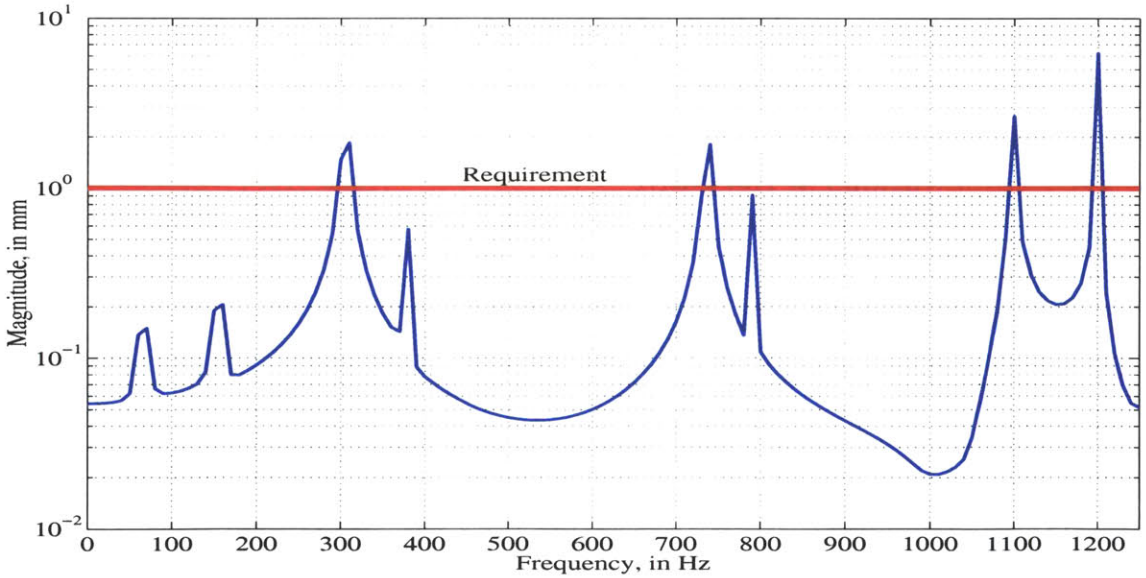

(b) Tip Bending Frequency Response

Figure 2-21: Predicted Frequency Responses of the blade at rest condition (zero rpm) and 220 V excitation.

A.10. Owing to the large size of the model, modifying the NASTRAN datafile to run SOL 108 over SOL 103 (that is, using results of the static non-linear rotational analysis as initial condition for the frequency response analysis) was not feasible within the timeframe of this work.

Optimization: It is equally difficult to make structural changes in the model because of the way it has been set up. This hinders the capability of optimizing the structural parameters of the model. The limitation faced while finding out the best spar location in Section 2.3.2 can be taken as a good illustration of this problem.

The finite element model may need to be updated to reflect the real manufacturing limitations explained above. To obtain the frequency response in the presence of rotation, either the analysis can be done in a finite element package where this capability is available, or codes in PATRAN language (PCL) may be written for doing the RERUN of SOL 108 over SOL 103. As regards to optimization, again writing codes for generating the various parts of the model, instead of doing them manually, will help.

Chapter 3

Spar and Filler Manufacture

Having completed the design of the blade, the attention now shifts to the manufacturing issues of the spar and graphite-epoxy root filler. At the end, a tensile pull test will be discussed to verify the integrity issue of this root system in the presence of tensile load equivalent to 16000 rpm centrifugal force.

3.1 Manufacturing Steps

The steps adopted for the manufacturing of the blade structural members were as follows.

- Manufacture of root filler from graphite-epoxy prepreg.
- Preparation of aluminum spar molds for realizing the spar manufacturing process.
- Manufacture of twisted spar-plate from graphite-epoxy prepreg.
- Cutting of spars from the plate.

3.2 Manufacture of Root Filler

The plan followed for filler manufacturing process was to get a brick-shaped graphite-epoxy ply layup, cure and cut it into wedge shaped fillers. As discussed in Section 2.3.1, a quasi-isotropic layup was used: $[0/+45/-45/90]_{10s}$ and was of length 4" x 6". The standard procedure for curing a straight untwisted graphite-epoxy plate is available in [18], the manual used in the MIT's Technology Laboratory for Advanced Composites (TELAC) where most of the manufacturing was done.

The layup was cured under straight aluminum molds in the TELAC autoclave; however, after the cure, it was observed that there was a considerable taper in the brick cross section at the ends. The tapered regions were cut off using the diamond-tipped wheel cutter of TELAC . Since the material is composite, standard steel cutters cannot be used. To get wedge shaped fillers, the brick cross section was cut along $\pm 45^{\circ}$ angles longitudinally and then the correct length chopped off. This was done in the diamond-tipped wheel cutter in MIT Central Machine Shop which has the facility of cutting along a 2-D plane. Figure 3-1 shows the graphite filler and illustrates the cutting path.

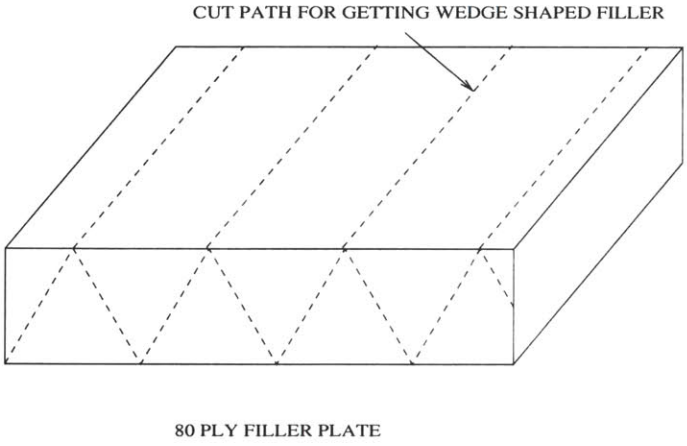

(a) Cut path to obtain filler

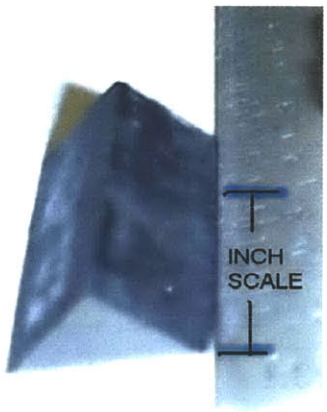

(b) Graphite-epoxy filler

Figure 3-1: Root filler for the active blade.

3.3 Manufacture of graphite-epoxy plate

3.3.1 Mold Preparation

The aluminum spar molds were prepared from the CAD files made for the spar. The CAD files were converted into MasterCAM, a format compatible with computer controlled numerical (CNC) machines available in MIT Central Machine Shop. The molds were machined from aluminum blocks of dimensions 8" x $5\frac{3}{4}$" x 3".

3.3.2 Manufacture of graphite-epoxy plate

Although the curing procedure for getting straight untwisted graphite-epoxy plates is given in [18], the difficulty was in modifying the procedure to get the desired twisted tapered shape of the Fan C blade. Several ideas were attempted. A promising one was to: (a) use graphite-epoxy [$\pm 20°$] fiber cloth and lay it on top of each other in decreasing lengths (to form the linear taper from root to tip), (b) repeat the layup and join the two to form a symmetric layout, and (c) cure it inside the aluminum molds under elevated temperature and pressure. The advantage of the cloth is that it is easy to deform. However there was not enough confidence in the composite community about accurate prediction of its elastic properties, and the material was not widely available in the laboratory. Hercules' AS4/3501-6 prepreg was the final choice.

An effort was first made to get a straight untwisted but tapered blade of same dimensions as the scaled Fan C. This enabled the establishment of the exact manufacturing technique for the twisted plate and the complete blade, as well as provides convenient specimens useful for experiments, such as the tensile pull test described in Section 3.4, the actuation test in Section 4.1.1, and the thermoform test in Section 6.3.

The graphite-epoxy prepreg was cut, laid out in a manner similar to the cloth process and then cured under elevated temperature and pressure in the autoclave. A steel block cut into a prismatic shape was used as the filler for the root. At that time, steel was chosen as the filler, although it was later changed to graphite for the twisted plate. After post-curing in an electric oven at high temperature, the straight plate was cut into spars using the water-jet cutter available at MIT's Laboratory for Manufacturing and Production (LMP). The tests done on the spars such as pull tests and thermoform tests (after attaching piezoelectric wafers to the spars and then attaching the spars to foam) proved that the procedure was satisfactory.

For the twisted tapered plate, the two symmetric halves of it were made from the prepreg cut to the lengths and orientations shown in Table 3.1. The transition element and root were made thicker than the spar root thickness by 8 plies. The extra plies were cut according to the dimensions shown in Table 3.2. To make cuts of accuracy ± 0.1", rulers with the appropriate least count and clean sharp knives were used.

Table 3.1: Length and orientation angle of plies cut for the twisted blade manufacturing process.

Ply number	Length (in)	Orientation (degrees)
1	8.0	+20
2	8.0	−20
3	7.3	+20
4	6.6	−20
5	5.9	+20
6	5.2	−20
7	4.6	+20
9	3.4	+20
10	2.8	−20
11	2.1	+20
12	1.5	−20

Table 3.2: Length and orientation angle of plies cut for root and transition element.

Ply number	Length (in)	Orientation (degrees)
1	3 x 3	+20
2	3 x 3	−20
3	3 x 3	+20
4	3 x 3	−20

By untwisting the blade shape, it was found that it closely matches a trapezoidal shape with a rectangular bottom. Hence the plies were cut accordingly. An outline for the shape of the plies is shown in Figure 3-2. The picture of the plies after layup is shown in Figure 3-3.

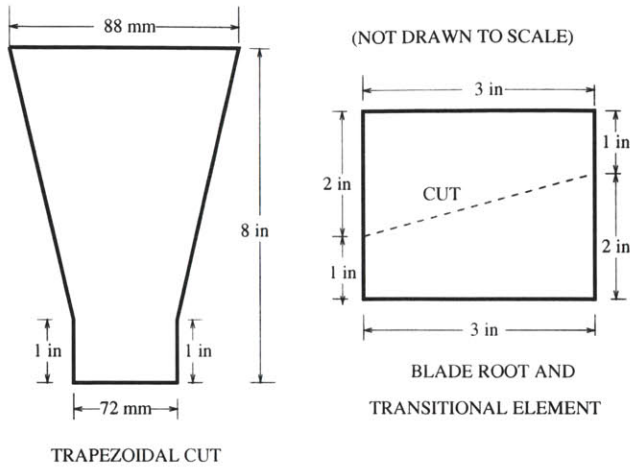

Figure 3-2: Outline of the ply cut for twisted plate, root, and transition element.

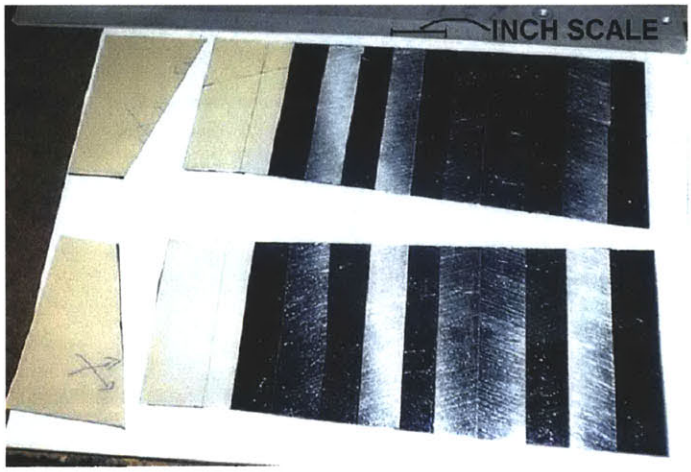

Figure 3-3: Prepreg layup for the twisted blade manufacturing process.

The plies were laid inside the cleaned aluminum molds coated with Dexter Frekote (to prevent glueing of plies to the mold) along with the graphite root filler structure. The plies were taped to the mold and the junction between the molds were taped by using blue flash tape. Figure 3-4(a) to (c) depict the layup process of the plate inside the molds.

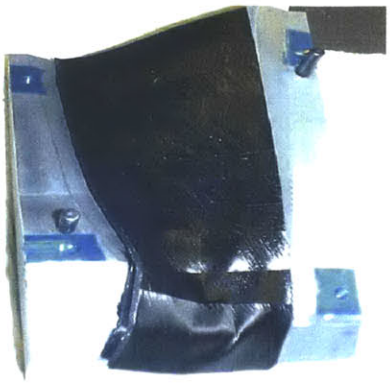

(a) Placing one of the layups on lower mold

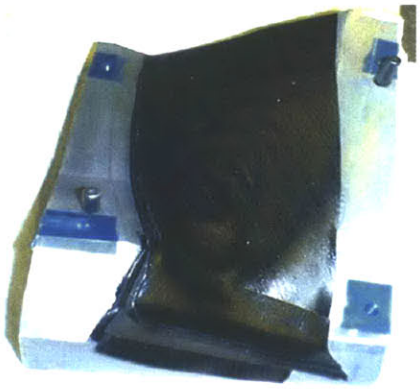

(b) Second layup on top of the first one

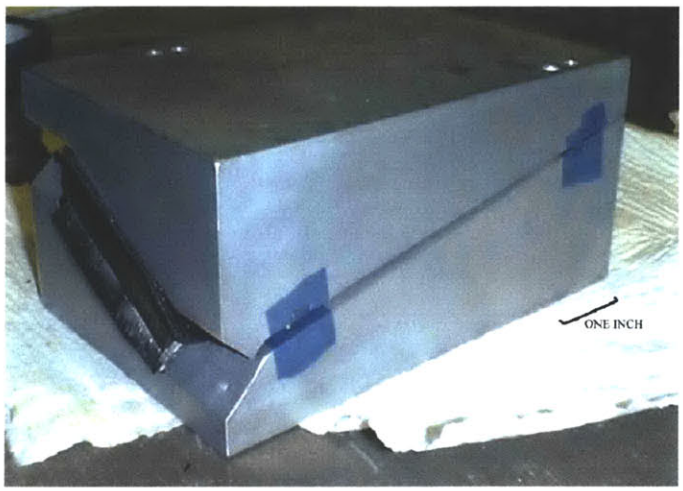

(c) Upper mold on top of the layups

Figure 3-4: Ply layup process of the twisted graphite-epoxy plate.

The molds were put inside the Heat Press in MIT's Active Materials and Structures Laboratory (AMSL). The Heat Press was chosen this time instead of the autoclave because the small size of the molds made the former much more convenient and quicker to use. The molds were kept in place by cork. The root filler was fixed in place by means of a steel block pushing against it and itself being held in place by cork. The whole assembly was covered with bleed paper and the cure cycle shown in Figure 3-5 was followed.

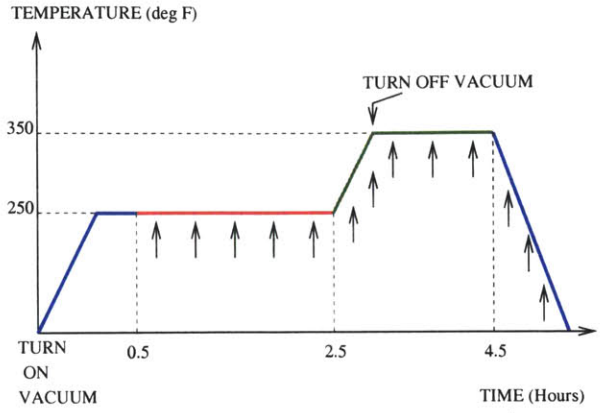

Figure 3-5: Cure cycle for graphite-epoxy plate manufacturing process.

As shown in Figure 3-6, two types of plates can be formed through this process – one with tapering from inside-out and the other with tapering from outside-in. When the taper is from outside, the flow of epoxy through the plate is not enough to cover the 'steps' created by the ply drops; as a result, the likelihood of failure due to crack propagation from the step edges (where stress concentration is highest) increases. When the ply drops are inside, the internal epoxy flow covers up most of the voids and thus, decrease the chance of failure. Hence, this was used during the active blade manufacturing process.

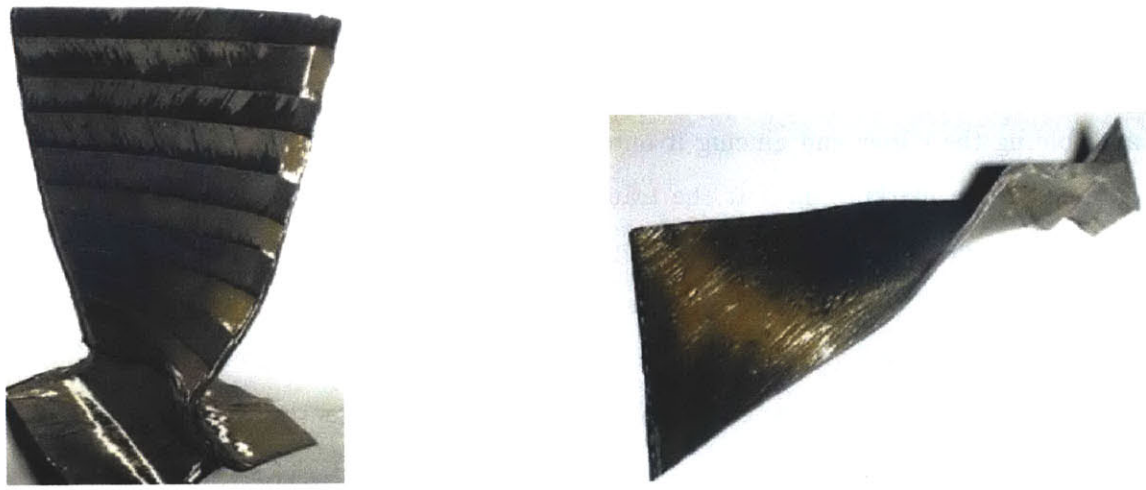

(a) Outside ply drops

(b) Inside ply drops

Figure 3-6: Two types of twisted graphite-epoxy plates formed during cure.

3.3.3 Obtaining Spars from the Plate

The process of obtaining spars from the plate is made difficult by the fact that the material is made of composite and so standard three-dimensional machines cannot be used for cutting the spars. The water-jet cutter of LMP is a potential solution but it cuts along a two-dimensional plane. So the image of the spar-plate can be projected onto the 'best' plane and the resulting image fed through the water-jet cutter. The 'best' plane is defined as that plane by virtue of which the deviation in the cutting path from the desired one is minimum. The deviation results mainly when the height of the water-jet source above the plate increases beyond a certain range and the jet starts diverging.

The other option is to use a hand-held cutting tool such as Dremmel. However, the spar cutting path needs to be marked on the curved blade surfaces before cutting can begin. There are at least two ways to accomplish this. One is to print a two dimensional image of the spar on transparency and project it onto the spar-plate, as shown in Figure 3-7(a). Although simple in theory, on executing the procedure, it was not found to be feasible as the quality and position of the projected image was sensitive to the distance and elevation of the spar-plate from the projector. Also the projector distorted the image significantly. Because of unavailability of better optical equipments, this method was discarded. The second way of creating spar paths is to discretize the spar into small triangles and print it on paper; the resulting image of one spar discretization is shown in Figure 3-7(b). By suitably cutting and folding the paper and glueing it onto the spar, a more accurate spar path would be obtained. The marking lines at the transition elements would serve as reference for the paper; however, the spar-path obtained this way is very sensitive to the placement of the paper at the root (used as the reference here). Once the spar path is obtained, the spars can be cut from the plate by a combination of cutting using Dremmel and sanding. To prevent local overheating, the cutting should be done intermittently.

The combination of glueing paper and cutting by hand was tried on one of the twisted graphite plates and it was found that the process does not yield very precise spars. Since water-jet cutting seems to be a promising option, it deserves further attention. In this thesis, the work on twisted spars is based on the specimen manufactured by hand.

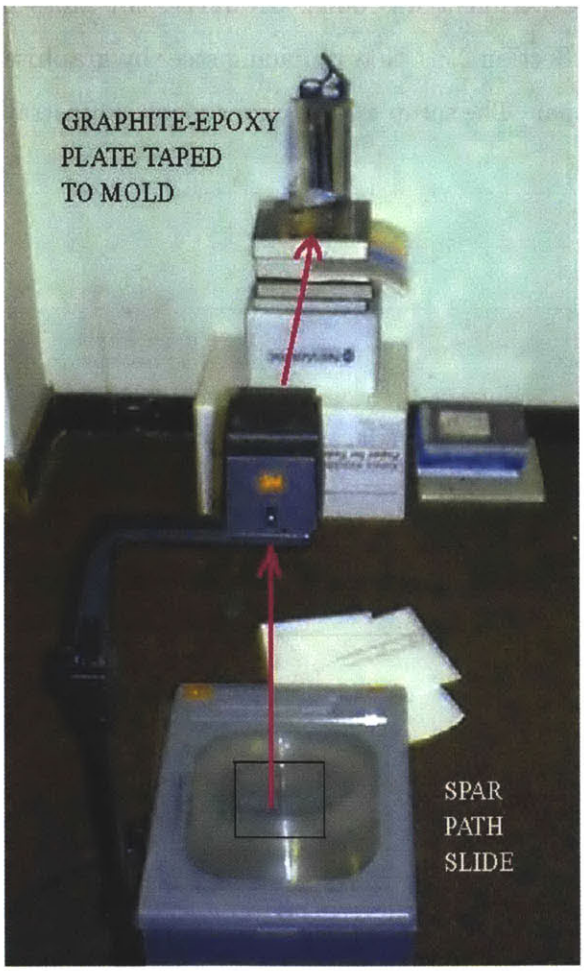

(a) Projection method. Uses the mold to hold the spar-plate.

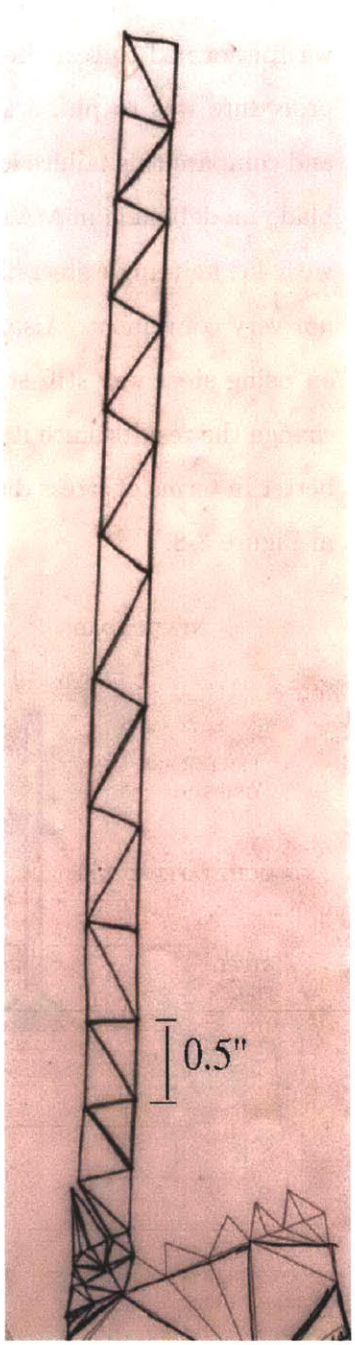

(b) Discretizing spar into triangles.

Figure 3-7: Two methods of impressing the spar outline onto the curved surface of the graphite-epoxy plate.

3.4 Pull Test

Having got the spars (both straight and twisted ones) with attached root, an experiment was performed to test the strength of the spar root at 16000 rpm equivalent loading. The procedure was to pull a straight graphite-epoxy spar with an attached root until failure, and compare this failure load with the 16000 rpm operating load obtained from a simplified blade model made in MATLAB (given in Appendix C). For this test, the straight specimen with 45° half-angle steel filler was used. It may be noted that pulling on the twisted spars is not very convenient. Also, steel filler was used instead of a graphite one, since the decision on using steel was still standing while the experiment was done. However, this does not change the results since it has been found in Section 2.3.1 that replacing steel by graphite is better in terms of stress distribution on the spar. The setup for the experiment is illustrated in Figure 3-8.

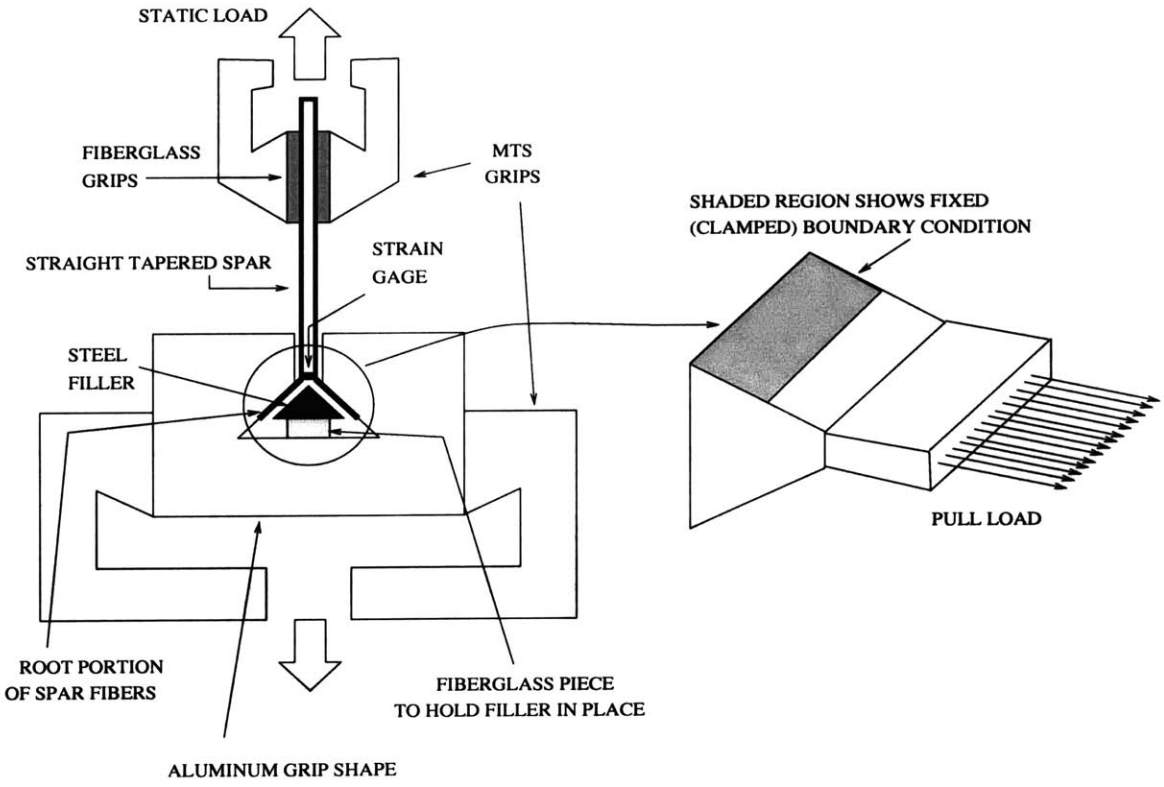

Figure 3-8: Setup for the pull test done in MTS Instron Machine and boundary condition on spar.

The specimen was pulled in the MTS Instron Machine of TELAC and strain was measured by a small gage at the base of the spar near the root. Fiberglass pieces were attached to the spar tip, which was in between the MTS grips, in order to prevent crushing of the spar. A special aluminum grip was prepared for holding the root structure. During the test, it was observed that the steel filler slipped from the spar. Hence the filler was forced into the spar base and kept in place by fiberglass pieces wedged in between the filler and the special aluminum grip shape. This simulates the spring action with which the active blade is held in place inside the hub. Also the two arms of the root close together when the spar is pulled and so the filler is held in place more tightly. Hence this is not expected to affect the result of the experiment in a detrimental way.

Figure 3-9 shows the results of the pull test and the failure mode of the specimen. As expected from the FEM, the spar started to rupture at the pointed tip of the filler where stress concentration was the highest. The centrifugal load estimated by the MATLAB code given in appendix C is 118 lb (525 N) and it is much less than the failure load of 172 lb (765 N). The conclusion is that the root manufactured this way is expected to hold the blade in place up to 16000 rpm operating condition.

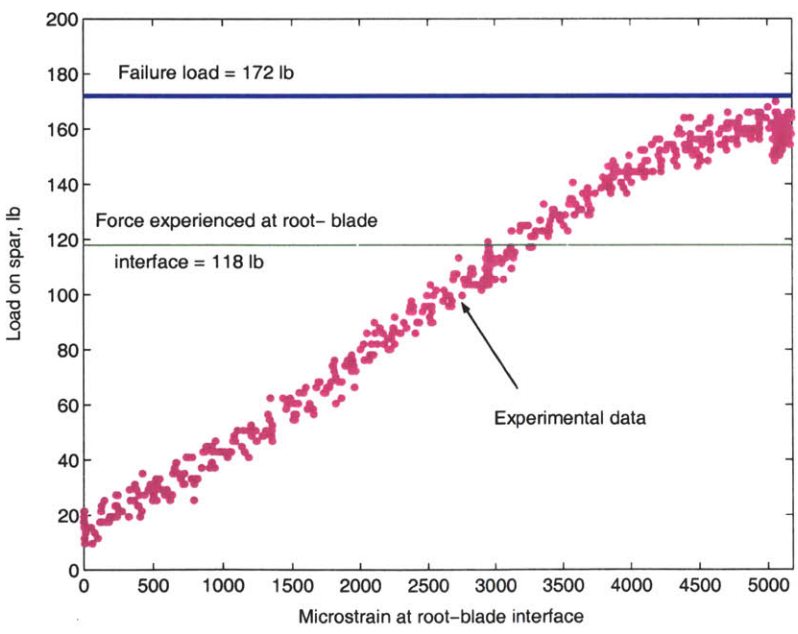

(a) Strain gage history during pull test.

(b) Specimen after pull test.

Figure 3-9: Results of pull test of straight spar with root.

Chapter 4

Actuator and Sensor Preparation and Blade Wiring Characteristics

This chapter will deal with the issues related to the piezoelectric actuator packaging and the sensors used in the blade along with the problems faced during their development. The characterization tests of the actuators before bonding them to the spars are discussed next. The chapter then talks about the issue of bonding of piezoelectric wafers to the twisted spars and the problem of implementation of precompression. Finally, recommendations are made for improvement in the active wired spar construction method.

4.1 Piezoelectric Actuator Packaging and Blade Wiring

The PZT-5A wafer cannot be used as actuator directly off-the-shelf. Although it is nickel-coated on both surfaces, electrical leads need to be developed to conveniently apply the desired electrical fields to the actuator. As given in [7], the following requirements need to be satisfied by the actuators:

- They should be lightweight; additional weight increases centrifugal loading on the blade.
- They should be thin; otherwise the spar thickness needs to be reduced.
- They should be flexible enough to be wrapped around the twisted spars, transition element and root.

- They should be electrically isolated from the underlying spar whose material (graphite) is electrically conductive.

Single-sided copper-coated Kapton, from American Durafilm, of thickness between 0.5 and 3 mil (0.127 and 0.762 mm) satisfies all these requirements and was chosen for packaging. The copper was etched away using PCB Echant to get the desired lead shape.

4.1.1 Problems with Old Wiring System

In [7], the initial tests with straight spars were done with 0.5-mil Kapton. Its size was enough to cover the piezoelectric wafer and had a thin strip of copper on one side. Wires were soldered to the ends of the copper-Kapton leads near the actuators, as shown in Figure 4-1, for a straight spar. A potential problem of this configuration is the damaging of the soldered wires near the actuators due to squeezing between the molds, when the spar and foam are bonded under high pressure and temperature. The bonding process is explained in detail in Section 6.2.

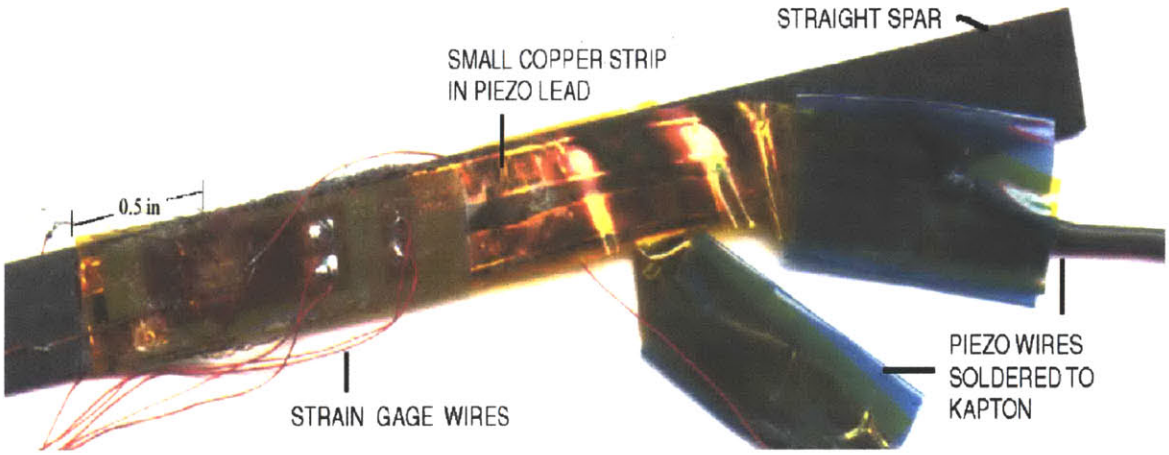

Figure 4-1: Old system of wiring followed on the straight spar.

Another problem is that this configuration proved harmful for straight spar actuation tests at high frequencies when sparks were observed to emit from the actuator while the straight spar was being actuated. The initial reason attributed to this phenomenon was that heat was produced when the piezoelectric material was actuated at high frequencies, particularly after 500 Hz. The piezoelectric material behaves as a capacitor whose impedance decreases and current increases at high frequencies, causing more heat to be produced. This

heat could not be dissipated fast enough because of the nonconductive glue surrounding the actuator. This increased the temperature of the glue to beyond its flash point. Temperature on the surface was observed to increase up to 220°F in about 2 to 3 seconds. A conductive glue such as Epotec 417 which contains macroscopic silver particles was thought to be a better solution. So, a test was conducted to verify the truthfulness of this line of thought and to gain further insight into the problem. As illustrated in Figures 4-2(a) and (b), a large sized piezoelectric wafer (about 15 mm x 30 mm) was covered with copper-Kapton glued with Epotec 301 on the left half side, and copper-Kapton glued with Epotec 417 on the other half, keeping the lower half clean.

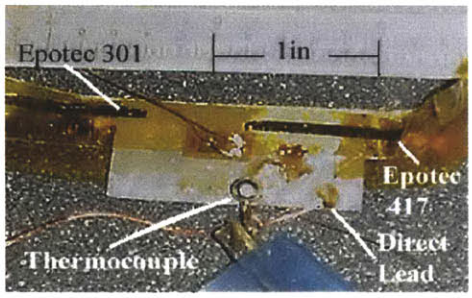

(a) Experimental specimen.

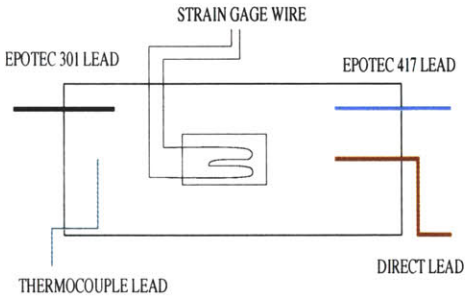

(b) Layout of specimen.

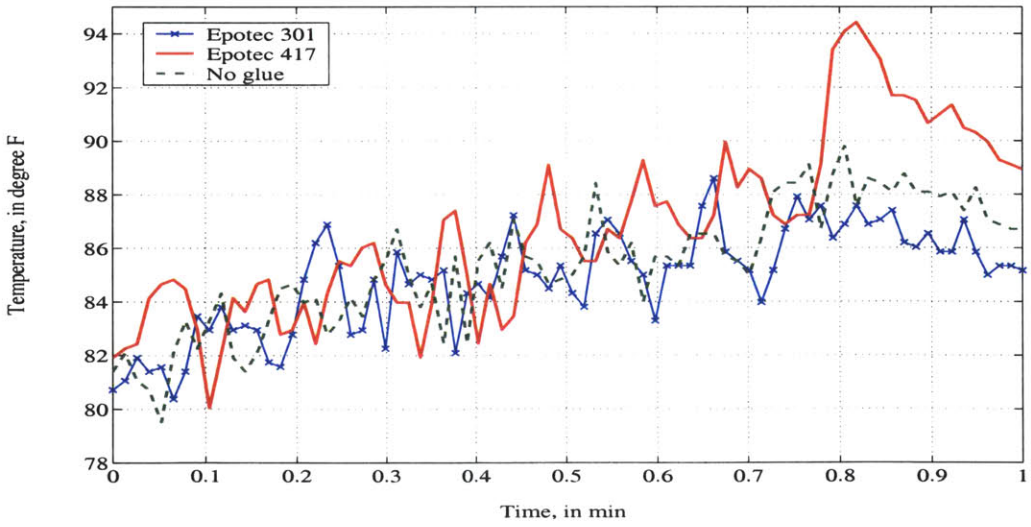

(c) Experimental results: Input signal of 220 V at 1 KHz applied during the first 30 s of the test duration.

Figure 4-2: Study of the degree of heating of the packaged actuator due to different epoxies.

Wires were soldered to the copper-Kapton leads on the free ends. A thermocouple probe, shown in Figure 4-2(a) as a large blob, was soldered to the lower half. A pair of power leads were directly soldered to the piezoelectric surface. The surface temperature was measured with: (a) the actuator being powered with the Epotec 301 Kapton only, (b) the actuator being powered with Epotec 417, and (c) the actuator being powered with direct leads. Every time, the actuation started only after the piezoelectric wafer had cooled back to room temperature. The results are plotted in Figure 4-2(c).

As seen in the graph of Figure 4-2(c), within 30 seconds of operation at 1 KHz, an increase of about 10°F was observed for basically all the three configurations. This is a small increase in temperature that does not explain the previous occurrence. Moreover, the graph does not match with the expectation that the case of Epotec 301 would show more increase in temperature than that of Epotec 417. Another possibility that may explain the observations of sparks appearing while actuating the straight spar in the original experiment was that the piezoelectric material developed microcracks while expanding. Since a narrow copper strip was in contact with a small portion of the piezoelectric wafer surface in both this experiment and the straight spar one, arcs formed between the cracks during actuation, causing the temperature to rise. This indicates the need for a wide strip of copper spreading all over the surface of the piezoelectric wafer. It was also observed that the solder joint of the wire with the copper-Kapton, which was very near the piezoelectric wafer, slipped and regained contact periodically owing to the expansion and contraction of the Kapton with the wafer. This could have been prevented by taping the wire to the copper-Kapton after soldering, a procedure which is at least inconvenient. The final reason for not using the thin Kapton is that it is very fragile to handle and to survive the blade manufacture process.

4.1.2 New Wiring Scheme

The thin copper-Kapton was replaced by the 3-mil thick copper-Kapton sheet, out of which 2 mil is copper. The thicker sheet has an added advantage that it can be directly used in commercially available printers to print the required copper lead shape. This lead shape should provide a long covering of copper-Kapton extending up to the base of the active rotor blade, and a thick twisted cable should be soldered to the free end of the copper-Kapton at the base. It was found that temperature increase in the specimen prepared using this method was within tolerable limits (about 2°F) when the aforementioned test was done.

The appropriate electrical leads shape was obtained with the help of the CAD files of the spar. The leads shape is shown in Figure 4-3(a).

Figure 4-3(b) illustrates the actuator arrangement on a spar to simulate bending while actuating the two spars independently. The actuators on both sides of the spars were oriented to have opposite polarity. This enables the independent bending of each spar, thus meeting one of the blade manufacturing objectives.

The lead diagrams were printed on copper-Kapton in a laser printer and unwanted copper was etched away with PCB Echant. The resulting surfaces were cleaned with tissue paper and cotton-tipped buds. The attachment of the piezoelectric wafer to the copper-Kapton sheets requires a very low viscosity glue so that a very thin bond layer can be formed under application of pressure. This thin bond layer will obviate the need for having a conductive bond layer for transmitting electrical fields. From [7], Epotec 301 was found to be appropriate for this purpose.

A special jig was made for packaging the piezoelectric actuators, as shown in Figures 4-4(a) and (b). Guaranteed Non-Porous Teflon (GNPT) was taped on the top of a cleaned aluminum plate having ports for vacuum pump. The copper-Kapton sheets with four piezoelectric wafers, properly aligned in between, was placed on the GNPT. This prevents sticking of Kapton to the plate. The plate was vacuum bagged and cured at 302°F (150°C) in vacuum for 2 hours in the heat press in occurrence. Vacuum causes a pressure of 15 psi on the bond layer and sucks out any air bubbles present in the glue, also known as outgassing. The resulting bond thickness was about 0.25 mil (6.35 microns). Vacuum can be avoided by putting a rubber sheet of appropriate thickness on top of the copper-Kapton sheet and compressing the system using the press. However, it is essential that no air gap remains in the glue after cure; air gaps may give rise to sparks and thus destroy the actuators when power is applied.

To test whether proper packaging of the piezoelectric actuators was accomplished, the capacitance across the leads was measured. Since the capacitance of one piezoelectric wafer is of the order of 20 nF, the total capacitance for each arm of the actuators was expected to be 40 nF because the two piezoelectric wafers in each arm were connected in parallel. A large deviation of the measured capacitance value suggests improper contact between the piezoelectric wafer and the copper-Kapton electrode.

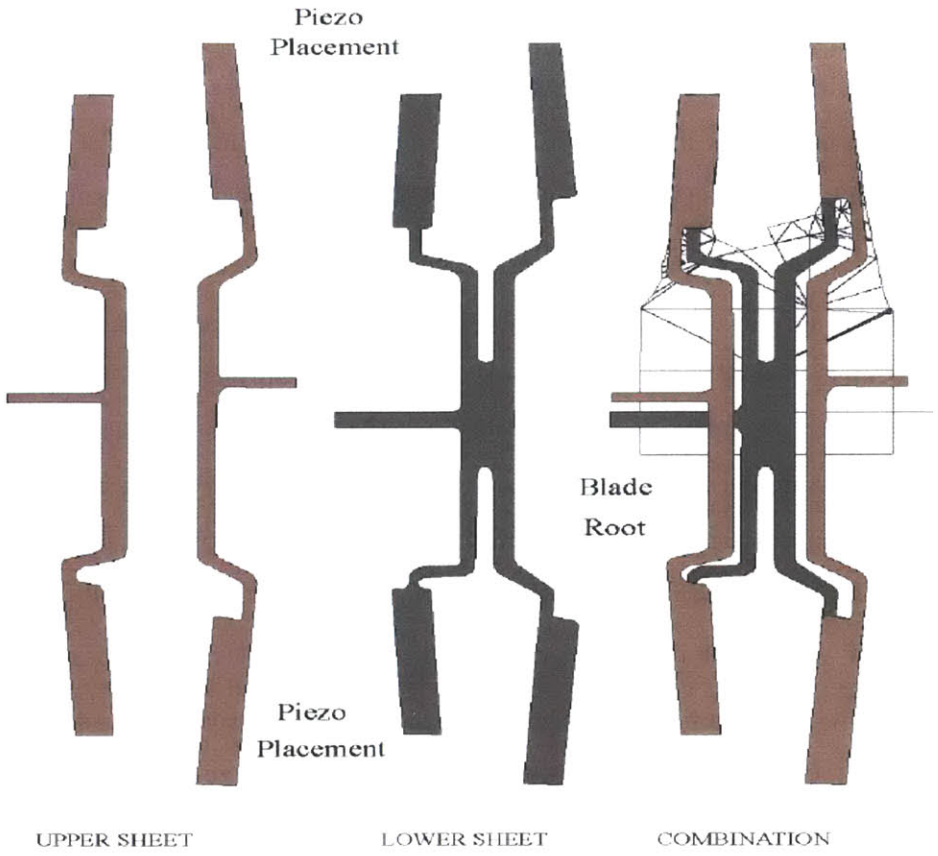

(a) Lead shape to be etched on copper-Kapton sheet

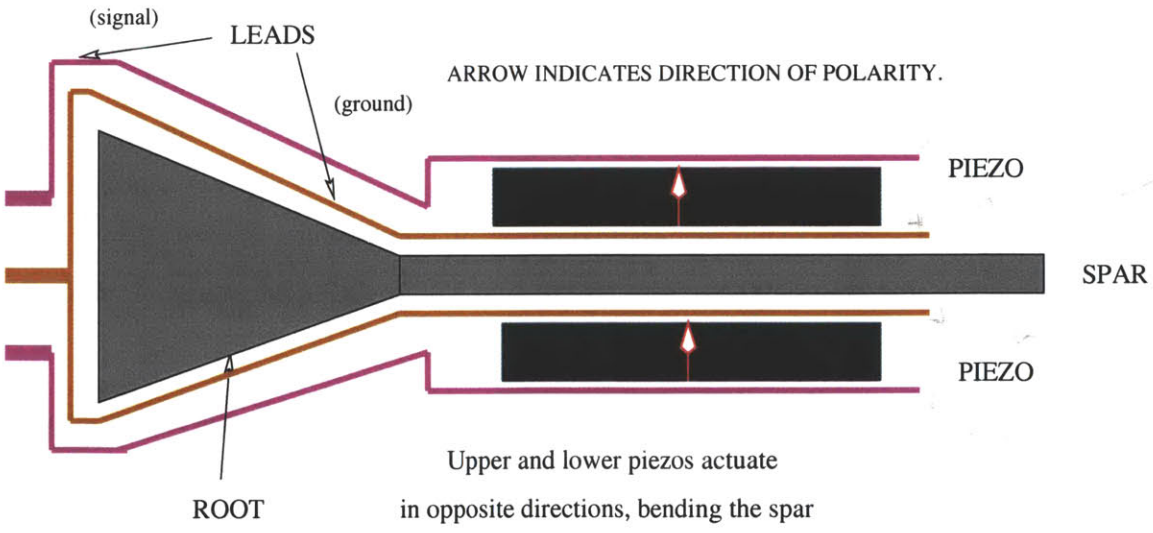

(b) Piezoelectric actuator placement on spar to simulate bending.

Figure 4-3: Development of copper leads for the piezoelectric actuator.

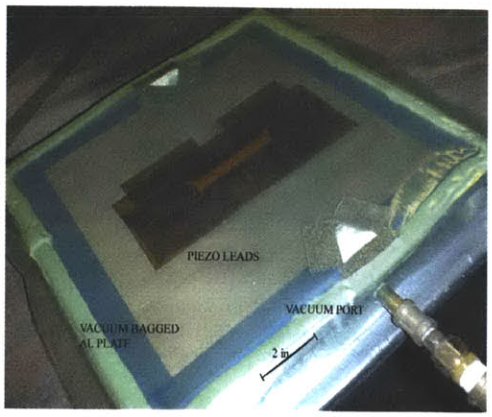

(a) Jig for preparing the copper-Kapton electrodes.

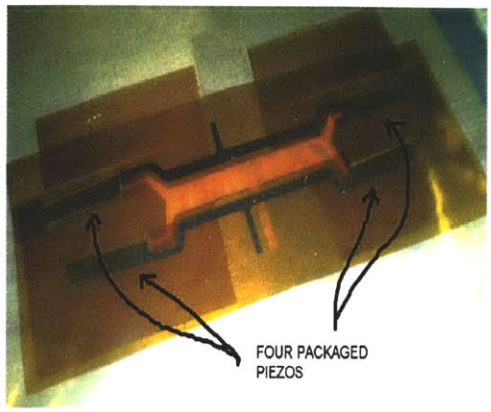

(b) Closeup view of leads and piezoelectric wafers.

Figure 4-4: Experimental setup for packaging the actuators with copper-Kapton electrodes.

4.2 Sensors used in Active Rotor Blade

As mentioned in Chapter 1, the primary sensors used in the active rotor blade are strain gages, fixed on the top surface of the piezoelectric actuators (the top surface being the one that will not be bonded to the spar). The strain gage of type EA-06-125AD-120 from Micro-Measurements Group was chosen for this project because of its appropriate size and wide availability. Figure 4-5 shows a closeup view of the strain gage.

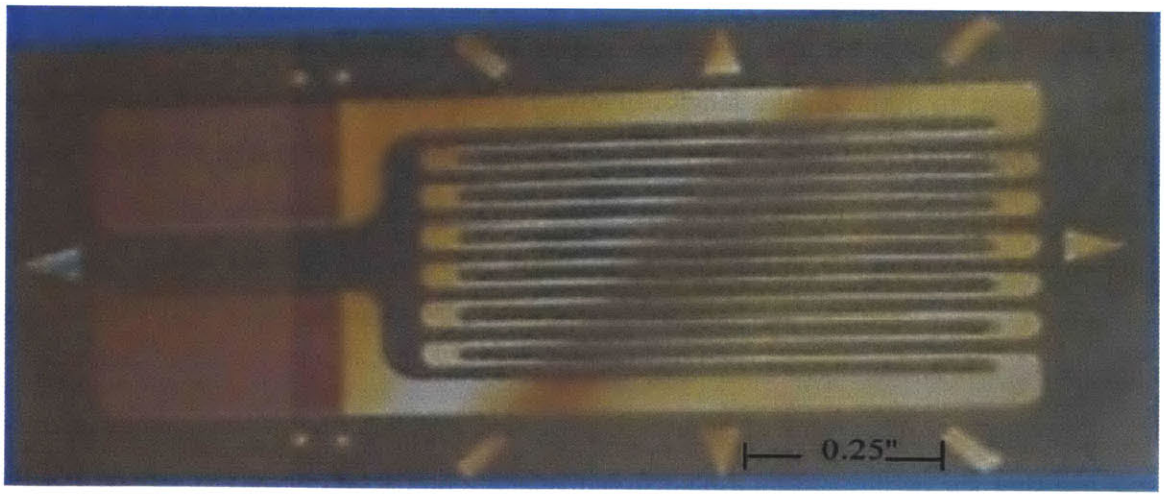

Figure 4-5: Closeup view of strain gage.

The strain gage was bonded longitudinally on the piezoelectric actuator using strain

gage glue of type M-Bond 200 and 200 catalyst of the same company. The curing procedure is as follows. The catalyst was first applied on the cleaned surface and allowed to cure at room temperature in 1 minute, then the glue was applied and strain gage attached. Thumb pressure was applied and the glue was cured in 3 minutes using the human body temperature. The final step was to solder strain gage wires to the solder points. The resistance of the strain gage was measured and compared against the manufacturer's value to verify the integrity of the gage. In the present case, the resistance value is 120 Ω.

4.3 Characterization of the Actuator

4.3.1 First Test: Butterfly Test

The piezoelectric actuators were passed through two characteristic tests before attaching to the spars. The first one was to obtain butterfly curves for one of the piezoelectric wafers in the stack bought from the company. Although the parameters involved in the butterfly curve are mentioned in the literature to be electric field and free actuation strain, this thesis deals with electric voltage and free strain. Since the thickness of the piezoelectric actuator is constant throughout the actuator, there is no qualitative difference between the two systems. The reason why voltage has been given preference over field is that the input to the system is in the form of electrical voltage and control technologies will be developed in terms of voltage.

A PZT-5A was taken from the stack and packaged, as mentioned above. Strain gages were attached to both surfaces longitudinally. The butterfly curve, as shown in Figure 4-6(b), was obtained by applying a $\pm$ 500 V amplitude triangle wave at a quasi-steady period of 30 sec (0.033 Hz) to the actuator held in free condition. The values for this type of signal have been taken from [7]. The curve was obtained by grounding one of the sides (side 2, in the figure) of the actuator and measuring strain on the other side (side 1). The notation for this experiment has been illustrated in Figure 4-6(a).

There are four points of interest in the curves. One is that in Figure 4-6(b), the maximum voltage that the actuator should be exposed is 240 V and strain of 350 $\mu\epsilon$ on the positive side and -480 V, -410 $\mu\epsilon$ on the negative side. This maximum value of voltage is known in piezoelectric terminology as repoling voltage (for a given thickness). So, in this particular case, a voltage range of 720 V peak-to-peak is available and could be used with a sinusoidal

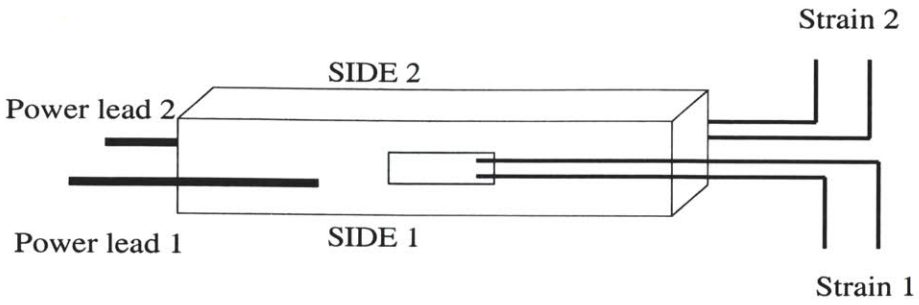

(a) Notation used

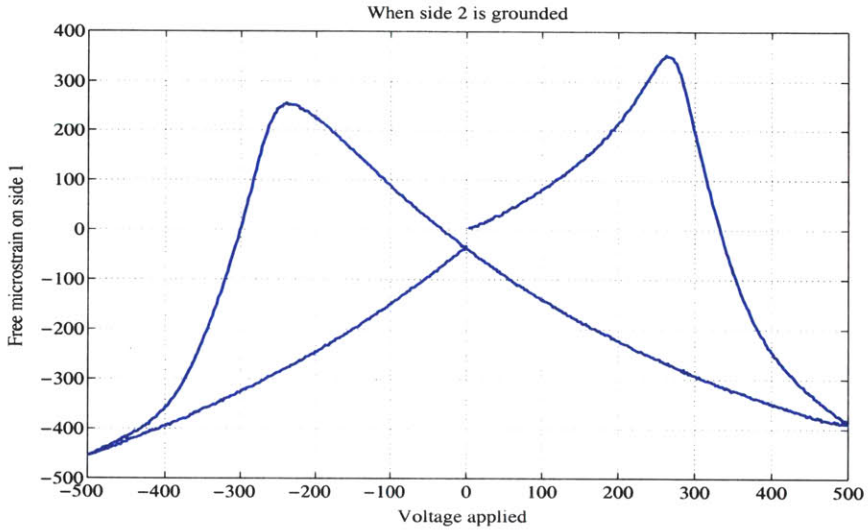

(b) Butterfly curve

Figure 4-6: Butterfly curve of free PZT-5A (size 36.3 mm x 9 mm x 0.254 mm).

excitation signal if a DC offset is superimposed to it. However, this not been exploited in this thesis. Therefore, the maximum voltage level for testing purpose has been set to be 220 V amplitude alternating signal, about 20 V less than the maximum, thus giving additional protection to the actuator.

Secondly, it can be shown that if the butterfly cycle is repeated, the enclosed area decreases with number of cycles. This is because the cycle ends at a point lower than the starting point in the strain direction, and so the actuation authority of each piezoelectric actuator decreases substantially. Also, there are sudden changes in piezoelectric behavior near the repoling voltage and so it should not be exceeded in practical applications.

Thirdly, the behavior is quite nonlinear at voltage levels near the repoling one; however, by limiting to 220 V amplitude and having no DC offset ensures linear behavior of the free actuator, less instrumentation and more reliable modeling. The downside of this method is that the maximum actuation capability of the blade is underplayed by a factor of approximately two.

Finally, the two crossed lines of the butterfly curve illustrate the behavior of the piezoelectric materials bonded to the opposite sides of the spar. One of the actuators will expand while the other contracts, thereby bending the spar.

4.3.2 Second Test: Investigation of Nonlinear Piezoelectric Behavior

As mentioned in Appendix A, the piezoelectric action has been modeled as thermal expansion and contraction, with the equivalent thermal strain determined by the product of the applied electric field and d_{31}, the piezoelectric strain constant in the 1-3 direction. It may be noted that d_{31} is a function of both applied electric field to the transducer as well as piezoelectrically induced strain. The value of d_{31} supplied by the manufacturer is normally measured at low electric field (consequently low strain response) and for a free specimen; so it cannot be used in the blade FEM for estimating the actuation limits of the active blade. Hence the following procedure was followed. This becomes the second of the characteristic tests of the transducers.

Data was collected at 1 Hz for sinusoidal cycle input voltages between 10 V and 230 V on the piezoelectric actuators prepared for the active rotor blade and is plotted in Figure 4-7. Also shown is the calculated d_{31} values plotted against peak actuation strain. d_{31} is calculated by dividing the peak-to-peak strain value by the peak-to-peak electric field value at each field. A straight line was fitted into the data points and extrapolated to zero strain to give a value, which is within 2% of the manufacturer's value of 1.71 x 10^{-10} m/V. The finite element model of the blade uses the value of d_{31} corresponding to 220 V actuation.

An interesting observation is that this curve does not match in magnitude with that given in [7] although the piezoelectric material is the same. The reason is that the two specimens belong to different factory produced batches and so have slightly different actuation characteristics. It may be noted that the piezoceramic properties vary from batch to batch due to variations in the manufacturing conditions and polycrystal formation.

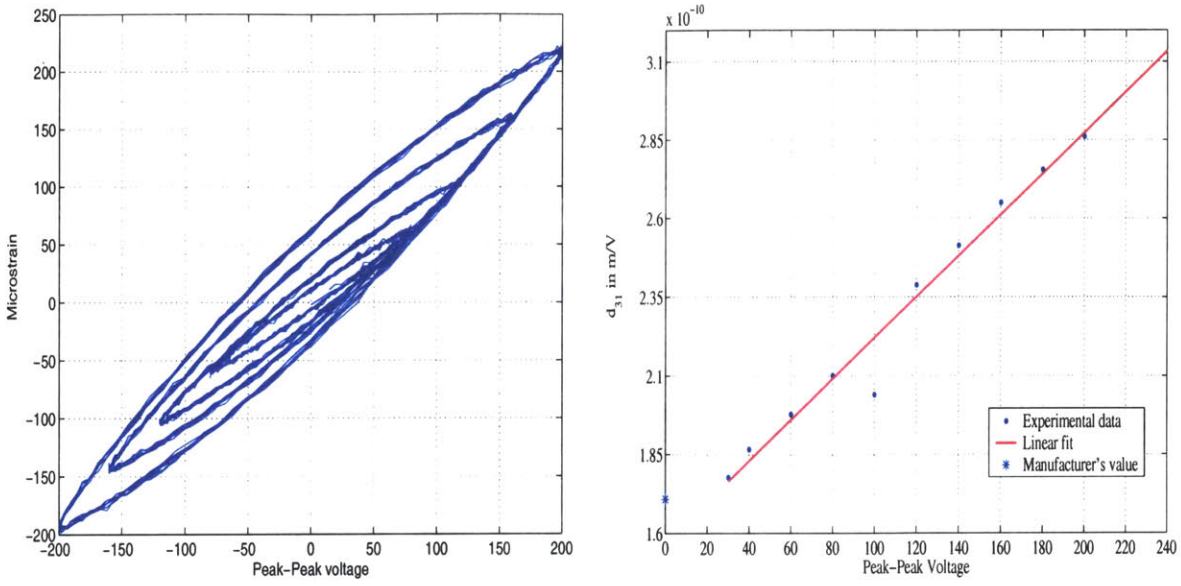

(a) Hysteresis

(b) Variation of d_{31} with actuation strain

Figure 4-7: Measuring the piezoelectric constants.

4.4 Bonding of Piezoelectric Actuators to Spar

After the characteristic tests were completed, the piezoelectric actuators were bonded to the spars. From the shear lag analysis in [7], it has been found that Epotec 301 is the appropriate glue for this purpose. Epotec 301 A and B were mixed thoroughly in the correct proportions and applied to the spar and root surfaces, and the Kapton sheets (which were cut to the right dimensions). The Kapton sheets were taped to the spars and root by means of blue flash tape (which does not glue itself to the substrate and can be peeled off after the cure). The structure was put on one of the aluminum spar molds, covered with GNPT and put on the special jig mentioned before. It was vacuum bagged and then cured inside the heat press in occurrence for 2 hours at 150°C (302°F).

The strain gage wires were removed before the cure. After the cure they were reattached to the strain gages, glued to the copper-Kapton, and brought to the root base. On the base, they were joined to a terminal strip having five nodes (four signal nodes and one ground node). To shield the strain gage wires, they were surrounded coaxially by thin aluminum foil. The foil was grounded by connecting it to the strain gage ground. Thick twisted wires were connected between the free ends of the copper-Kapton leads and another nearby terminal strip with three nodes (two signal and one ground node). Wires coming from the

outside of the blade (e.g., the actuator power source, strain gage reader, etc.) were joined to these terminal strips. Figures 4-8(a) and (b) show the final picture of the wired spar system. The reason for this wiring scheme is explained in Section 7.2.1.

(a) Top view of spars showing wiring, aluminum shield, and shims

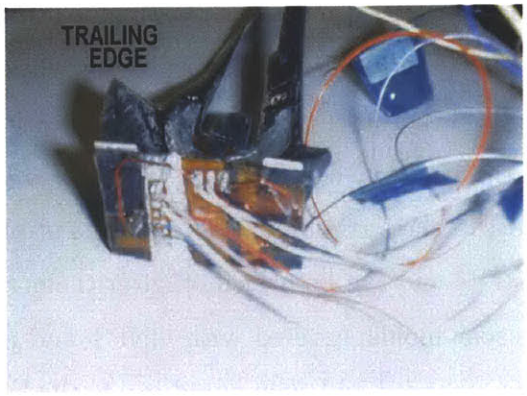

(b) Wiring on the base of the blade

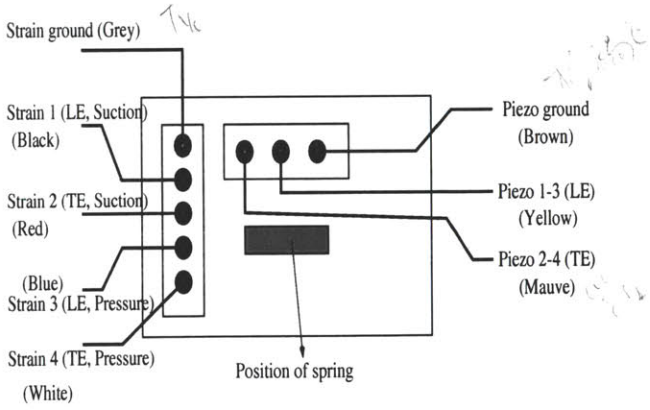

(c) Outline of the wiring on base

Figure 4-8: Wired spar system.

To prevent the wires from getting smashed on the inclined surfaces of the root when it is fixed to the hub of the rotor, aluminum shims (typical dimensions 13 mm x 10 mm x 1 mm) were fixed to the root as shown in Figure 4-8(a). Also an aluminum spring was attached to the base to make a snug fitting inside the hub. Figure 4-8(c) shows the schematics of the wiring on the base.

4.5 Problems faced with the New Shielded Wiring System

After the new wiring scheme was implemented and tested, important issues were observed. First, it was found from the benchtop experiments that three out of four of the strain gages did not give sensible readings. The possible explanation may be associated with the fact that the spar system was subjected to a temperature cycle while the actuators were bonded to the spars. This might have damaged the strain gage or drastically changed the properties of the strain gage glue. The final cause is uncertain and requires further investigation.

Another observation about the new wiring scheme is that it is not necessary to shield the strain gage wires if they are twisted. Also, the use of aluminum shield and its connection to the strain gage ground was a source of signal leakage and a decision was made to remove it.

In view of the above, new strain gages and wires were attached to the original twisted spar article so that it could be used in further tests. The new wires were twisted and taped to the spar with blue flash tape. That was performed to prevent the wires from flying apart during spar rotation. Figure 4-9 shows the new wiring system.

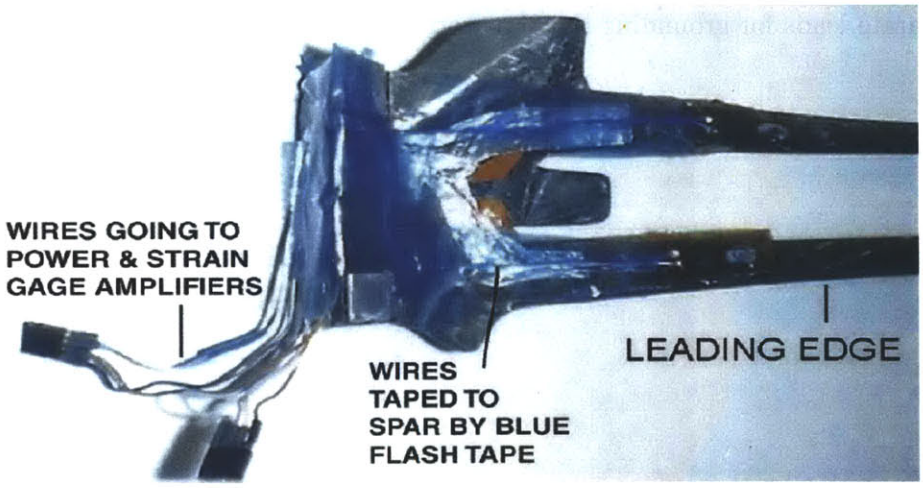

Figure 4-9: Modified wiring system used on the blade test article.

4.6 Precompression Requirement Implementation

From [7], it was found that precompression extends the life of the actuator while it is under high centrifugal loads. Also, it can be used to tailor the maximum actuation level to occur at the operating centrifugal loads. However, it has not been used in the specimen considered in this thesis. The reason is threefold. Firstly, the limitations of the uncompressed specimen can be experimentally determined in the rotating environment through its spin tests. Secondly, the copper-Kapton wiring shape used here does not allow for precompression of all the piezoelectric actuators because applying compression on one actuator puts the actuator on the opposite side of the spar in tension. Finally, conducting the actuation test at rest and under rotation will help in obtaining the required amount of precompression.

4.7 Final Remarks

The above limitations on independent activation of the four actuators on a blade indicate the need to redesign the lead shape so that all the actuators become totally independent of each other. One way of doing this would be to remove the common ground lead and make four separate leads for grounding the actuators.

Figure 4-10: Front view of the active wired spars, showing slippage of piezoelectric actuators over the spars.

Another limitation is associated with the bonding of the actuators to the curved and twisted spars. Figure 4-10 shows an example of the slippage of the packaged piezoelectric

wafers partly from the spars after their bonding. As a result, about 10% of the actuator area is not connected to this spar specimen. This reduces the actuation capability of the blade. One of the reasons for this slippage is attributed to the geometric mismatch between the spar system that was cut from the twisted plate and the actual one. It may be noted from the previous chapter that the spars were obtained by the slightly inaccurate method of taping paper with the blade outline to the plate and cutting it using a hand-held tool. Since the actuator leads were prepared by direct printing of the lead shape from the CAD files of the spars, the mismatch is due to the manufacturing error present in the spars. This motivates the use of the water-jet cutter for obtaining the spars from the graphite-epoxy plate.

The second probable reason for the slippage is that the actuator and graphite-epoxy spar have different coefficient of thermal expansions and this caused the actuators to slip while cooling took place. To avoid this, room temperature cure should be used. Curing of Epotec 301 occurs at room temperature under pressure (15 psi) within 48 hours. It is desirable to maintain vacuum for the whole period; however for practical reasons, it may be switched off after about 12 hours and the vacuum port sealed to avoid air leakage. To apply pressure to the curved top surface of the aluminum mold having the fixed spar, the other mold can be put on top and pressure applied via either the straight faced press of a hot press or by means of C-clamps. To protect the piezoelectric actuators from getting smashed between the metal molds, a thin piece of rubber can be inserted between the two molds. The advantage of rubber is that it easily conforms to the desired shape and provides a cushion to the actuators.

Chapter 5

Foam Shaping

The next step of building the blade is obtaining the required aerodynamic outer shape. This involves shaping the foam, which can be done using two ways as discussed below. Both methods need aluminum molds which can be prepared from the blade CAD files, similar to the spar molds.

5.1 Machining

5.1.1 General Procedure

The first method of shaping is machining the foam from an appropriately thick slab using the CAD files of the blade in a CNC machine. The procedure is illustrated in Figure 5-1. It is conducted in two steps. The first is to machine the top surface of the foam slab, thus shaping one side of the blade (e.g., the suction side). The next step is to invert the slab, fix it to the 'complementary' aluminum mold (i.e., the one having the suction side), and machine the new top side of the slab (to obtain the pressure side). The attachment between the slab and the mold can be done using tape and clamps. After obtaining the surfaces, the remaining side foam blocks can be chopped off to get the blade shape. The leading and trailing edges can be obtained by sanding to reasonable accuracy.

5.1.2 Problems with Machining

The low stiffness and density, and high strength properties of the foam are derived from its cellular structure. As illustrated in Figures 5-2(a) and (b), the cellular dimensions are of

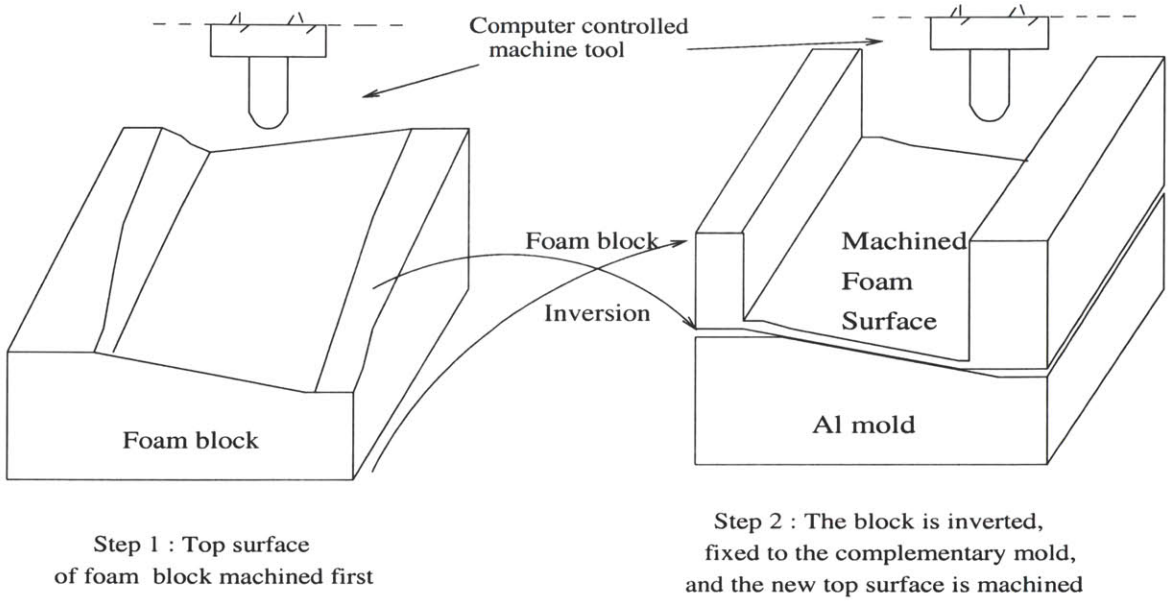

Figure 5-1: Machining procedure of the foam.

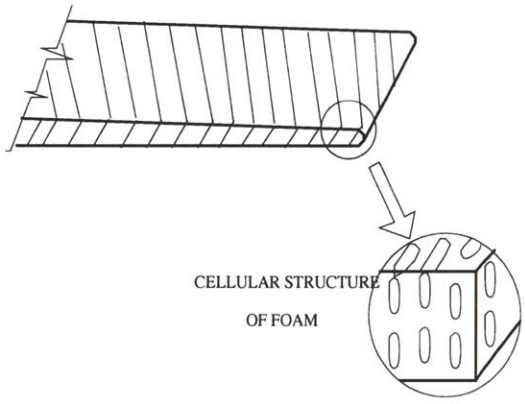

(a) Diagram of foam cells and their orientation

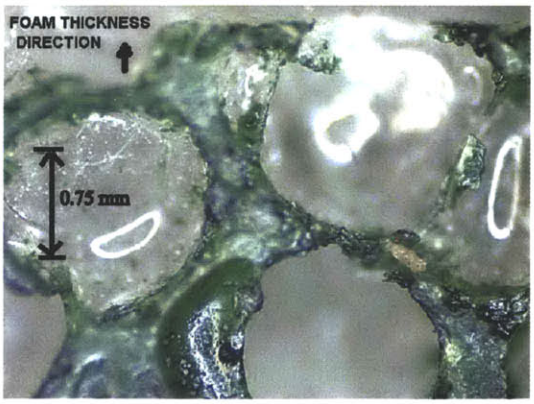

(b) Microscopic view of foam cells at tip of the blade: there are two full cells (not completely shown) along the thickness in this specimen.

Figure 5-2: Machining and the core of its problems – the cellular structure of foam.

the same order as the blade tip thickness. Machining near the tip of the blade might destroy the cells and crack the foam since the foam is too thin and fragile at that region.

Another downside of this method is that it is very expensive, and especially so if all the 26 blades of the rotor are to be prepared this way. So the alternative procedure of thermoforming may be considered now.

5.2 Thermoforming

Thermoforming is the process of heating the foam to a certain temperature, known as heat distortion temperature, and then applying pressure until the desired shape is obtained. At this temperature, the cells become soft and 'springy'. A special set of aluminum molds (mentioned above) can be used to mold the shape of a straight piece of foam into the twisted aerodynamic Fan C shape. The thermoforming procedure and the thermocycle for Rohacell WF 200 are illustrated in Figures 5-3(a) and (b), respectively. As shown in Figure 5-3(a), by putting the straight foam of approximate shape in between the molds and applying pressure by means of C clamps and heat, thermoforming can be accomplished.

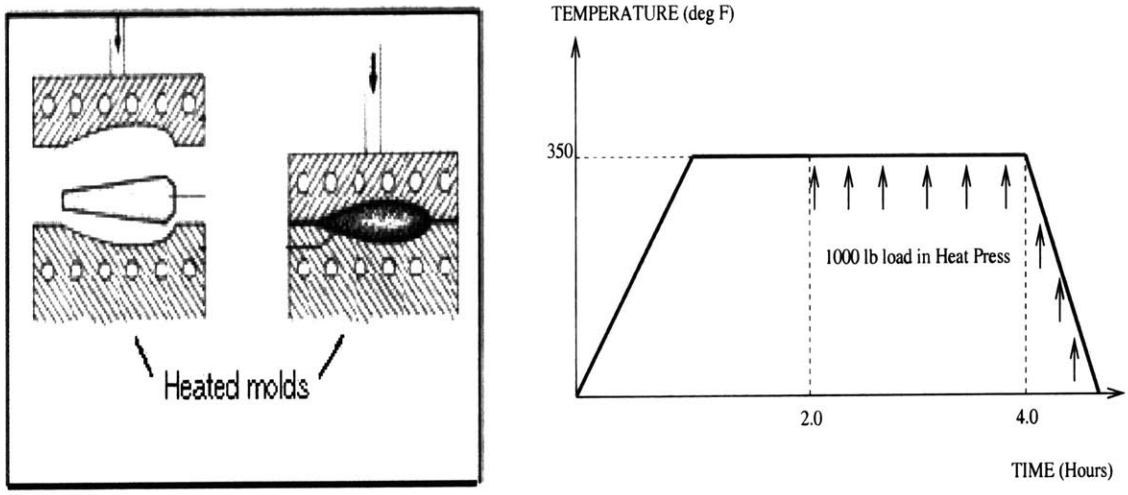

(a) Thermoforming process

(b) Thermocycle used for thermoforming Rohacell WF 200

Figure 5-3: Thermoforming procedure and cycle.

The following points may be noted about thermoforming. First, the temperature at any stage should not exceed the limit of 390°F (199°C), after which the foam cells become permanently set and cannot be thermoformed any more. The cells change from 'springy' to brittle during the process. Also, after thermoforming is over and the specimen is taken out of the mold, the foam tends to spring back. This should be taken into account while designing the molds for this procedure. This was not done since there was no previous experience with this particular blade application.

Initial tests were done with thin brick-shaped straight foams. It was found that thermoforming did not give the desired airfoil shape with tapered thickness to the cross section. This is because the thermoforming process compresses the cells of the foam in the thickness direction. To produce the thickness taper, differential pressure needs to be applied along the chord of the cross section. This could not be done using the given aluminum molds and available facilities. Hence, it was decided that the foam was to be given the proper aerodynamic shape by machining and sanding, and the required twist be given by thermoforming. Paper templates were prepared for this purpose by untwisting the foam shape, as shown in Figures 5-4 and 5-5. The foam was cut to the shape shown in Figure 5-4. Using the templates of Figure 5-5 and the sanding belt of TELAC, sanding was done to give an approximate airfoil shape and the desired thickness taper along the length.

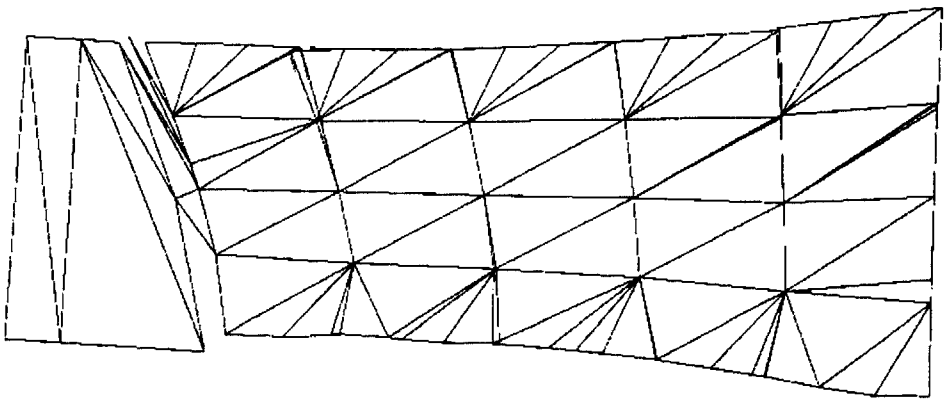

Figure 5-4: Foam shaping templates I – Plan view of foam.

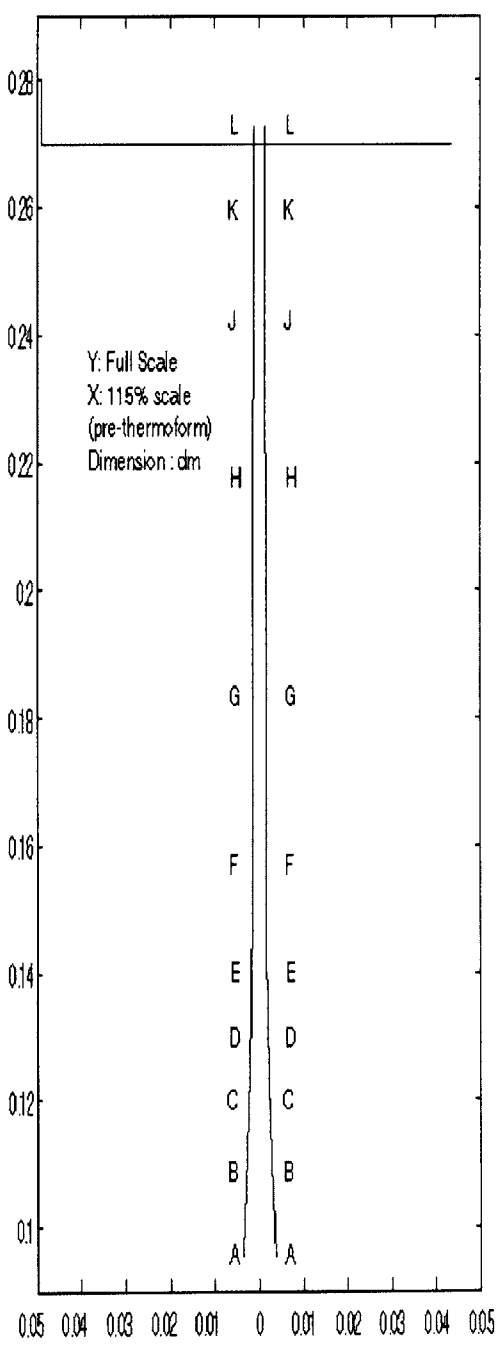

(a) Thickness profile

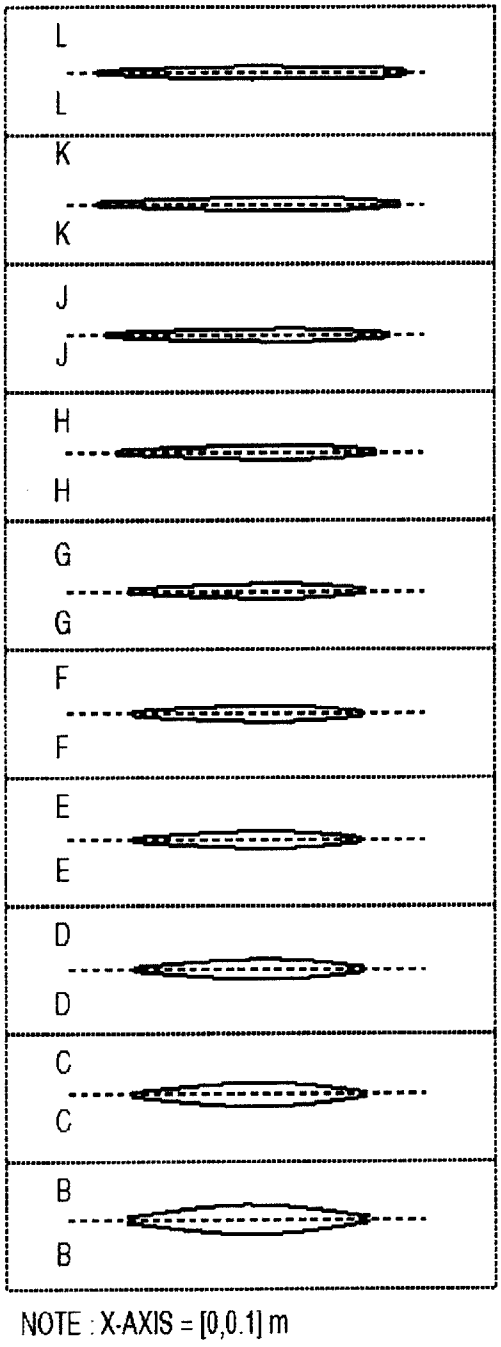

(b) Cross-section profiles

Figure 5-5: Foam shaping templates II.

Having got an approximate aerodynamic shape without the desired twist, the foam was subjected to thermoforming. The setup of a typical thermoform done in AMSL Electrical Oven is shown in Figure 5-6. The foam was taped to one of the molds with blue flash tape to prevent slipping and pressure was applied by hand through the C clamps.

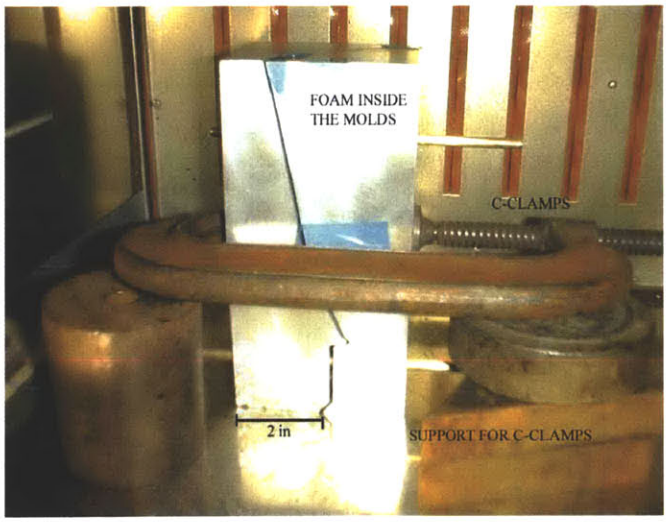

Figure 5-6: Thermoforming procedure.

It should be noted that the process of thermoforming was carried in several stages, with each stage introducing a certain amount of twist until the maximum twist level was achieved. This is because tests showed that the required twist could not be achieved in one step without breaking the foam. Moreover, as shown in Figure 5-6, the molds do not close together even in the final stage and this introduces error in the foam shape. To apply more pressure, the setup was moved to the AMSL Heat Press. When more pressure was applied onto the molds, the foam snapped at the point of maximum curvature.

To achieve more twist and to relieve some of the manufacturing stresses, grooves were made on the foam. They extended to about 1/5th of the length of the foam at the positions where the spars were to be attached later. Note that the method of attaching the spars and foam is discussed in detail in the next chapter. Although the foam seemed to thermoform in smaller number of stages, it snapped at the point where the groove initiated from base, before full twisting could be achieved. The two cases of cracking at the groove and snapping of the foam without grooves at the maximum curvature due to excess force are illustrated in Figure 5-7.

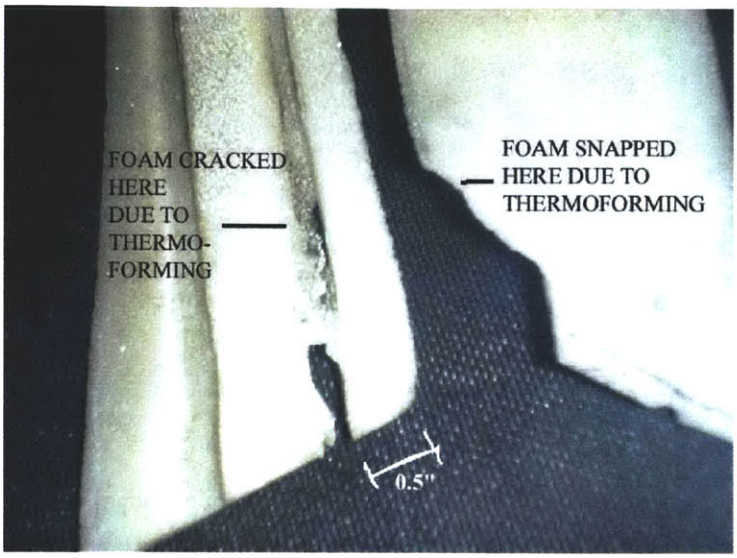

Figure 5-7: Illustration of foam cracking at groove and foam snapping at maximum curvature due to excess force and limited material flow during thermoforming.

Some of the other results achieved in this work are shown in Figure 5-8(a)-(c). As seen in Figure 5-8(a) and (b), even after 6 thermoforming cycles, the molds did not fully close. This resulted in a blade cross section that does not match the desired aerodynamic shape (Figure 5-8(c)).

Apart from breaking, the second potential problem of thermoforming was the apparent stiffening of foam during each thermoforming cycle. More on this will be discussed in the next chapter. Another problem faced was that it did not produce the desired shape at the leading and trailing edges.

5.3 Final Remarks

The uncovered problems associated with thermoforming turned out to be significant, and machining seems attractive once more. However, no machining attempt was done to verify its applicability and is left for future work.

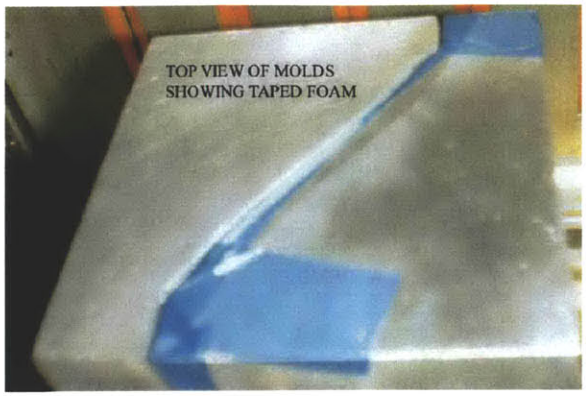

(a) Top view of the molds, after thermoforming

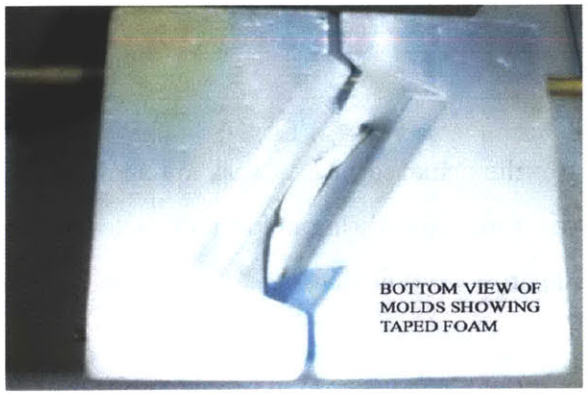

(b) Bottom view of the molds, after thermoforming

(c) Best result in thermoforming achieved after 6 cycles

Figure 5-8: Illustration of the thermoforming process and its effectiveness.

Chapter 6

Assembly of Blade

This chapter deals with the process of assembling the blade from its components. The attempt made to get the first active rotor blade and its integrity test is discussed. The chapter then discusses an experiment to quantify the effects of subjecting the blade to thermal cycles, the reason being that the blade is subjected to several thermal cycles during its preparation. Based on these observations, an improved method of attaching the spars and foam is suggested at the end.

6.1 Assembling of Blade

The blade can be assembled by the following steps.

- Making grooves on the foam surface
- Attaching the spars to the grooves to get a smooth aerodynamic surface
- Preparing the leading and trailing edges, if necessary, to get the desired sharp edges.

The unanswered questions that arise from this outline are the method of making grooves on the foam and the identity of the glue that can hold the spars and foam together at operating conditions. Grooves can be done either by CNC machining or by hand-held tools. The former can make use of the CAD files prepared for the active rotor blade. In the case of the latter, the spar path may be created on the foam by a process similar to that of obtaining the spar path on the graphite plate. However, since that is not accurate, the option of machining together with sanding the grooves is preferable. It should be noted

that the groove width and depth should be just enough for the spars to fit into them snugly after pressure is applied. Also the depth of the groove should account for the increase in thickness of the spars at the base due to the piezoelectric actuators and the attached wiring. This will ensure a smooth aerodynamic surface of the blade.

The second question about finding the proper glue for the bond is a difficult one since the interface between the spar and foam is so complicated that standard glue strength analysis such as shear lag is not useful for this purpose. So, direct experimentation should be used to find the right glue. Epotec 301, which was used for attaching the actuator to the spar, can be taken as the first choice. This glue was used in the manufacturing process of the first active blade.

The method of preparing the leading and trailing edges has been discussed in the next section.

6.2 Manufacture of the First Twisted Blade

The preparation of the first twisted blade illustrates the do's and don'ts of the manufacturing process of the active blade. The spars cut from the graphite-epoxy plate were not radially placed with respect to the rotor hub, but were cut along two parallel planes. The reason for doing so was that the CAD files for getting the correct spar paths had not been completed at that time. The foam was shaped by hand and thermoformed in several stages to get the maximum twist possible. The spar path on the foam was obtained by printing the spar path on paper and cutting it, and then folding and taping it on to the foam. Grooves were made by hand using Dremmel tool. The width of the grooves was attempted slightly smaller (about 5%) than that of the spar. To even out the floor of the grooves throughout the length, sanding was done. However, it was not possible to control the depth of the grooves and in some places it was about 7% smaller than that of the spar at that point while at other places, it was larger. The spars were attached to the suction side of the foam because preparing grooves on the suction side was found to be easier.

The result after this procedure is shown in Figure 6-1. It shows some of the places of geometric mismatch between the spars and the foam. This can be attributed to: imperfect thermoforming, groove manufacture and spar cutting, and unequal coefficient of thermal expansion of spar and foam. Although this blade was not expected to survive 16000 rpm,

it underwent the complete manufacturing stage to gain insights into the process.

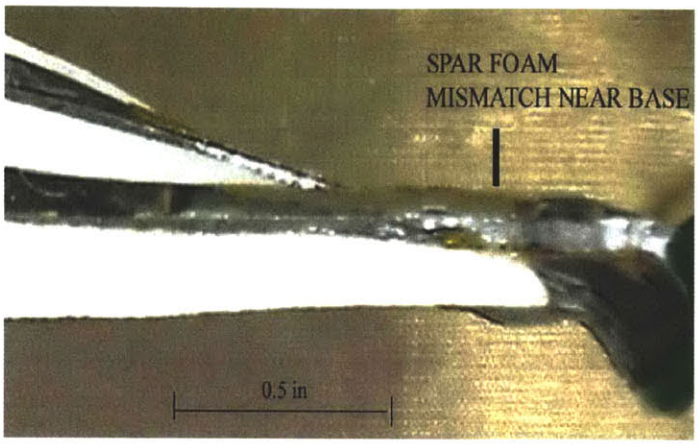

Figure 6-1: Closeup view of the first active rotor blade – Mismatch between the spar and foam at the base can be seen.

The next stage was to get the leading and trailing edges of the foam accurate. They were prepared by having S-glass epoxy fibers attached to the edges on both sides of the blade, covering about 1/5th of the blade width on each side. The fiber made an angle of 90° with the length of the blade. The reason for choosing glass over graphite is that it has lower stiffness than graphite. The 90° angle was for the purpose of not drastically changing the torsional and bending stiffness of the blade. Before adding the fibers, the foam edges were painted with Epotec 301. To avoid the fibers to be supported by the foam alone and, therefore, adding excess stress on the foam, the fiber-glass strips were made to extend up to the transition element of the blade.

After putting the fiber-glass strips on the foam, the grooves and spars were painted with Epotec 301 and the spars attached to the foam at the grooves by taping them with flash tape. The assembly was put in between the foam molds, and then cured using the same cycle as graphite-epoxy, except that the lower temperature level was 250 °F (121 °C), the curing temperature of glass-epoxy, while the higher temperature was kept the same, 350 °F (177 °C), the thermoforming temperature of foam. The rationale was that thermoforming softens the foam and allows the spars to push into the grooves so that on cooling, the spars stick to the foam tightly.

Although the blade was not wired, aluminum shims were attached to the root of the blade to simulate the contact conditions faced by the wired active rotor blade. More on

this was discussed in Section 4.4.

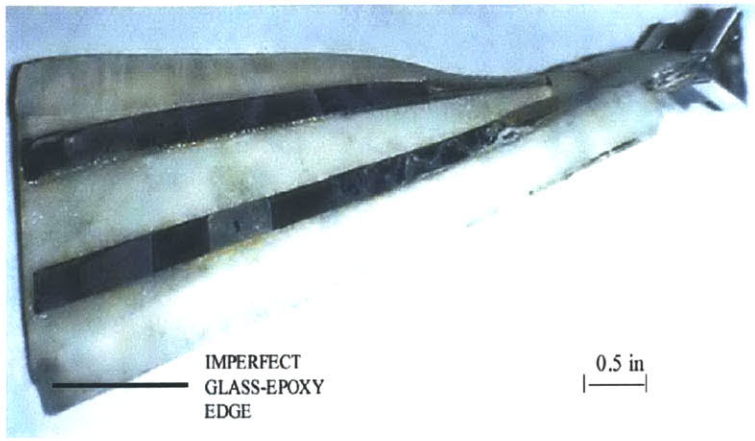

Figure 6-2: Final stage of the first active rotor blade – glass-epoxy LE and TE can be seen.

The result is shown in Figure 6-2. Clearly, the bonding of the glass fibers at the tip of the blade does not look satisfactory. The bonding was better at the base of the foam, where the fibers were also in bondage with the graphite tab.

A spin test of the blade was conducted in vacuum in a specially designed spin pit (Chapter 7). It was observed that the foam broke at 6500 rpm. The remainder of the blade is shown in Figure 6-3. As one can see, most of the foam got separated from the spars and smashed against the vacuum chamber into pieces.

Figure 6-3: Damaged blade test article after being spun at 6500 rpm.

Clearly, Figure 6-3 shows that some of the foam remained attached to the spars at places (in this sample, the base region) where the bonding with the spars were without flaws. This indicates that the glue was performing well thus far and that the quality of the finishing

is essential for the integrity of the test article. As said above, one reason for the imperfect spar-foam bonding was the imperfect foam shape and grooves manufactured by hand. This suggests the use of CNC machining to prepare the foam of correct shape along with the grooves. The mismatch of the coefficient of thermal expansion between graphite and foam may have also played a significant role in the misalignment, suggesting the avoidance of elevated temperature cure at any stage of the bonding process. If glass fibers are to be introduced at the edges of the active rotor blade, then they can be added after the room temperature bonding of foam and spars is completed.

6.3 Effects of Thermocycling on Blade Actuation Capability

So far, the effects of thermocycling on the blade have been seen qualitatively. To quantify the effects, a benchtop actuation test was performed on a straight untwisted but tapered blade. The straight blade was chosen for simplifying the experimental procedure while capturing all the essential features to be studied. The dimensions of the straight blade is comparable to that of the active rotor blade.

The specimen was prepared as follows. Piezoelectric actuators were packed and bonded to the spars. Strain gages were attached and wires were soldered to the ends of the copper-Kapton leads and to the strain gages. Thermal cure method was followed for the bonding process, and it was found that only one of the actuators showed the correct capacitance after the wiring was completed. The reason may be attributed to damaging of the copper-Kapton leads of the other actuators, or the contact between the leads and the actuators during the bonding procedure. However, one working actuator was sufficient for this study, thus enabling the specimen to be used for the experiment. A straight tapered piece of foam was then attached to the spars at room temperature. The blade was clamped at the root end and the working actuator was applied a sinusoidal signal from a signal generator and amplified through an audio amplifier (more about this will be discussed in the next chapter). The following are the particulars of the signal:

- Maximum signal amplitude from the signal generator of 300 mV
- Signal frequency band from 50 to 1250 Hz
- Linear frequency sweep with 4-second duration

- Variable voltage gain across the audio amplifier (see Figure 7-5 for more details).

The strain gage readings were recorded and transfer functions between the strain gage and signal generator readings plotted. The same transfer function plots were made after the blade underwent one thermoform cycle and then another. A picture of the blade setup is shown in figure 6-4 and the result shown in figure 6-5.

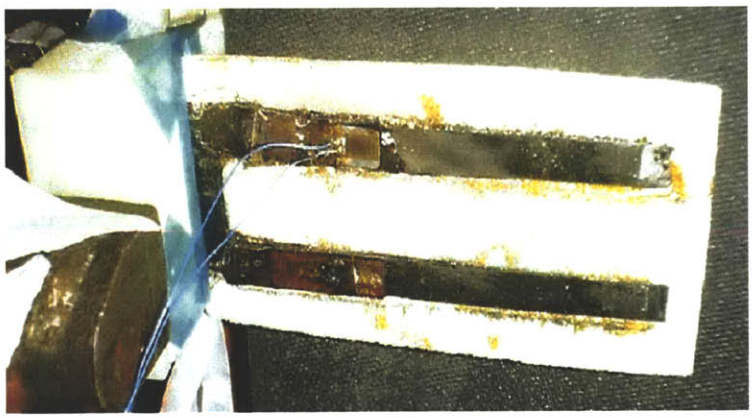

(a) Straight blade showing foam, spars and strain gage wires come out of the working actuator

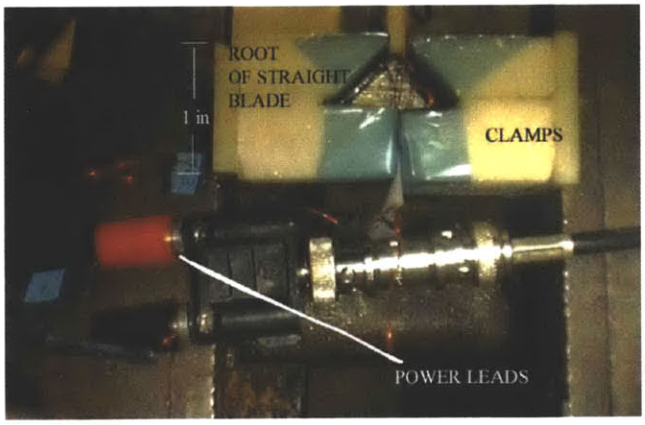

(b) Clamped boundary condition

Figure 6-4: Blade setup for determining the effects of thermocycling on blade actuation performance.

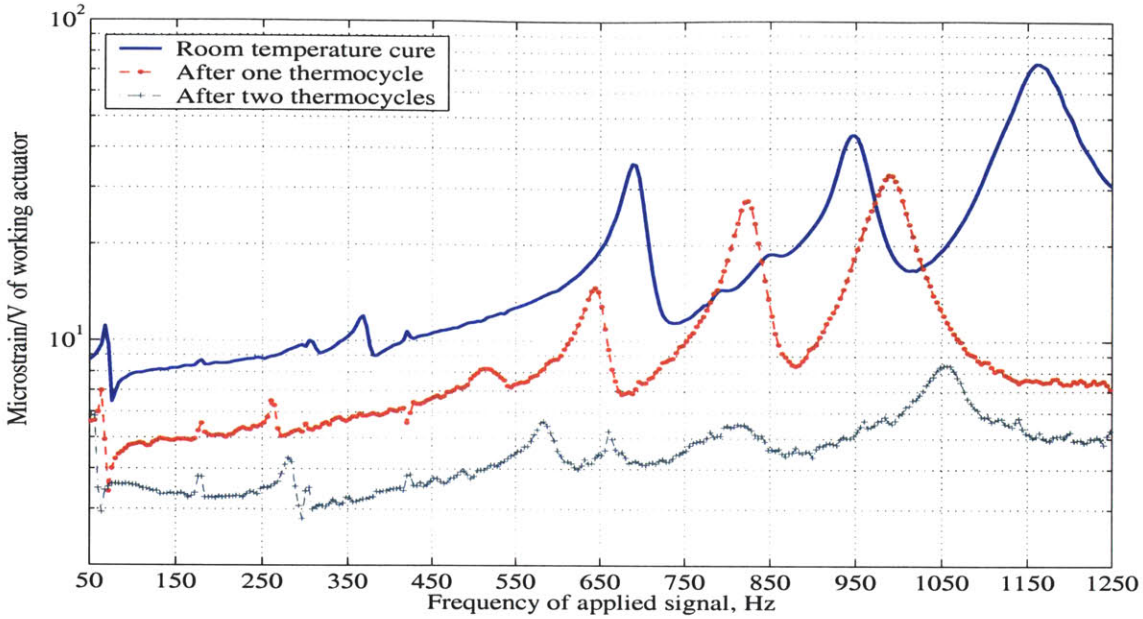

Figure 6-5: Effects of thermoforming on blade – transfer function result at 300 mVpp.

The results are very clear: the strain in the actuator decreases by as much as 50% after each thermocycle. The following points may also be noted about this experiment.

- The 300 mV ensures that the piezoelectric actuator is in its linear range throughout the actuation level and this helps to decode the results easily.

- The explanation of the reduction in actuation level given is that the stiffness of the foam increases with each thermocycle. This was also felt by twisting the foam by hand after each thermoform stage.

- From this experiment, it can be safely assumed that there will be a decrease in strain actuation in case of the twisted blade.

- The transfer function exhibits a 20-dB slope increasing tendency with frequency. This corresponds to a capacitative effect due to the interaction between the strain gage, its glue, and the underlying copper-Kapton lead. This will be further explained in the next chapter. Despite of this, the above observations still hold.

6.4 Final Remarks

The observations made so far regarding thermal cycling seem to reinforce the conclusion that curing at elevated temperatures should be prevented at any stage of blade preparation, except during the manufacturing of the graphite-epoxy twisted plate.

The appropriate curing procedure for attaching spars and foam is then similar to that used in the bonding of the actuators to the spar. Epotec 301 is applied to the cleaned surfaces of spars and foam grooves, the spars put inside the grooves, and the blade put inside the foam molds. The molds are then vacuum-bagged and cured under a load between 2000 and 3000 lb. The load may be increased from zero until the molds close together. The cure takes about 48 hours to complete at room temperature.

Chapter 7

Performance Testing of Spars

Before attaching the spars and foam, the active wired spar system was tested to get its performance at rest condition as well as while spinning. The plan followed to achieve this objective was as follows:

- Actuation testing on benchtop to verify the proper working of the spar system and also to characterize its nonrotating performance.
- Spinning of the spar and testing for its performance at various rpms.

Here the term 'performance' refers to the tip displacement of the spars and the strains in the actuators at various frequencies of the applied signal. Also it may be noted that the spin tests were conducted in vacuum to eliminate the effects of aerodynamic loads. Inclusion of aerodynamic loads is left for future work.

The description of the various tests has been divided into three sections – instrumentation, procedure and results.

7.1 Benchtop Tests

7.1.1 Instrumentation and Experimental Layout

The following instruments were used to conduct the tests.

Computer/DAQ

A PC loaded with National Instruments LabView 4.0 software and data acquisition (DAQ) board PCI-MIO-16E-4, was used to collect data from a variety of instruments. The DAQ

board has 16 single ended input channels, two output channels, and can sample up to 250 KHz data. More information on the software and DAQ board specifications is available in [12].

Actuator Power Supply

The power supply to the actuators consists of: (a) HP 33120A 15 MHz function/arbitrary waveform generator, which can generate signals up to 10 V amplitude; (b) Yorkville AP4040 audio power amplifier which amplifies the voltage signal from the generator up to 25 times in the presence of the actuators. This has a two channel output, with the option of having the channels independent of or dependent upon each other. Thus, one audio amplifier rack can serve to power one active rotor blade; (c) Transformer of coil ratio 22 x 115, which, together with the amplifier, amplifies the signal generator voltage by 120 times; and (d) DC offset instrument, which can provide a DC offset of up to 100 V. This, however, has not been used in this study for reasons mentioned in Section 4.3.1. The high voltage readings were recorded in the computer after passing the signal through a 100 x 1 voltage divider.

Strain Gage Amplifier

The strain gage signals were passed through a breakout box mentioned in [7] and fed to strain gage amplifiers of the 2310 Measurement Group, Inc. series. Each strain gage was fed into a single channel of the amplifier rack. The amplifier works on the Wheatstone bridge principle as illustrated in Figure 7-1(a) and has a 10 KHz filter built into it to remove any high frequency noise from the signal.

One important issue related with instrumentation that must be pointed out here is the strain gage capacitative effect. This phenomenon is influenced both by the action of the strain gage amplifier and the wiring of the strain gage and the actuator. As illustrated in Figure 7-1(b), the top copper-Kapton sheet, which is the signal lead, carries $V_S \sim 120$ V of electrical signal (the reason for this signal given in Section 7.1.2), the bottom one is grounded and the strain gage wires which carry signals of the order of millivolts are practically grounded. The top copper-Kapton lead and the strain gage form a capacitance plate with Epotec as the dielectric, as seen by the strain gage amplifier. This capacitance overwhelms the 120 Ω resistance of the strain gage at around 1 KHz frequencies, especially with the 2 V excitation voltage (V_E) applied by the amplifier to measure the strain gage

resistance change due to strain. Hence an increasing trend (of slope 20 dB) was observed in the strain gage transfer function plots, as presented in Section 6.3. To eliminate this effect, the top copper-Kapton sheet may be grounded so that the voltage difference between the top sheet and strain gage is of the order of millivolts. Note that V_E cannot be increased to offset this effect without damaging the strain gages.

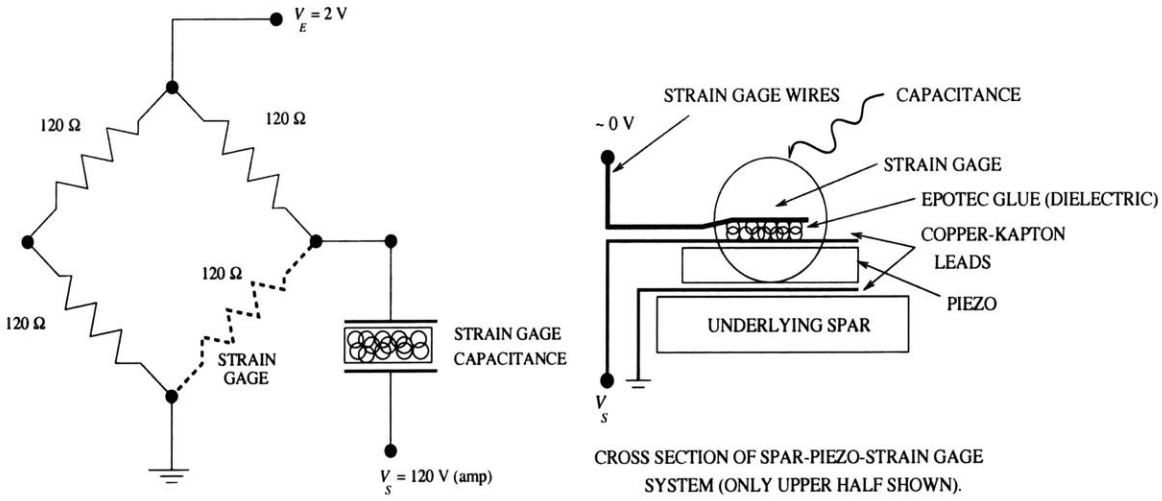

(a) Wheatstone bridge action of strain gage amplifier and parasitic capacitance effect

(b) Strain gage capacitance structure

Figure 7-1: Strain gage capacitance effect due to grounding of the bottom copper-Kapton sheet.

Laser Sensor

The Keyence LB-72 laser sensor was used to capture the tip displacement readings of the spar while it was actuated. The settings and calibration procedure are given in [7]. It may be noted that the bandwidth of the sensor is about 600 Hz.

Signal Analyzer

A HP 35665A dynamic signal analyzer was used to compute the transfer function of the laser or strain gage reading to the signal generator, *in situ*. Because it has two channels, the transfer functions can be generated sequentially. The drawback is that it takes a longer time to get all the transfer function readings, when compared to an analyzer with more than two channels. The actuation test time is critical in the spin tests at high rpms (greater than

6000 rpm) in which case the temperature of the spin stand vital components rise sharply, limiting the test time. More on the spin stand is discussed in Section 7.2.1.

The above instruments were laid out according to Figure 7-2 and the spar system was clamped at the root, as shown in Figure 7-3.

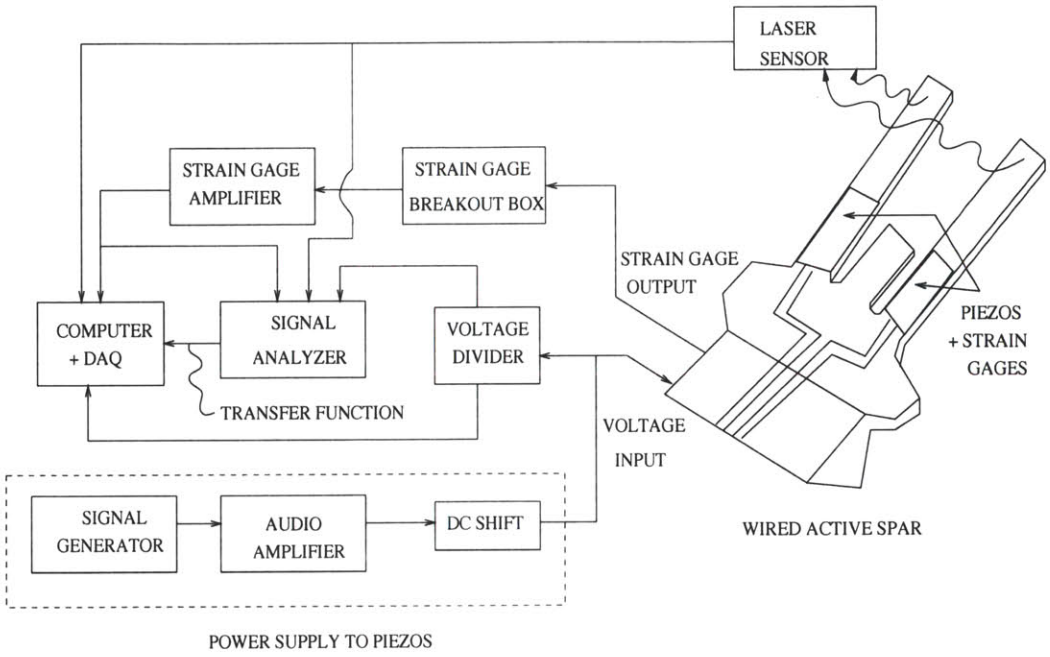

Figure 7-2: Spar actuation test on benchtop – instrument layout.

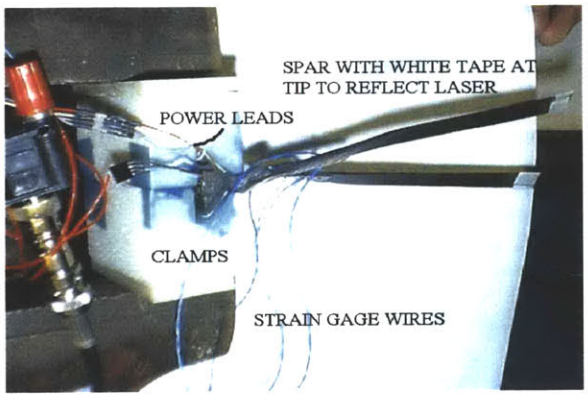

Figure 7-3: Assembly conditions during benchtop test of active wired spar.

7.1.2 Test Procedure

To avoid the parasitic capacitance effect on the strain gage readings, the top copper-Kapton sheet of the spar was grounded while the bottom was made the signal lead. The aftermath of this was that the spars could not be actuated out of phase directly but could either be individually actuated or actuated in phase. The reason is that the two piezoelectric actuators on each blade surface are poled in the same direction, and so out-of-phase actuation is not possible with the same signal lead to both of them. This was illustrated in Figure 4-3.

To get strain and tip displacement to voltage transfer functions for all cases of actuation, the following plan was used.

Notation:

Excitation of leading edge (LE) actuators	A
Excitation of trailing edge (TE) actuators	B
Excitation of both, in phase	C
Excitation of both, out of phase	D
Strain gage at LE, suction side	S1
Strain gage at TE, suction side	S2
Strain gage at LE, pressure side	S3
Strain gage at TE, pressure side	S4

The actuating spar is indicated in the strain gage reading by a subscript. So the notation $S1_B$ indicates suction-side LE strain gage reading when TE spar is actuated in bending. The notation for the laser sensor is slightly different in that two subscripts are used. For example, L_{BA} indicates laser displacement reading of LE spar tip when TE spar is actuated.

Experiments Conducted:

Experiment done	Variables measured
A	$S1_A$, $S3_A$, L_{AA}
B	$S2_B$, $S4_B$, L_{BB}
C	$S1_C$, $S2_C$, $S3_C$, $S4_C$, L_{CA}, L_{CB}

Results Derived:

The remaining readings were obtained as follows:

$$S1_B = S1_C - S1_A \quad S1_D = S1_A - S1_B$$
$$S2_A = S2_C - S2_B \quad S2_D = S2_A - S2_B$$
$$S3_B = S3_C - S3_A \quad S3_D = S3_A - S3_B$$
$$S4_A = S4_C - S4_B \quad S4_D = S4_A - S4_B$$

and so on for the laser readings.

A swept sine signal shown in Figure 7-4 was applied to the actuators according to the above plan. The transfer function of the overall power system's output with respect to the signal generator output is shown in Figure 7-5. The particulars of the power signal are:

- Signal amplitude of 1 V from the signal generator
- Signal frequency band between 50 and 1250 Hz
- Linear frequency sweep with 4 seconds duration
- Variable power system overall voltage gain as shown in Figure 7-5.

It may be noted that 1 V signal from signal generator is adequate for calculating the transfer function readings.

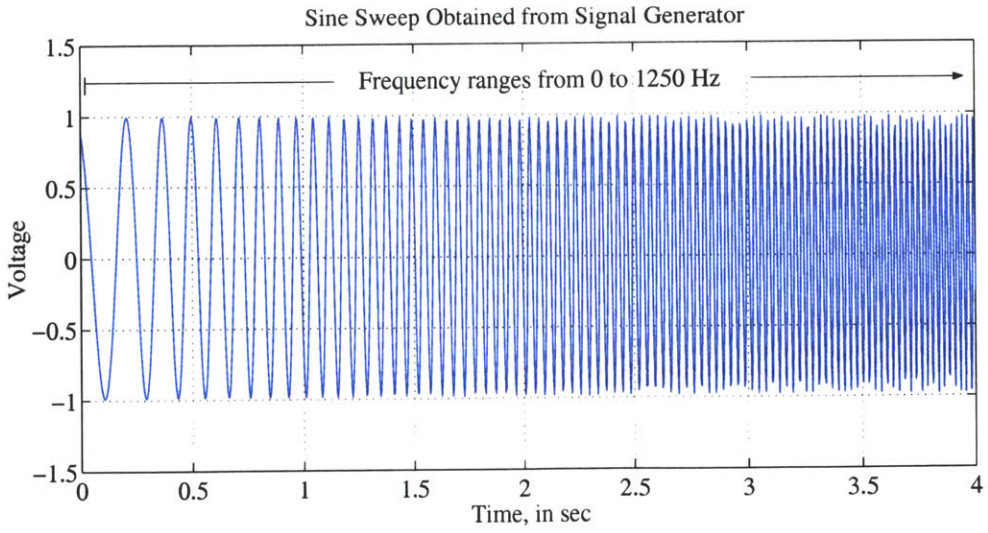

Figure 7-4: Swept sine signal from generator – input signal to power amplifier system.

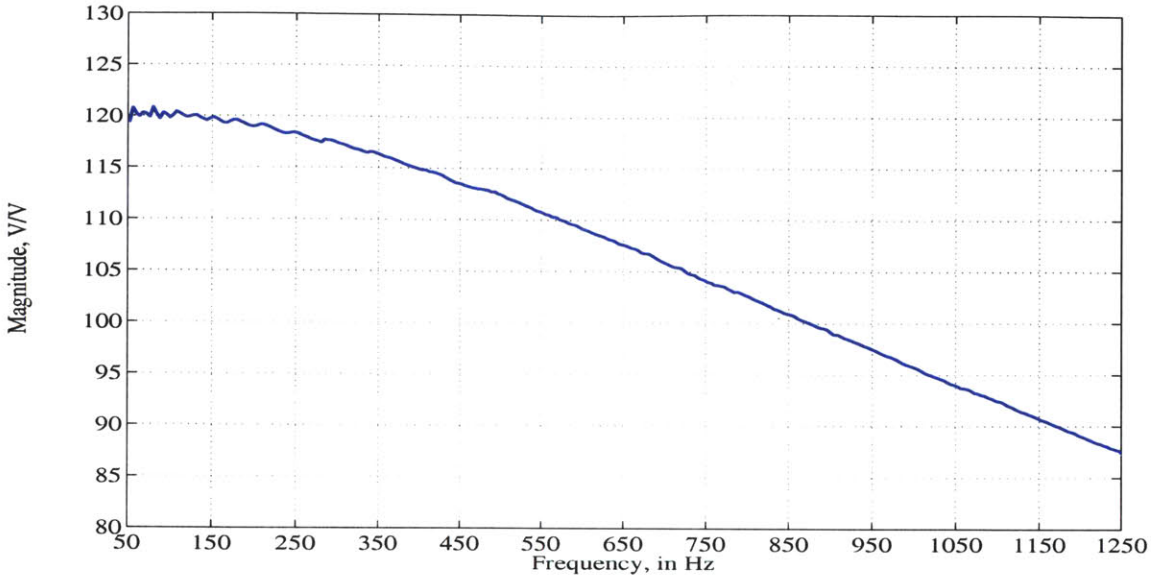

Figure 7-5: Transfer function of the audio amplifier output with respect to the signal generator output.

7.1.3 Results

The first set of results are presented as frequency responses of tip displacement due to applied voltage on the actuators. The frequency response is calculated by dividing the transfer function of the desired variable with respect to the signal generator voltage, by the transfer function of the power system signal output to the actuators with respect to the signal generator voltage, and multiplying the resultant by 220 V. This gives the frequency response when the applied voltage to the actuators is 220 V amplitude for all frequencies. This is useful in obtaining the performance limitations on the blade. Figures 7-6(a) and (b) show the laser displacement results for both tip twist and tip bending deflection. The tip twist was calculated by dividing the sum of the two spar tip readings by the interspar distance at the tip. The tip bending deflection is the average of the two spar tip readings. The upper limit of frequency shown in the figures is because of the 600 Hz bandwidth of the laser sensor.

The following are the noteworthy points regarding the spar performance:

- The active spar system closely meets the pitch and plunge (or bend and twist, respec-

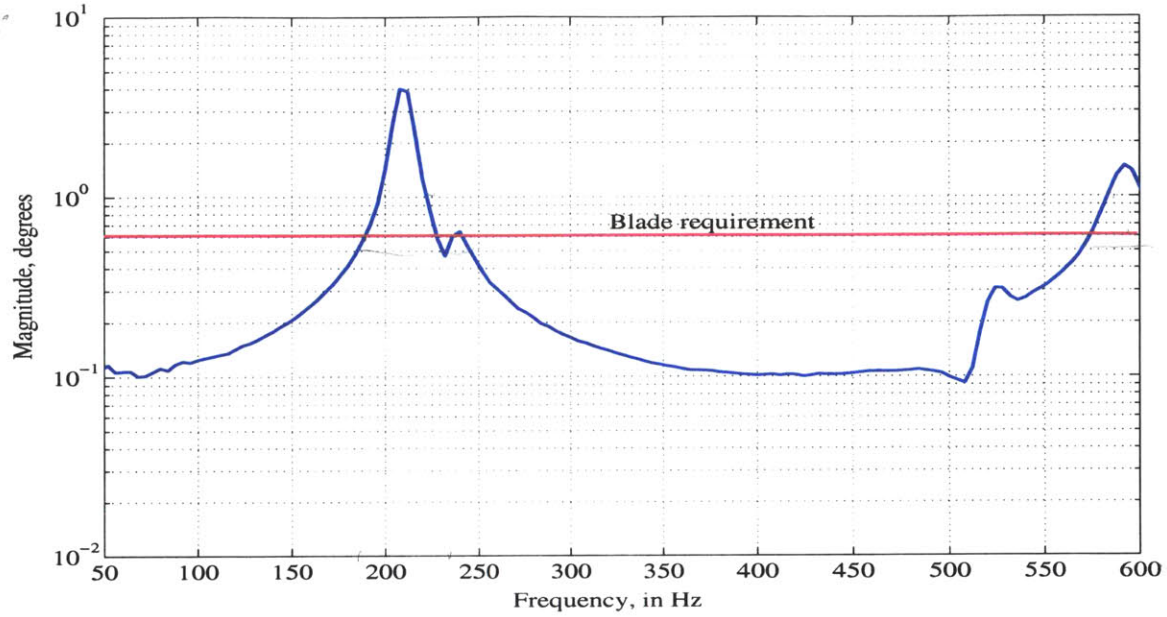

(a) Tip twist frequency response.

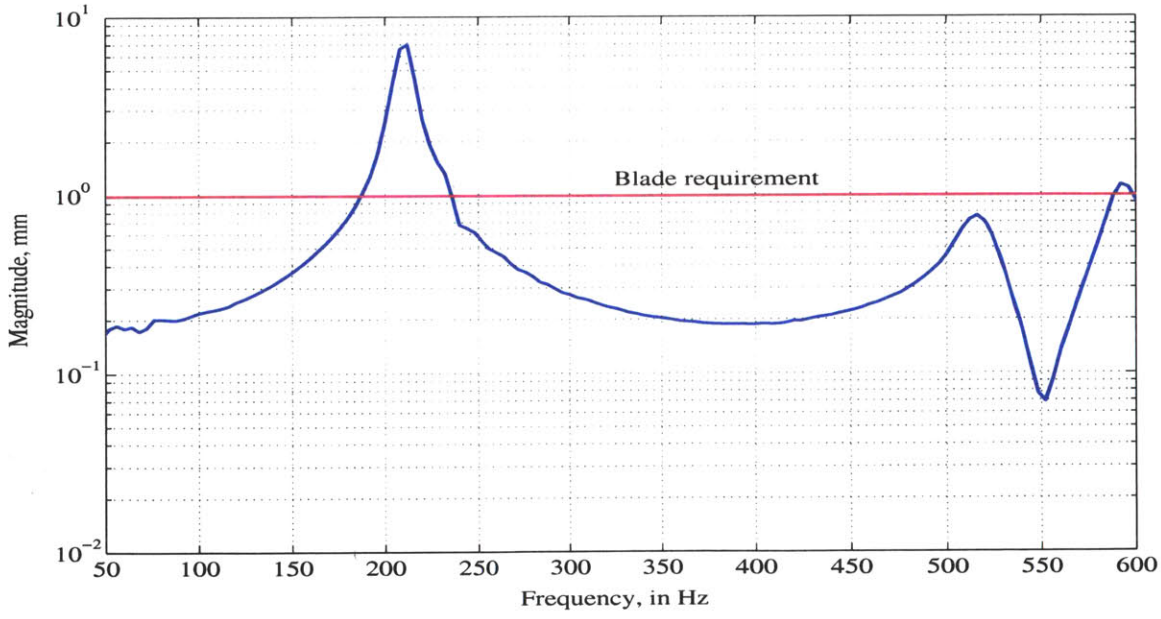

(b) Tip bending frequency response.

Figure 7-6: Frequency response of active wired spar on benchtop due to a signal of 220 V. Laser displacement measurements.

tively) requirements within the bandwidth of the laser sensor.

- It may be noted that because the actuators can take more than 220 V electric signal by the method discussed in Section 4.3.1, the maximum actuation level should be increased by a factor of 1.5.

- However, the actuation level will decrease by about one order of magnitude, when the foam is attached to the spars, as predicted by the blade finite element model. The frequency response of the tip twist for the spar-foam and spar-alone cases predicted by the blade FEM are shown in Figure 7-7. Some of the methods of increasing the actuation level are discussed in Chapter 8.

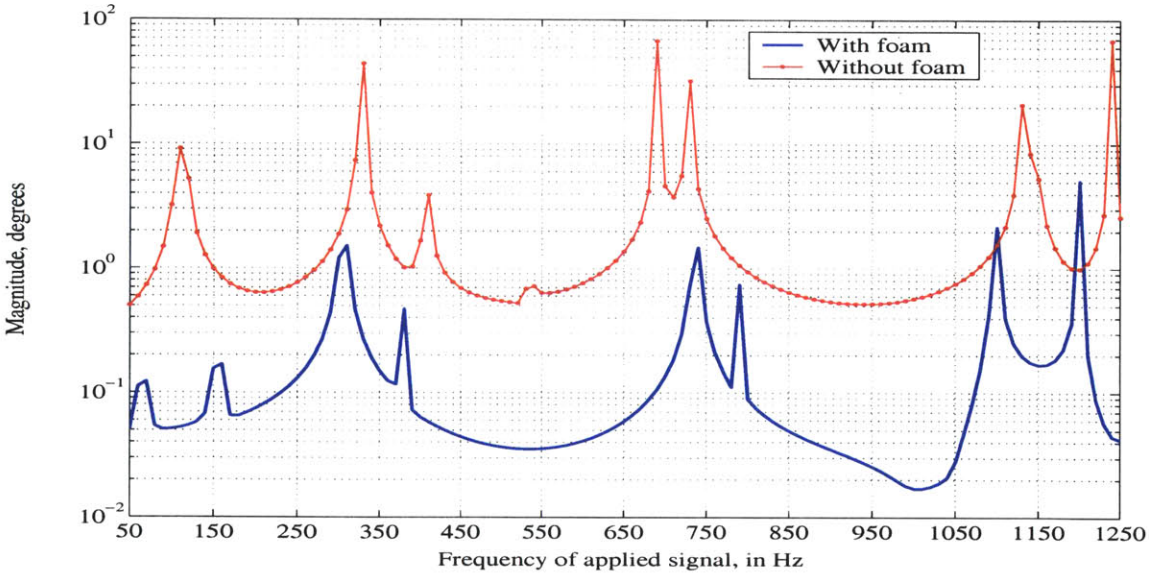

Figure 7-7: Blade FEM prediction of frequency response of blade tip twist with and without foam, at rest condition. Excitation of 220 V at all frequencies.

A comparison between the tip twist frequency response obtained by the benchtop test and that predicted by the FEM for the spars is shown in Figure 7-8. Although the level of actuation achieved is similar in both cases, the resonance frequencies are totally different. One of the reasons is associated with the mismatch of the tested article and the FEM model. The specimen was built based on desired geometries for the spar that could not be achieved by the hand-held cutting process. Another reason explained in Section 2.4.6 is that the FEM did not model the slippage of the actuators over the spars during the bonding

process. The third reason for the difference is because of inaccurate reproduction of the ply drop-off regions from the specimen to the FEM, since they are not visible from outside. As discussed in [7], modeling inaccuracies such as uncertainty in properties of graphite-epoxy plies may be another reason. The uncertainty in properties result from the inability to control epoxy flow inside the molds during cure.

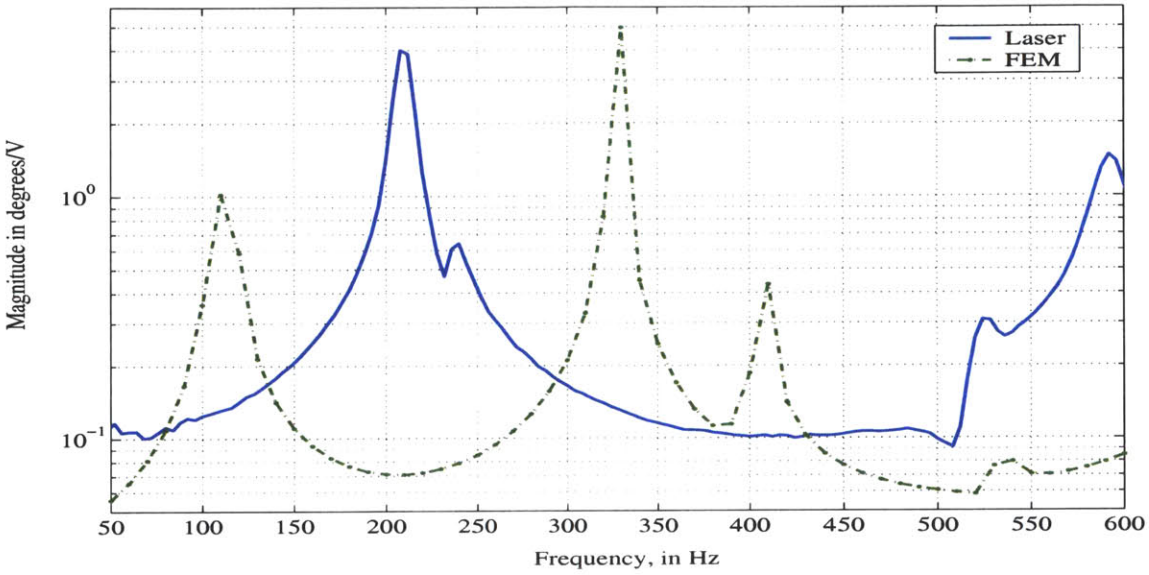

Figure 7-8: Blade FEM prediction of frequency response of spar tip twist versus the benchtop test result.

The transfer functions of the four strain gages to the input signal for in-phase and out-of-phase actuations are shown in Figures 7-9 to 7-12. The transfer functions maintain a constant trend (without increasing or decreasing) over the whole frequency bandwidth of interest (that is, from 50 to 1250 Hz), showing clear strain gage readings over this range. Therefore, by finding the relationship between the strain gage and laser readings between 50 and 600 Hz, the tip twist and bending deflection of the spar can be extrapolated from the magnitudes of strain gage readings at frequencies higher than 600 Hz. It can be safely concluded that the dereverberated tip twist is expected to be around 0.1° and tip bending deflection around 0.2 mm at frequencies higher than 600 Hz. The second point to note about the strain transfer functions is that the phases of strain in the actuators on both sides of a spar are opposite, conforming the bending deflection of the spar. This is true for both in-phase and out-of-phase actuation cases. Finally, it can be seen that the 1250 Hz

bandwidth effectively captures the first three modes of the spar system, and that the first two resonant frequencies correlate well with the laser displacement measurements shown in Figure 7-6.

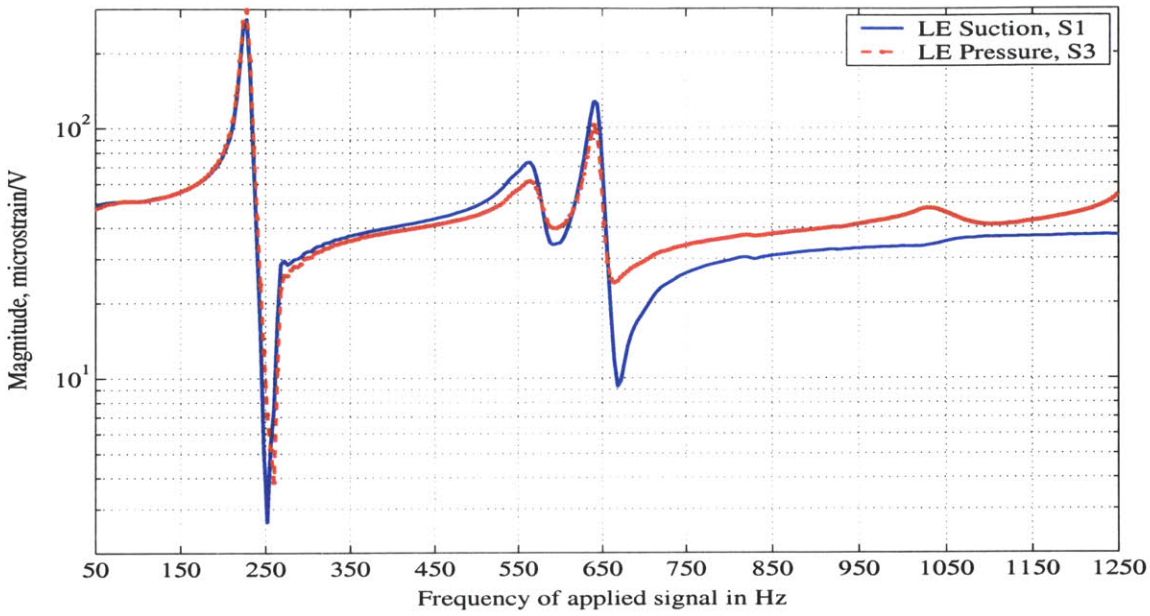

(a) Magnitude.

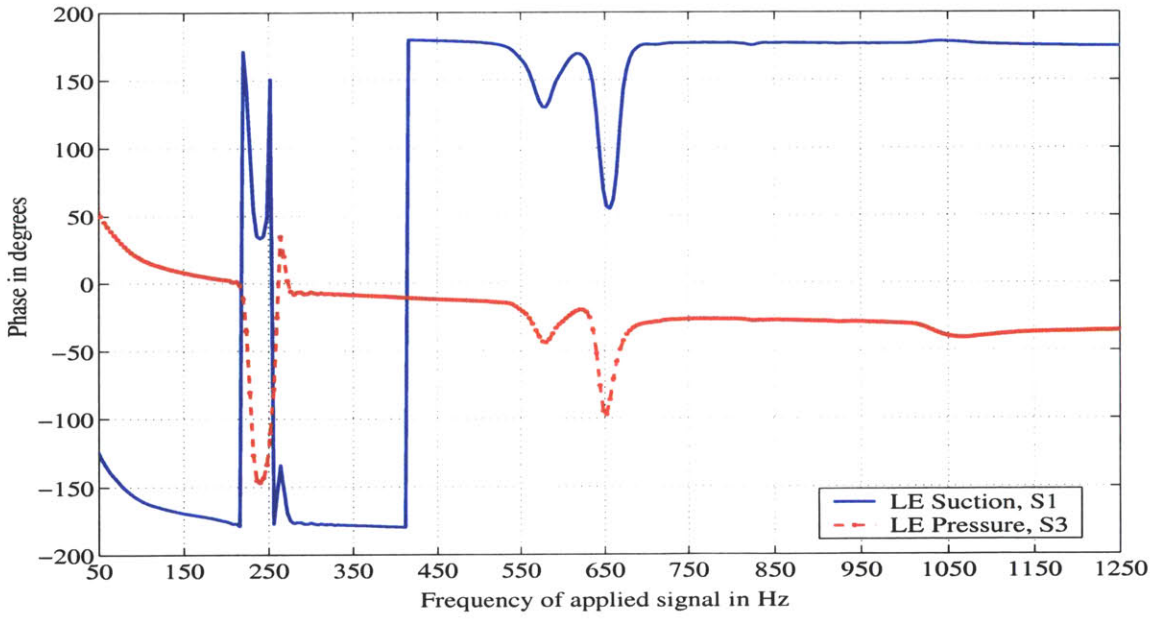

(b) Phase.

Figure 7-9: Transfer Function of the leading edge strain gages to the input signal. Input of 220 V in-phase to both spars. Benchtop Test.

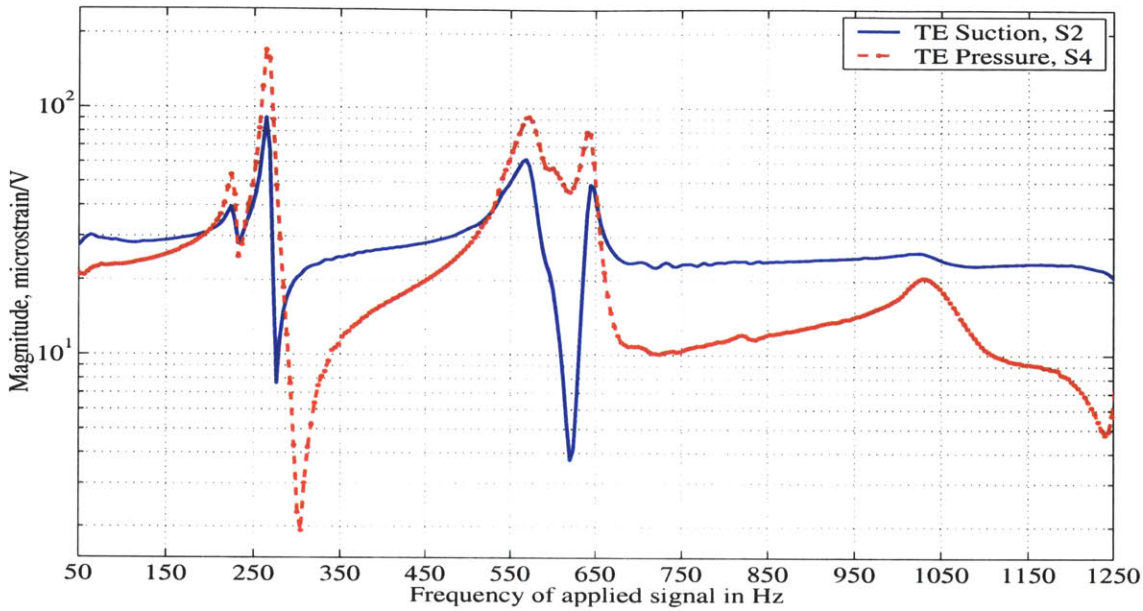

(a) Magnitude.

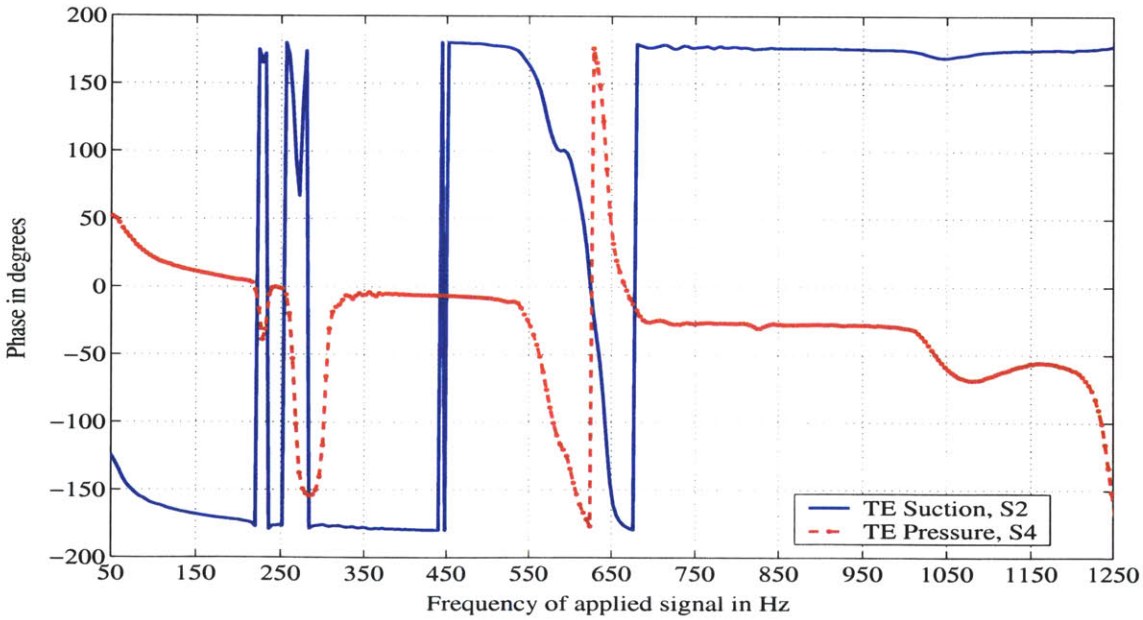

(b) Phase.

Figure 7-10: Transfer Function of the trailing edge strain gages to the input signal. Input of 220 V in-phase to both spars. Benchtop Test.

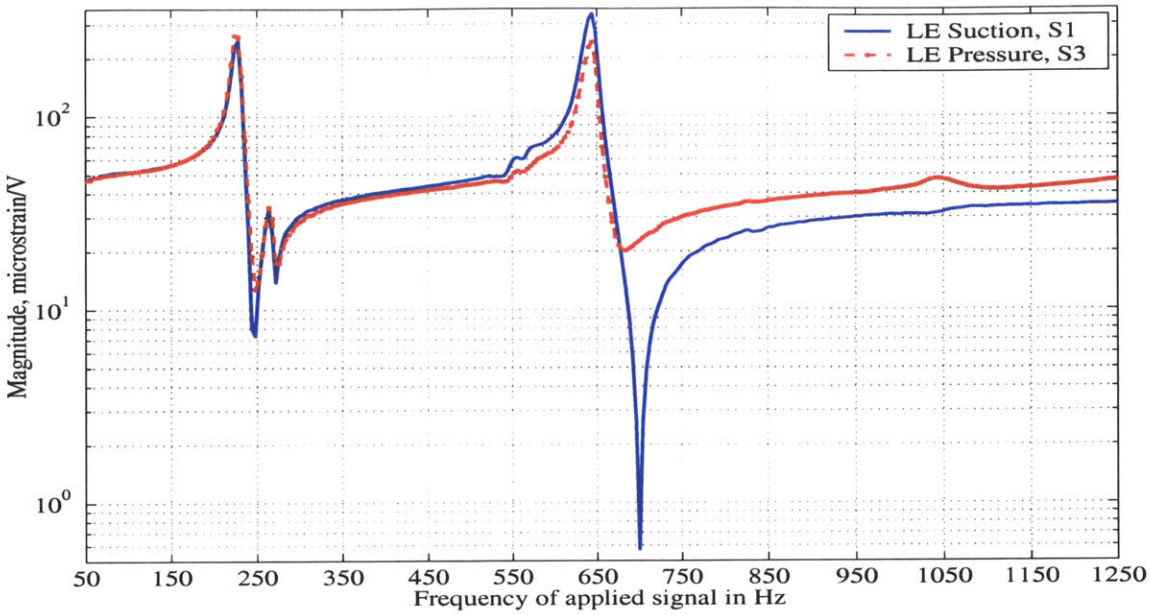

(a) Magnitude.

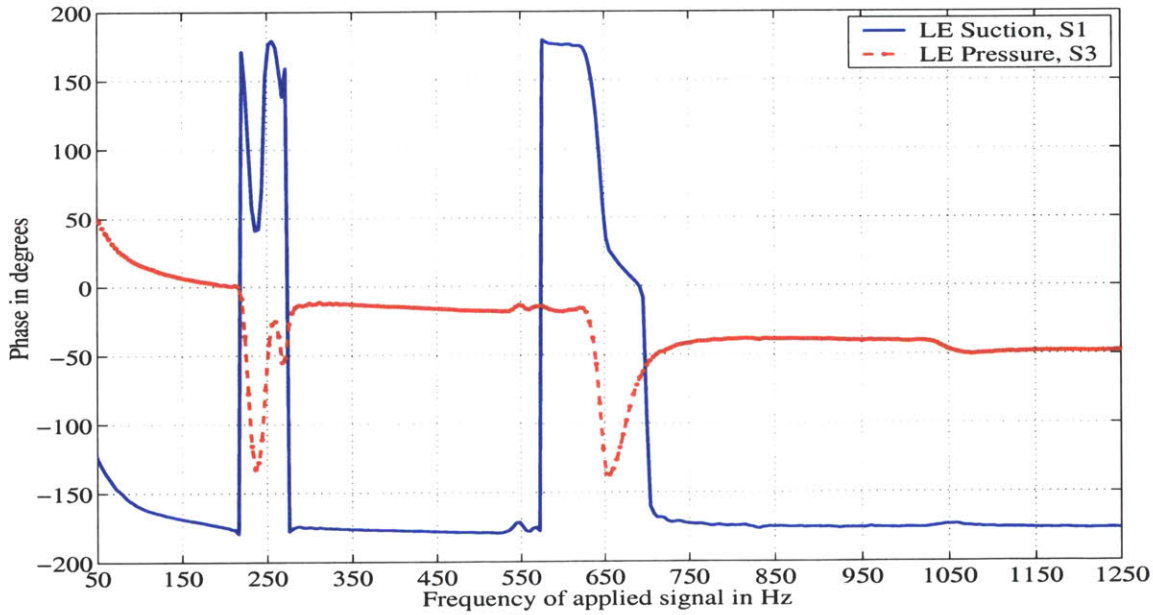

(b) Phase.

Figure 7-11: Transfer Function of the leading edge strain gages to the input signal. Input of 220 V out-of-phase to both spars. Benchtop Test.

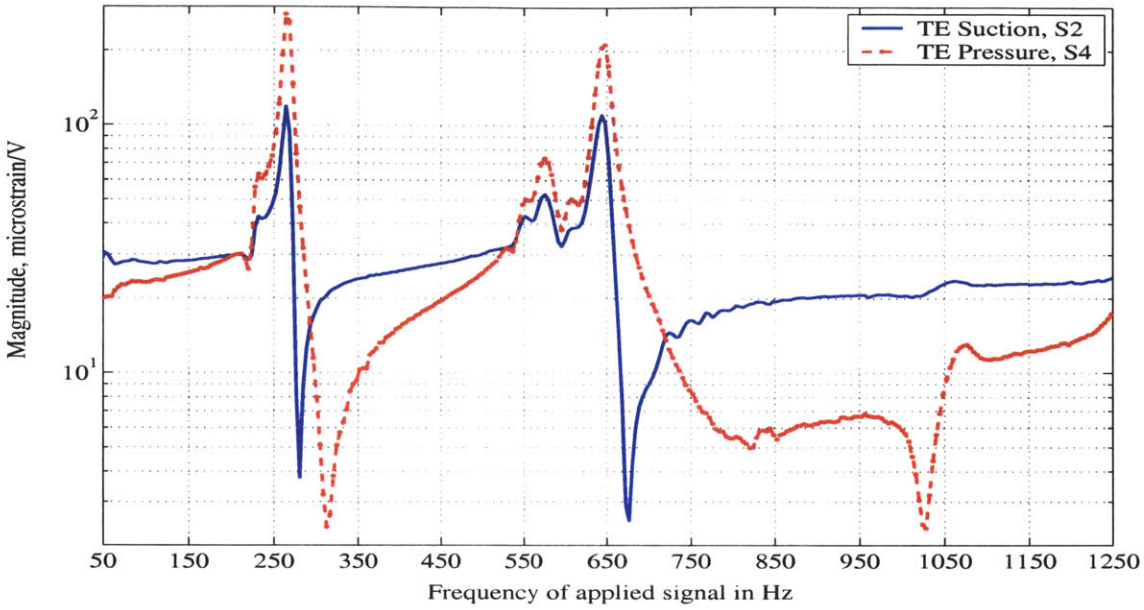

(a) Magnitude.

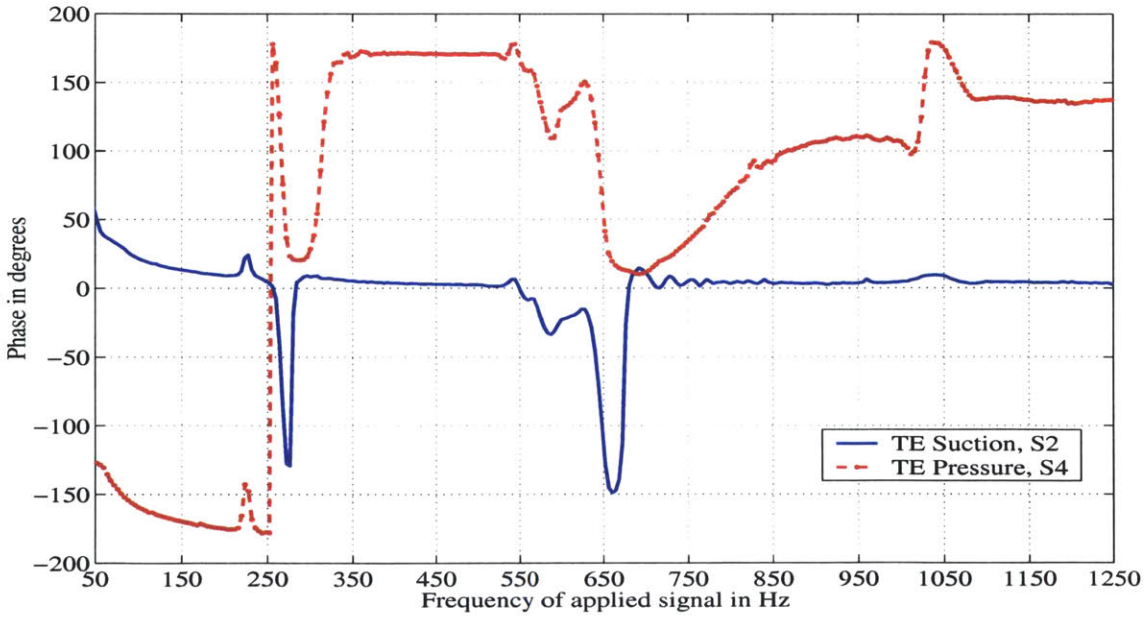

(b) Phase.

Figure 7-12: Transfer Function of the trailing edge strain gages to the input signal. Input of 220 V out-of-phase to both spars. Benchtop Test.

7.2 Spin Pit Tests

7.2.1 Additional Instrumentation

A spin pit was constructed for conducting the actuation tests of the active rotor blade under rotation, in vacuum. The spin pit consists of a drive system (a high-speed motor and a drive shaft), and a vacuum chamber that encloses the rotating components. Communication with the blade (that is, measuring response and sending actuation commands) is achieved through a high power 26-channel slip ring. The slip ring contains the sensor channels used for the blade-mounted sensors and the power channels for the actuators. Due to limited number of channels available to the blade, a decision was made to reduce the number of individual connections to maximize the number of sensors. One of the decisions was to set a common ground for the strain gages; hence the wiring configuration of Section 4.4 was adopted. The test rig also includes a set of auxiliary monitoring systems that constantly measure temperature, vibration, rotational speed, etc. to ensure that tests are performed soundly. A cut-away view of the rig is shown in Figure 7-13.

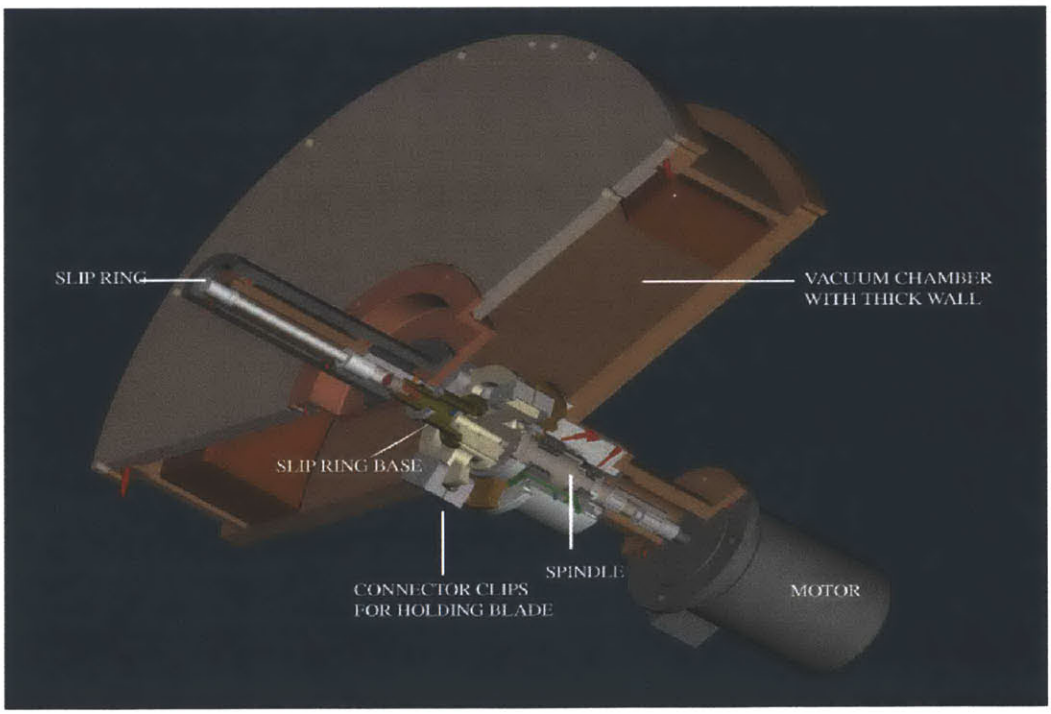

Figure 7-13: Cut-away view of spin pit – the test rig used to perform blade actuation tests under rotation in vacuum.

Since the blade is in a moving frame, a sensor system associated with the moving blade

is needed to capture the blade deformation pattern in the fixed frame. An example of such a system is the eddy current sensor [19], which is based on the principle of formation of eddy current in a conductive specimen resulting in change in electrical field in the sensor. The active rotor blade tip can be metal painted at the tip to make it conductive. The sensor can be mounted inside the vacuum chamber by means of brackets. Because of time constraints, the bracket design could not be completed and so blade tip displacement could not be measured. The strain gage readings were the only output measured.

The active wired spar was fixed by means of clips as shown in Figure 7-14 and counter-balancing weights were put inside the other clips.

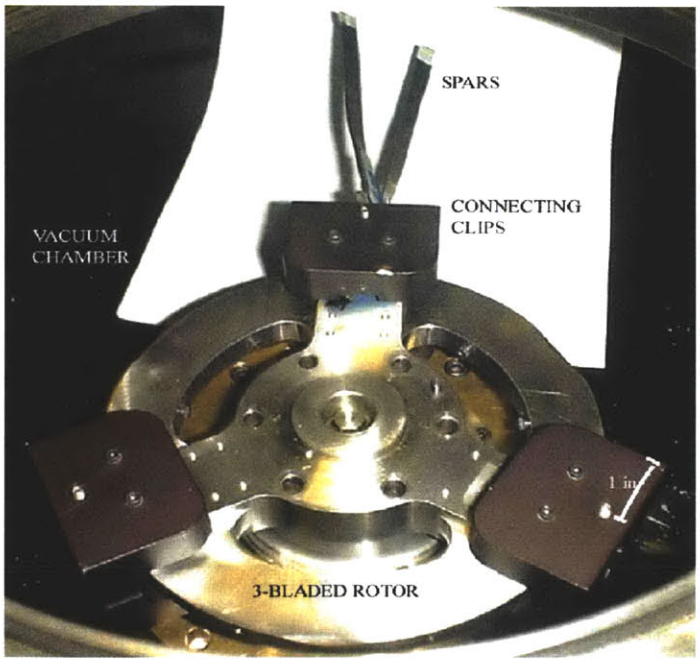

Figure 7-14: Boundary condition for the spin test.

Actuation tests were performed according to the plan shown in Section 7.1.2. The tests were performed for various rotational speeds of the spar system, starting from 0 rpm in steps of 4000 rpm. Initial tests were done by grounding the copper-Kapton sheet in between the actuator and spar. As expected, a 20 dB increasing tendency was observed in the strain transfer function with respect to the signal generator output. Parasitic capacitative effect on the strain gages was one of the factors affecting the output. To eliminate this effect, the power connections to the actuators were flipped. However, there was no change in the

nature of the transfer functions. In fact, at higher rpm and frequencies above 400 Hz, the increasing tendency completely overwhelmed the strain gage output due to blade dynamics. This is illustrated in Figure 7-15.

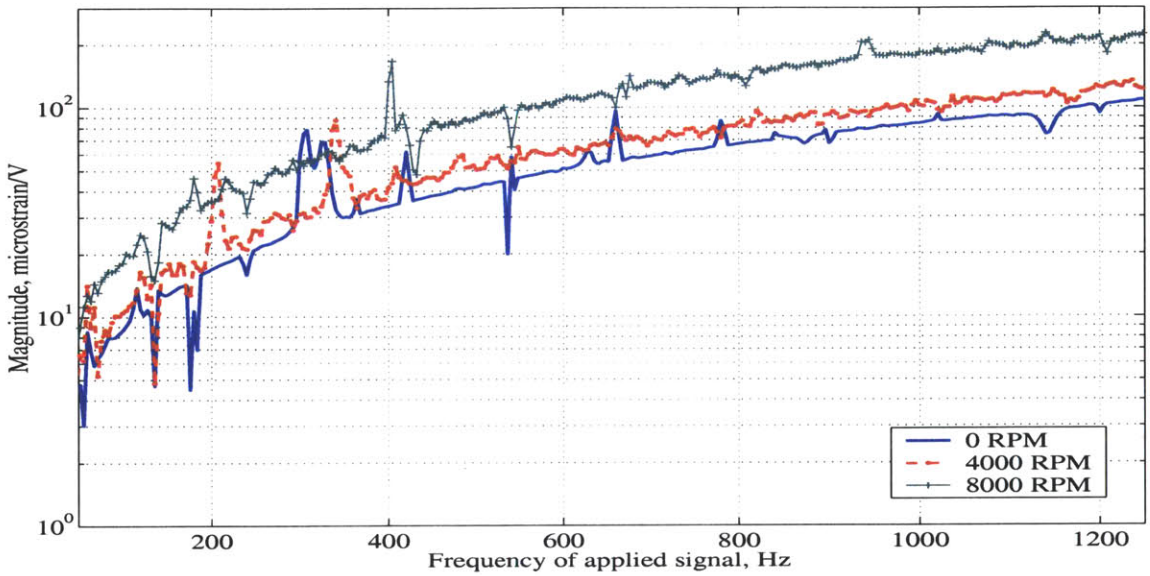

Figure 7-15: Transfer function of LE suction side strain gage to input voltage at various rotational speeds. Excitation of 220 V at all frequencies.

Post-experimental investigation found that there existed ground loops in various portions of the electrical circuitry of the spin rig (such as loop between the grounds of power amplifier and spin pit chassis, and that between the strain amplifer and chassis). This caused the signal to flow between various grounds, causing virtual capacitative effect. This effect imparted the aforementioned noise to the strain gage readings. This can be eliminated by proper wiring, grounding and shielding of the various components of the spin pit and by keeping proper inter-component spacing wherever possible. Another observation was that there was a constant drift of about 100 $\mu\epsilon$ in the strain gage amplifier output. One probable cause for this is the joining of all the strain gage grounds at the base of the blade, which was not there in the benchtop test where all the strain gage wires came out separately. Both these steps involved significant rewiring of the blade and rig. Time constraint did not allow the completion of the tests to take place.

7.2.2 Final Remarks

The spin pit tests indicate the necessity for rewiring the blade and slip ring to minimize the effects of strain gage capacitance and the ground loops in the spin pit circuitry. After completing these steps, the foam can be attached to the spars. The whole blade should undergo both tests (benchtop and spin) before testing it in the presence of air flow in the blowdown compressor at MIT's Gas Turbine Laboratory.

Chapter 8

Concluding Remarks

8.1 Summary

The active rotor project was conceptualized to develop an experimental database on aeroelastic phenomena, particularly high cycle fatigue and flutter, over the entire operating range of the gas turbine engine. The active rotor has blades made of two stress-bearing composite spars, aerodynamically shaped foam, piezoelectric actuators attached to the spar base, and root shaped to insert the blade into the 26-bladed rotor. The shape of the blade can be deformed by bending the two spars either in the same direction or in opposite directions while the bending of the spars can be achieved by actuating the piezoelectric wafers attached to both sides of the spar in opposite phase. The requirement prescribed for this active rotor blade, from aerodynamic consideration, is 0.25° of tip twist and 1 mm of tip bending. The basis of the design is the 31.3% scaled GE Fan C blade.

The thesis analyzed the models developed for the design of the active rotor blade from previous studies. The following parameters were obtained from those models – spar, actuator, and foam dimensions and material. Since the issues relating to root design, spar location within blade and spar-foam bonding were not considered in those models, they were discussed in detail in this thesis.

The root was designed to contain the graphite-epoxy fibers coming out of the spars, and a graphite wedge (filler) to maintain the root shape. The wedge half-angle was chosen as 45° since it corresponds to the minimum root stress at 16000 rpm, as predicted by a finite element model of the root. Also, graphite filler was found to produce lower stresses than metal ones. A transition element was then designed to join the straight root piece to the

twisted spars as smoothly as possible.

To get the best spar location within the blade, a finite element model of the blade was constructed. The gap between the spars was varied and the tip twist actuation of the blade predicted. A 20-mm spar gap gave the optimum results at the first two vibration modes of Fan C blade.

The stresses and strains in the various parts of the blade, rotating at 16000 rpm, were then predicted. The stress in the spar and foam were found to be within failure limit. Although strain in some regions of the piezoelectric actuator was higher than ultimate, it is expected to survive the centrifugal load after being packaged with copper-Kapton, as indicated by previous tensile pull tests. The maximum amount of untwist of the blade shape due to rotation was found to be 17.9°. This indicates that an extra pretwist needs to be given so that the blade will match the Fan C geometry at a certain operating condition. The tip twist and bending actuation limitation of the blade at rest condition were also found. The FEM predicted that these values are lower than the initial target. Despite this, manufacturing and testing of this blade configuration was commenced. The reason is that this configuration, once realized, would provide an invaluable and robust experimental tool to perform control studies on flutter and estimate aerodynamic loads on a scale much larger than presently achievable, although lower than the initial target. Moreover, with further development of piezoelectric material systems, higher authority actuators can replace the current ones in use.

The spar-foam bonding was assumed to be perfect in the FEM model. Since the shape of the interface between the two is complicated and analyses such as shear lag are not useful, experimental method was chosen for finding the right epoxy glue. However, to strengthen the bond, the area of contact between the spar and foam was increased by introducing a graphite-epoxy tab between the spars. The effect of tab on the stresses and strains in the blade parts was found to be insignificant for the present configuration.

Aerodynamic pressure at Mach number 0.70 and flow angle 61° were added to the blade in the FEM. Since the stress and strain levels were within failure limits, it was concluded that the design was safe enough for the blade to be used for testing in the presence of airflow at 16000 rpm speed.

The manufacturing issues related to the spars and filler were investigated next. The filler was manufactured by making a plate of quasi-isotropic layup, and curing and cutting

the plate to get the desired shapes. Aluminum molds were made for spar manufacture; the prepreg was laid up and cured inside the molds along with the filler inserted at the root to give a graphite-epoxy twisted plate. This plate was cut into spars by hand-held tools such as Dremmel. Tests showed that this did not produce an accurate specimen. A tensile pull test was conducted on a straight untwisted single spar specimen prepared under straight aluminum molds using a similar procedure; the test verified the integrity of the root design under loads corresponding to 16000 rpm.

The next stage involved piezoelectric packaging and blade wiring. The old method of packaging and wiring was critically analyzed and improvements made. The lead shape for the twisted blade was obtained on copper-Kapton sheets, and then attached to the actuators. Strain gages were bonded on them and the packaged piezoelectric wafers underwent two characteristic tests – (a) butterfly tests to find the repoling voltage, and (b) hysteresis tests to find the d_{31} characteristic value. The actuators were then bonded to the spars, and the wires were routed around the spars and root to emerge from the base of the blade.

The lead shape adopted for the actuators precluded the application of precompression needed for tailoring the maximum actuation level to the desired centrifugal load, and also application of DC offset to the alternating signal needed for increasing the signal amplitude without repoling the actuators. Despite this, the lead shape was adopted, because conducting the actuation test at rest and under rotation will help in obtaining the required amount of precompression and also give an estimate of the actuation limits of the blade.

The next manufacturing step involved getting the correct foam shape. Thermoforming was used for giving the desired shape. Tests showed that the required amount of twist could not be obtained by thermoforming without breaking the foam. Also, this process stiffened the foam and did not give the desired shape at the leading and trailing edges.

The final step involved assembling the parts together to get the active blade. To resolve all issues regarding the assembly, an attempt was made to manufacture the first active rotor blade. Spars were hand cut from the graphite plate and a foam was thermoformed to get an approximate shape. Grooves were made on the foam using hand-held tools and the spars were glued at the grooves using Epotec 301. Glass-epoxy fibers were attached at the edges of the foam and the system cured under elevated temperature and high pressure inside aluminum molds made for the blade. A spin test showed that the foam got separated from the spars at 6500 rpm.

Since thermocycling was an integral part of blade manufacturing procedure, its effects on blade actuation performance were investigated. This was accomplished by actuation tests done on a straight untwisted spars with foam that was bonded at room temperature, and then underwent several thermocycles. The results showed a drop in actuation level of the piezoelectric material after each thermocycling process.

Tests were conducted on the wired active twisted spar system on benchtop to verify its proper working and to find its tip twist and bending actuation frequency response. Although the spar satisfied the requirements, the blade FEM predicted that the actuation level decreases by an order of magnitude when foam is attached to the blade.

The spars were then put inside the spin pit and rotated from 0 rpm onwards, in steps of 4000 rpm. Actuation tests were conducted at and after each rotational speed. It was observed that the capacitative effect between the strain gage and underlying copper-Kapton sheet as well as ground loops that existed in the electrical circuitry of the spin pit system resulted in a 20 dB increasing slope in all the strain transfer functions with respect to the input signal. This increasing trend completely overwhelmed the blade dynamics at frequencies greater than 400 Hz. So the tests were stopped at 8000 rpm.

8.2 Conclusions

The following conclusions may be drawn from the work done on the active rotor.

Spar and Root

The material, graphite-epoxy, can survive the 16000 rpm rotational environment. The spars emerge radially from the rotor and have a gap of 20 mm at the base, and a width of 9 mm throughout the length. The fiber angle is $\pm 20°$ and there is a linear tapering of the cross section from $[\pm 20°]_{6s}$ at the base to $[\pm 20°]_s$ at the tip.

Various tests show that most of the adopted manufacturing techniques for the spar and the root is adequate for this study. However, cutting of the spars from the graphite plate by hand-held tools did not give the required accuracy; so more precise methods are desired.

Packaging of Piezoelectric Actuator and Blade Wiring

The adopted method of packaging the piezoelectric actuator is adequate for this work. The 3-mil copper-Kapton sheet provides convenient electrode manufacturing features, including direct printing of the lead shape on it by a regular laser printer, and enough flexibility and strength to be routed around the twisted spar-root system as well as survive the blade manufacturing process.

Also the adopted way of routing the wires from the strain gages over the twisted spar-root system has been found to be effective during most of this research work. Connection of all the strain gage and actuator wires to nodes at the base of the blade, and that of all outside wires (from power and strain gage amplifiers) to these nodes is a simple and elegant way of making the blade 'independent' of the wiring system followed in the spin pit. This facilitates the replacement of one given blade to another one.

However, this wiring scheme has several problems. One is that the piezoelectric actuators are not totally independent of each other, and so no DC offset or precompression can be applied. The common terminal of the actuator leads needs to be separated. Another is that the common strain gage ground makes it difficult to get stable strain gage readings from the strain gage amplifiers. By separating the grounds, more stable readings can be obtained.

Foam

Rohacell WF 200 foam is predicted to be strong enough to survive the centrifugal loads at 16000 rpm as well as flexible enough to enable deformation of blade shape due to piezoelectric action. Imparting the desired twisted aerodynamic shape to the foam by thermoforming is a difficult task. Machining the right shape from a rectangular block of foam, supported by the molds, seems to be a better alternative. Finishing of the leading and trailing edges can be done by hand-sanding. However, no conclusion can be made from the present study, regarding the alternative of adding extra material such as glass-epoxy for getting more accurate leading and trailing edge shapes. This has been left for future work.

Blade Assembly

The attempts made with the first active rotor blade construction and the results of its subsequent spin tests suggest that the mismatch between the spar and foam shape should

be minimized to strengthen the bond. This may be taken care of by cutting the spars by water-jet and CNC machining of the foam.

Secondly, Epotec 301 seems to have worked so far in maintaining the spar-foam bond. Spin tests at 16000 rpm will determine its effectiveness.

Thirdly, the groove size on the foam should be about 5% smaller than the spar width so that the spar fits tightly after being subjected to pressure. Also, the groove depth must be same as that of the spar-actuator system throughout its length. This tight tolerance would not be possible by machining using hand-held tools, as shown before. Again, CNC machining of the foam to form grooves seems to be a better alternative.

Finally, subjecting the foam to thermal cycles at any stage during the blade construction has proved to be detrimental to the blade actuation performance. Hence a room temperature cure cycle should be followed for the bonding between the spars and foam to take place.

Strain Gage Sensors

Preliminary tests on benchtop showed that to get meaningful strain gage data, the copper-Kapton leads between the strain gage and the piezoelectric wafer need to be grounded while the other lead should be used for signal application. In addition, initial tests inside the spin pit have indicated that ground loops existing in the spin pit circuitry should be removed.

Blade Actuation Performance

The blade tip twist was predicted by the FEM to be of the order of 0.05°, lower than the initial target of 0.25°, at all frequencies of interest, except at the poles. The bending deflection predicted by the FEM is of the order of 0.04 mm, lower than the target of 1 mm, at all frequencies, except at the poles. At the poles, the twist actuation level reaches as high as 5° and the bending actuation reaches as high as 6 mm.

The benchtop extrapolated actuation results are as follows. The twist actuation level is of the order of 0.1° at all frequencies except at the poles where it reaches a high of 4°. The bending actuation level is of the order of 0.2 mm; at the poles, it reaches a high of 6 mm. So this specimen meets the twist requirement but not the bending deflection one at all frequencies except at the poles. It may be noted here that the actuation level is expected to drop by as much as one order of magnitude, as predicted by the finite element model.

Also, the strain gage actuation level is of the order 20 $\mu\epsilon$ over all frequencies of interest,

except at the poles where it goes up to 200 $\mu\epsilon$. This may be accounted for, while calculating the required amount of precompression to be given to the actuators.

Since the region of high actuation at the poles covers a narrow band of frequencies, it may be concluded that the actuation level reached by the present design of the active blade will be lower than the target. However, with potential improvement of this design as presented in the next section, a robust tool could be built which would help in gathering turbomachinery aeroelastic data over a larger operating range than is currently possible.

8.3 Recommendations

The following recommendations may be made, based on the study conducted on the active rotor blade.

Blade Design

The blade finite element model has ignored the localized regions of stress and strain levels higher than the respective failure limit. This needs to be addressed in the future in the context of damage initiation and propagation. In addition, the blade finite element model needs to be updated to reflect the real manufacturing limitations discussed in Section 2.4.6 and to obtain the frequency response of the blade under rotation.

Blade Manufacture

The following areas of blade manufacturing procedure need to be resolved:

- More work is needed to demonstrate the applicability of water-jet cutting to achieve the desired tolerance in the spars.

- CNC machine feasibility for foam shaping and manufacturing grooves, smaller than the spar width, needs to be demonstrated.

- Significant work needs to be done regarding the constitution of the leading and trailing edges. The blade finite element model developed in this thesis can be a convenient starting point for this investigation. Since introduction of extra material at the edges increases the stress level on the blade and decreases its performance, this material

should be introduced only if CNC machining together with hand-sanding cannot produce the edges up to the required accuracy.

Blade Testing

To get conclusive data from the active blade tests, the following improvements need to be made:

- Significant rewiring of the blade needs to be done to separate the strain gage grounds to stabilize the strain gage amplifier outputs. Also, the two legs of the copper-Kapton leads sandwiched between the actuator and the spar need to be separated from each other. This will enable precompression while bonding the actuators to the spars as well as application of DC offset to the sinusoidal signal applied during actuation tests.

  Figure 8.3 shows a plan of the node structure at the blade base when the new scheme is implemented. It may be noted that after applying precompression, the number of actuator nodes may be reduced. This may be accomplished by adding jumpers at the common points.

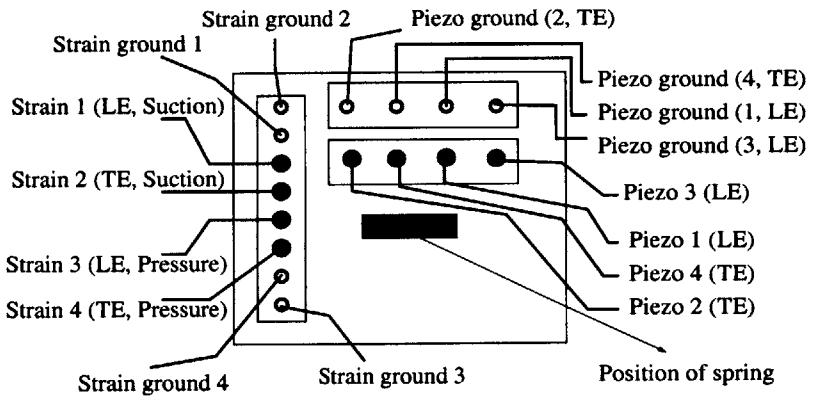

Figure 8-1: New wiring plan – Separating the common ground junction of the strain gages and the actuators.

- To increase the blade actuation level, a 360 V amplitude alternating signal with 120 V DC offset may be applied to the actuators. Also, the signal should be applied to the copper-Kapton electrode sandwiched between the actuator and the spar, while the other electrode is grounded. This will eliminate the debilitating effect of the strain gage parasitic capacitance within the operating range.

Blade Performance

Since the present blade design does not meet the prescribed performance requirements, several changes can be made to the design, as enumerated below.

- Firstly, multi-wafer actuators may be used instead of single wafer ones. The number of wafers will be limited by the strength considerations of the blade. The packaging of multi-wafer actuators needs to be carefully done so as to eliminate inter-wafer air gaps which might result in sparking when signal is applied.

- Active fiber composites having double the actuation capabilities of piezoelectric wafers may be used as actuators. The graphite-epoxy plate may replace the spars and active fiber angles of $\pm 45^\circ$ will enable tip twist and bending. This also needs a suitable shell that is (a) thin enough to cover the composite plate and maintain the desired thickness distribution over the blade surface, (b) flexible enough to be shaped into the desired aerodynamic shape, (c) light and strong enough to survive the centrifugal load at 16000 rpm, and (d) flexible enough to allow desired deformation of the blade. Rohacell WF 200 cannot meet the first and second requirements simultaneously because of its large cellular structure; a combination of packing foam such as styrofoam and thin rubber sheets may be useful. This issue needs further investigation. A typical cross-section is shown in Figure 8-2.

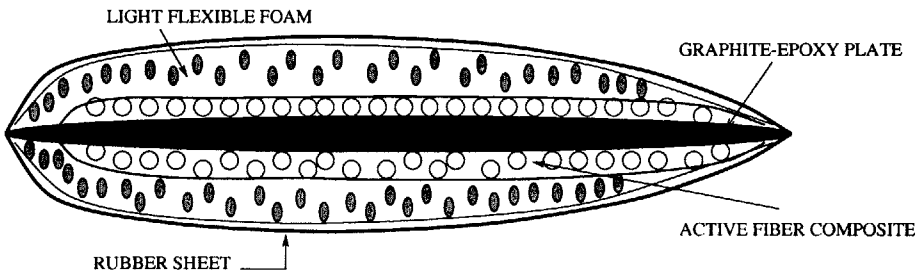

Figure 8-2: New design – typical cross-section of active rotor blade with active fiber composite.

Rotor Design

Two changes need to be made in the rotor. First is the design and manufacture of a hub with 26 slots instead of the present 3 slots. This includes designing new clips to accommodate the

26 blades within the rotor circumference and thus designing new root of the blade. Second is the design change that needs to be made to incorporate the rotor into the blowdown compressor of the MIT Gas Turbine Laboratory. Ultimately, the wind tunnel site will serve to conduct extensive aeroservoelastic experiments on the active rotor blades.

Appendix A

Theoretical Background of PATRAN Blade Finite Element Model

This appendix outlines the theoretical issues involved in the PATRAN blade finite element model in general and piezoelectric actuation in particular. The reader may refer to [8] for more information on finite element modeling, and [16] for PATRAN implementation issues. Further details on piezoelectric action can be found in [7] and [13].

It may be noted that aerodynamic loads on the blade have not been referred to in this outline – inclusion of aerodynamic loads in external load vector form (like centrifugal loads) is trivial. The effect of aerodynamic loads on the blade have been discussed in section 2.4.4. The appendix ends with a discussion of the various analysis packages available in PATRAN that are used in the FEM and implementation of piezoelectric actuation.

- The blade is divided into finite elements consisting of nodes. The blade displacement $\{u\}$ at any point within the blade due to loading is obtained from the displacement at the nodes $\{d_e\}$ through interpolation function, known as shape function [N], as shown below.

$$\{u\} = [N]\{d_e\} \tag{A.1}$$

- The strain vector at any point in the blade can be expressed in terms of nodal dis-

placement vector $\{d_e\}$ as follows.

$$\{\epsilon\} = [B]\{d_e\} \tag{A.2}$$

where [B] is related to [N] by a differential matrix operator.

- The stress-strain characteristic equation can be written as

$$\{\sigma\} = [D](\{\epsilon\} - \{\Lambda\}) \tag{A.3}$$

[D] is obtained from the material properties. The stress-strain relationship of the piezoelectric actuator is similar to that of a thermoelastic material, the thermal strain term being replaced by the piezoelectric actuation strain term Λ, as shown below. Note that actuation is done by applying electric field in the through-the-thickness direction (3 in common notation) and using the strain in the plane of the piezoelectric material via the electromechanical coupling coefficient (d_{31}).

Thus, in the 1-3 plane, one has,

$$\Lambda = d_{31}\frac{V}{t_{piezo}} \tag{A.4}$$

where V is the applied voltage and t_{piezo} is the thickness of the piezoelectric layer.

- Kinetic energy is given by

$$\begin{aligned} T_e &= \frac{1}{2}\int_{v_e} \rho \frac{\partial\{u\}^T}{\partial t}\frac{\partial\{u\}}{\partial t}\,dv \\ &= \frac{1}{2}\{d_e\}^T\left(\int_{v_e} \rho[N]^T[N]\,dv\right)\{d_e\} \\ &= \frac{1}{2}\{d_e\}^T[M_e]\{d_e\} \end{aligned} \tag{A.5}$$

where ρ is the material volumetric density.

- Potential energy of the blade is given by

$$\begin{aligned} U_e &= \frac{1}{2}\int_{v_e}\{\sigma\}^T\{\epsilon\}\,dv \\ &= \frac{1}{2}\{d_e\}^T\left(\int_{v_e}[B]^T[D][B]\,dv\right)\{d_e\} - \frac{1}{2}\left(\int_{v_e}\{\Lambda\}^T[D][B]\,dv\right)\{d_e\} \\ &= \frac{1}{2}\{d_e\}^T[K_e]\{d_e\} - \frac{1}{2}\{P_{ae}\}^T\{d_e\} \end{aligned} \tag{A.6}$$

- Potential energy due to the centrifugal load is given by

$$\begin{aligned} U_{ce} &= -\int_{v_e}\{u\}^T\{p_{ce}\}\,dv \\ &= -\{d_e\}^T\left(\int_{v_e}[N]^T\{p_{ce}\}\,dv\right) \\ &= -\{d_e\}^T\{P_{ce}\} \end{aligned} \tag{A.7}$$

where $\{p_{ce}\}$ is the centrifugal load vector, proportional to the square of the rotational speed and to density.

- Lagrange's equation of motion is given by

$$\frac{d}{dt}\left(\frac{\partial T_e}{\partial\{d_e\}}\right) - \frac{\partial T_e}{\partial\{d_e\}} + \frac{\partial(U_e + U_{ce})}{\partial\{d_e\}} = 0 \tag{A.8}$$

which simplifies to

$$[M_e]\{\ddot{d}_e\} + [K_e]\{d_e\} = \{P_{ae}\} + \{P_{ce}\} \tag{A.9}$$

By assembling terms for the whole blade, we get the global governing equation of motion.

$$[M]\{\ddot{d}\} + [K]\{d\} = \{P_a\} + \{P_c\} \tag{A.10}$$

Appendix B

Material Properties of Blade

Table B.1: Isotropic properties of piezoelectric anffoam materials.

Entity	Material	E (GPa)	G (GPa)	ν	ρ ($\frac{kg}{m^3}$)
Piezoelectric actuator	PZT-5A	61	23	0.31	7700
Foam	Rohacell WF-200	0.35	0.15	0.17	205

Table B.2: Properties of graphite-epoxy used in the blade and root FEM. The 32-ply properties are used for the root and transition element.

Entity	3-D Anisotropic properties of 32-ply layup
Material	Graphite-epoxy
D_{11} (GPa)	116
D_{12} (GPa)	17.2
D_{13} (GPa)	4.54
D_{22} (GPa)	14.1
D_{23} (GPa)	3.91
D_{24} (GPa)	6.33
D_{33} (GPa)	11.2
D_{44} (GPa)	18.7
D_{55} (GPa)	3.77
D_{66} (GPa)	6
ρ ($\frac{kg}{m^3}$)	1545
X_t (MPa)	2356
Y_t (MPa)	50
S (MPa)	105

Entity	2-D Orthotropic ply properties
Material	AS4/3501-6
Resin content	36%
E_{11} (GPa)	143
E_{22} (GPa)	9.81
ν_{12}	0.3
G_{12} (GPa)	6
G_{23} (GPa)	6
G_{13} (GPa)	3.773
ρ ($\frac{kg}{m^3}$)	1545

Table B.3: Steel properties used for the root filler in the FEM.

E (GPa)	G (GPa)	ν	ρ ($\frac{kg}{m^3}$)
210	81	0.3	7800

Table B.4: Properties of Epotec 301 A/B – the bonding agent between the actuator and spar as well as between the spar and foam.

Tensile modulus (room temperature(RT))	1.2 GPa
Shear modulus, RT	2.87 GPa
Density	1090 kg/m^3
Flash point Turns to ash at	200°F (93°C) 662°F (350°C)
Lap shear strength (aluminum-aluminum), at RT	11.7 MPa
Viscosity at 100 rpm, RT	100-200 cPs
Glue capacitance, RT and 1KHz	3.26 nF

Appendix C

Codes for Root Design

In the root design process, a very detailed finite element model was used, as given in Section 2.3.1. For building the solid elements of the root fibers and filler, a code was written in PATRAN COMMAND LANGUAGE (PCL). This language is followed in PATRAN and more information can be found in [16]. Another code in PCL was written to convert the root stresses to Tsai-Hill failure stress concentration factors. The codes are given below.

Program 1

```
$  This program creates solid elements thru surface
$   extrusion for the fibers of the  root

INTEGER plynum
REAL offreal
STRING plynum_str1[VIRTUAL]
STRING plynum_str2[VIRTUAL]
STRING offreal_str[VIRTUAL]
STRING offset_str1[VIRTUAL]
STRING offset_str2[VIRTUAL]
STRING offstring1[17]="[0 0 12345678901]"
STRING offstring2[20]="[.006 0 12345678901]"

FOR (plynum=1 TO 24)
offreal=.0001208*(plynum-1)
```

```
plynum_str1=str_from_integer(plynum)
plynum_str2=str_from_integer(plynum+24)
offreal_str=str_from_real(offreal)
str_assign(offstring1,6,11,offreal_str)
str_assign(offstring2,9,11,offreal_str)

STRING asm_create_patch_xy_created_ids[VIRTUAL]
asm_const_patch_xyz( plynum_str1,
  "<0 .0414 .0001208>", offstring1, "Coord 0",
  asm_create_patch_xy_created_ids )
asm_const_patch_xyz( plynum_str2,
  "<0 .0414 .0001208>", offstring2, "Coord 0",
   asm_create_patch_xy_created_ids )

END FOR
```

Program2

```
$  This program creates a solid for inclined faces

INTEGER plynum
REAL offreal1
REAL offreal2
STRING plynum_str1[VIRTUAL]
STRING plynum_str2[VIRTUAL]
STRING offreal_str1[VIRTUAL]
STRING offreal_str2[VIRTUAL]
STRING offset_str1[VIRTUAL]
STRING offset_str2[VIRTUAL]
$STRING offstring1[21]="[-.0130 0 1234567890]"
$STRING offstring2[21]="[-.0130 0 1234567890]"
STRING offstring1[21]="[-.0159 0 1234567890]"
STRING offstring2[21]="[-.0159 0 1234567890]"
```

```
FOR (plynum=49 TO 60)
$offreal1=-.013+.0001208*(plynum-49)
$offreal2=.0159+.0001208*(plynum-49)
offreal1=-.00919+.0001208*(plynum-49)
offreal2=.01209+.0001208*(plynum-49)
plynum_str1=str_from_integer(plynum)
plynum_str2=str_from_integer(plynum+12)
offreal_str1=str_from_real(offreal1)
offreal_str2=str_from_real(offreal2)
str_assign(offstring1,11,10,offreal_str1)
str_assign(offstring2,11,10,offreal_str2)

STRING asm_create_patch_xy_created_ids[VIRTUAL]
asm_const_patch_xyz( plynum_str1,
 "<0 .0414 .0001208>", offstring1,
 "Coord 0", asm_create_patch_xy_created_ids )
asm_const_patch_xyz( plynum_str2,
 "<0 .0414 .0001208>", offstring2,
 "Coord 0", asm_create_patch_xy_created_ids )

END FOR
```

Program 3

```
$Convert Stresses to Tsai-Hill factor
FUNCTION material_p20( xx, yy, xy )
     REAL xx, yy, xy
     REAL xxm, yym, xym
     REAL deg
     REAL m, n
     REAL X1t, X2t, S
     REAL tsaihill
```

```
        deg = 20
        m = cosd(deg)
        n = sind(deg)

        xxm = m*m*xx+n*n*yy+2*m*n*xy
        yym = n*n*xx+m*m*yy-2*m*n*xy
        xym = -m*n*xx+m*n*yy+(m*m-n*n)*xy

        X1t = 2356e6
        X2t = 50e6
        S   = 105e6

        tsaihill = (xxm*xxm)/(X1t*X1t)+(yym*yym)
                    /(X2t*X2t)-(xxm*yym)/(X1t*X1t)
                    +(xym*xym)/(S*S)
        RETURN tsaihill
    END FUNCTION
```

Another code was developed in MATLAB for estimating the tensile load at the root-blade interface due to rotation of blade at 16000 rpm. The notation followed and the code itself is given below.

```
%Composite spar
rhoc = 1587; l = 0.178; b = 0.009;w = 0.0414;
om = 2*pi*16000/60; t = 0.003;
ro = 0.089;h = 0.0130; p = 0.015+0.030;
rl = ro + h+p;ru = ro + h+ l;
Fc = 2*rhoc*b*t*om^2*((ru^2 - rl^2)/2 - (ru^3-rl^3)/3);

%Foam
rhof = 380; lf = l; bf = 0.065;tf = 0.008;
```

```
Af = bf*tf;
rl = ro+h+p;ru = ro + h+l;
Ff = rhof*Af*om^2*0.5*(rl^2 - ro^2);

%Piezo
rhop = 7700; lp = 36.3e-3-30e-3;tp = 0.254e-3;
Ap = b*tp;
rl = ro + h+p;ru = ro + h+ p + lp;
Fp = 4*rhof*Af*om^2*0.5*(ru^2 - rl^2);

F = Fc + Ff + Fp
A = 2*b*t+Af+2*Ap
(F/A)
(F/A)*(b*t)
```

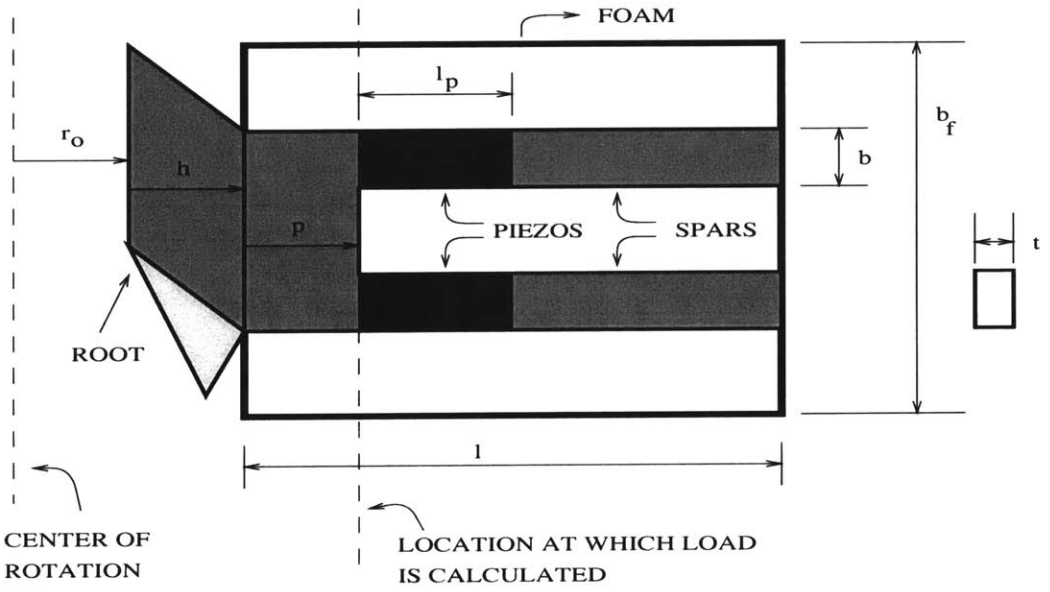

Figure C-1: Notation used in MATLAB

Bibliography

[1] A. V. Srinivasan. Flutter and Resonant Vibration Characteristics of Engine Blades - The 1997 IGTI Scholar Paper. *Journal of Engineering for Gas Turbines and Power*, 119:742–775, 1997.

[2] E. J. Trimble. Report on the Accident to Boeing 737-400 G-OBME near Kegworth, Leicestershire on 8 January 1989. Air Accidents Investigation Branch, Department of Transport, HMSO London, Air Accident Report 4/90 (ISBN 0 11 550986 0), 1990.

[3] U. S. Air Force Scientific Advisory Board. Structural Failure Modes of Titanium Components in Fans and Compressors of Air Force Gas Turbine Engines. Report of the Ad Hoc Committee on Air Force Aircraft Jet Engine Manufacturing and Production Processes, 1992.

[4] E. Livne. Controlled–Motion Models for Wind Tunnel Unsteady Aerodynamic Loads Identification on Deforming Configurations: A Multidisciplinary Challenge. 41th AIAA/ASME/ASCE/AHS/ASC Structures, Structural Dynamics, and Materials Conference, Atlanta, Georgia, April, 2000, AIAA–2000–1485.

[5] R. G. Griffin, D. E. Parker, and L. W. Dunbar. Experimental Quiet Engine Program - Aerodynamic Performance of Fan C. NASA CR-120981, 1972.

[6] R. R. Jutras, R. B. Fost, R. M. Chi, and B. F. Beacher. Subsonic/Transonic Stall Flutter Investigation of a Rotating Rig. NASA CR-174625, February 1981.

[7] G. L. Maahs. *Design of an Active Compressor Blade for Aeroelastic Studies.* Master's Thesis, Massachusetts Institute of Technology, 1999.

[8] K. J. Bathe. *Finte Element Procedures.* Prentice Hall Publication, 1996.

[9] N. A. Cumpsty. Aerodynamics of Aircraft Engines - Strides and Stumbles. Technical Report GTL 213, Massachusetts Institute of Technology, September 1992.

[10] S. Fleeter. *Aeroelasticity in Turbomachines.* Panel Session, ONR, 1972.

[11] R. M. Jones. *Mechanics of Composite Materials.* Taylor and Francis Publication, 1999.

[12] *LabVIEW Quick Start Guide (Version 4.1).* National Instruments Corporation Publication (www.natint.com), 321527A–01, 1997.

[13] K. B. Lazarus and E. F. Crawley. Induced Strain Actuation of Composite Plates. Technical Report GTL 197, Massachusetts Institute of Technology, March 1989.

[14] J. P. Longley. A Review of Nonsteady Flow Models for Compressor Stability. *ASME Journal of Turbomachinary,* 116:202–215, 1994.

[15] *MATLAB - The Language for Technical Computing (version 5).* Math Works Publication (www.mathworks.com), 1996.

[16] M. Reymond, and M. Miller. *MSC/NASTRAN - Quick Reference Guide (Version 69).* Macneal-Schwendler Publication (www.msc.com), 1996.

[17] *Introduction to PRO-ENGINEER (Release 20).* Parametric technology Corporation Publication (www.ptc.com), 1998.

[18] P. A. Lagace, M. Beaumont, J. C. Breuer, and C. F. Varnerin. TELAC Manufacturing Class Course Notes. Technical Report 88-4b, Massachusetts Institute of Technology, September 1992.

[19] G. W. Terpay, and G. G. Zipfel, Jr. Measuring Blade Condition in a Gas Turbine Engine using Eddy-Currents. 9th International Conference on Adaptive Structures and Technologies, Boston, Massachusetts, October, 1998, Proceedings (A99-23285 05-31), Technomic Publishing Co., Inc., 71–80, 1999.

[20] K. E. Willcox, J. D. Paduano, J. D. Peraire, and K. C. Hall. Low Order Aerodynamic Models for Aeroelastic Control of Turbomachines. 40th AIAA/ASME/ASCE/AHS/ASC Structures, Structural Dynamics, and Materials Conference, St. Louis, Missouri, April, 1999, AIAA, 2204–2214, 1999.